SECONDARY AND BACKSCATTER ELECTRON EMISSION FROM CONDUCTORS

Warren G. Wilson

July 1998

Final Report

> APPROVED FOR PUBLIC RELEASE; DISTRIBUTION IS UNLIMITED.

AIR FORCE RESEARCH LABORATORY
Space Vehicles Directorate
3550 Aberdeen Ave SE
AIR FORCE MATERIEL COMMAND
KIRTLAND AIR FORCE BASE, NM 87117-5776

19990203 079

DTIC QUALITY INSPECTED 2

PL-TR-97-1161

Warren G. Wilson
Project Manager

JOHN H. COMTOIS, MAJOR, USAF
Chief, Space Electronics and Protection
Technologies Branch

FOR THE COMMANDER

CHRISTINE M. ANDERSON, SES
Director, Space Vehicles

REPORT DOCUMENTATION PAGE

Form Approved
OMB No. 074-0188

1. AGENCY USE ONLY (Leave blank)	2. REPORT DATE July 1998	3. REPORT TYPE AND DATES COVERED Final; Jan 90 – Aug 92	

4. TITLE AND SUBTITLE
Secondary and Backscatter Electron Emission From Conductors

5. FUNDING NUMBERS
PR: ILIR
TA: 91
WU: 12

6. AUTHOR(S)
Warren Grant Wilson

7. PERFORMING ORGANIZATION NAME(S) AND ADDRESS(ES)

Air Force Research Laboratory/VSSE
Bldg 472
3550 Aberdeen Ave. SE
Kirtland AFB, NM 87117-5776

8. PERFORMING ORGANIZATION REPORT NUMBER
PL-TR-97-1161

9. SPONSORING / MONITORING AGENCY NAME(S) AND ADDRESS(ES)

10. SPONSORING / MONITORING AGENCY REPORT NUMBER

11. SUPPLEMENTARY NOTES

13. ABSTRACT (Maximum 200 Words)
Reports the absolute secondary and backscatter electron yield cross section {#/#} for copper, aluminum, and carbon targets as a function of incident electron energy and angle. Reports the energy distribution of the secondary and backscatter electron as a function of emission angle {#/(#.ev.sr) for the same target set.

14. SUBJECT TERMS
Secondary Electron Yield, Backscatter Electron Yield, Energy and Angle Distribution, Production Cross Section

15. NUMBER OF PAGES
162

16. PRICE CODE

17. SECURITY CLASSIFICATION OF REPORT UNCLASSIFIED	18. SECURITY CLASSIFICATION OF THIS PAGE UNCLASSIFIED	19. SECURITY CLASSIFICATION OF ABSTRACT UNCLASSIFIED	20. LIMITATION OF ABSTRACT UNLIMITED

NSN 7540-01-280-5500

Standard Form 298 (Rev. 2-89)
Prescribed by ANSI Std. Z39-18
298-102

Preface

This report presents yield measurements of secondary and backscatter energy and angle emission distributions from materials currently used in spacecraft design. The yield data are presented as:

1) differential electron yield for secondary and backscatter electrons:
$$d^2\sigma(E_p,\theta_p,T,E_s,\theta_s,\phi_s)/dEd\Omega \qquad \text{in } \#/(\#.eV.sr)$$

2) secondary electron emission coefficient:
$$\delta(E_p,\theta_p,T) = \text{Integral of } \sigma \text{ over } E_s \ (<50 \text{ eV}), \ \theta_s \text{ and } \phi_s \qquad \text{in } \#/\#$$

3) backscatter electron emission coefficient:
$$\eta(E_p,\theta_p,T) = \text{Integral of } \sigma \text{ over } E_s \ (>50 \text{ eV}), \ \theta_s \text{ and } \phi_s \qquad \text{in } \#/\#$$

where 'T' is the target set examined = { conductors (clean, oxidized, ...), aluminum, copper, carbon, stainless steel and brass}. θ_p is the off normal incident angle, θ_s and ϕ_s are the in-and-out-of-plane emission angles. E_p is the incident electron energy, and E_s is the emitted electron energy. For the data presented here:

$$
\begin{aligned}
500 \text{ eV} &\le E_p \le 6 \text{ keV} \\
0° &\le \theta_p \le 60° \\
0.02 \text{ eV} &\le E_s \le E_p \\
\theta_s &= 45° \\
\phi_s &= 0°
\end{aligned}
$$

Acknowledgments

CONTENTS

SUMMARY

This report presents the status of a machine which has produced yield measurements of secondary and backscatter electrons as a function of emission energy and angle from materials currently used in spacecraft design. The yield data are presented as:

1)   differential electron yield for secondary and backscatter electrons:

$$d^2\sigma/dEd\Omega = f(E_p,\theta_p,T,E_s,\theta_s,\phi_s) \qquad (0.1)$$

2)   secondary electron emission coefficient:

$$\delta(E_p,\theta_p,T) = \int d^2\sigma/dEd\Omega \qquad \text{over } \theta_s, \phi_s \text{ and } 0 < E_s < 50 \text{ eV} \qquad (0.2)$$

3)   backscatter electron emission coefficient:

$$\eta(E_p,\theta_p,T) = \int d^2\sigma/dEd\Omega \qquad \text{over } \theta_s, \phi_s \text{ and } 50 \text{ eV} < E_s < E_p \qquad (0.3)$$

where 'T' is the target set examined = { conductors (clean, oxidized, ...), inorganic insulators (tile, glass, ...), organic insulators (polymers,..., Teflon®, Kapton®,..)}. θ_p is the off normal incident angle, θ_s and ϕ_s are the in-and-out-of-plane emission angles. E_p is the incident electron energy, and E_s is the emitted electron energy.

$$100 \text{ eV} \leq E_p \leq 20 \text{ keV}$$

$$0° \leq \theta_p \leq 80°$$

$$0.02 \text{ eV} \leq E_s \leq E_p$$

$$0° \leq \theta_s \leq 80°$$

$$0° \leq \phi_s \leq 80°$$

Section 1: Introduction

This report presents yield measurements of secondary and backscatter energy and angle emission distributions from materials currently used in spacecraft design. There is a long history of secondary electron and backscatter electron yield measurements (Ref. 1)[†]. Most previous measurements were with metals at low incident electron energies (with a few measurements at energies above ~MeV (Ref. 2)). Relatively few measurements have been made of the energy and angle distributions of the emitted electrons. Almost no measurements have been made with materials used in spacecraft construction, nor have any been made at the energies of interest in the space environment (keVs to 10s of keVs incident energy). Even more limited data is available for insulators and semiconductors used in spacecraft design. The lack of knowledge of the angular dependence of the emission coefficients and the emission properties of actual satellite surfaces (oxidized or contaminated) is one of the major deficiencies in spacecraft charging theory (Ref. 3).

In addition, calculations of neutral particle beam (NPB) interactions with spacecraft (Ref. 4) demonstrated deficiencies in the data base for secondary and backscatter production coefficients and for the energy and angular emissions of electrons due to incident high energy electrons and neutrals (H°). The missing data was the shape of the high energy tail of the emission energy distribution generated by high energy electrons (~30 keV). The assumed

---

[†]   Superscript symbols reference footnotes at the bottom of the page, numbers in parentheses reference endnotes on page 142.

2

electron emission energy distribution has a critical effect (three orders of magnitude) on the potential reached by the target during NPB bombardment.

Spacecraft charging potentials are a strong function of the energy dependance of secondary electron and backscatter electron yields. Presently, two expressions are used for the secondary (δ) and backscatter (η) production coefficients: that by Katz (Ref. 5) and that from Sternglass (Ref. 6) and Prokopenko (Ref. 7). The Katz expression successfully explained the high voltage charging (to ~kV levels) observed with the SCATHA (Ref. 8) (Spacecraft Charging AT High Altitudes) satellite subject to high energy electron flux (~10's keV). This formulation is currently used in the NASACAP (NASA Charging Analyzer Program) and DynaPAC (Dynamic Plasma Analysis Code) spacecraft charging computer programs[†].

$$\delta_K = 1.114*\delta_{max}/\cos(\theta)*R^{0.35}*(1-\exp(-2.28*\cos(\theta)*R^{1.35})) \qquad (1.1)$$

$$\eta_K = S*(1-(2/E)^{0.037*Z} + 0.1*\exp(-E/5000)) \qquad (1.2)$$

with $\qquad$ $S = \ln(E/50)/\ln(20)$ $\qquad\qquad\qquad$ for $50 < E < 1000$

or $\qquad$ $S = 1$ $\qquad\qquad\qquad\qquad\qquad$ for $E > 1000$

where E and θ are the incident electron energy (eV) and angle, $R = (E_{max}/E)$ and E_{max}, δ_{max} and Z are the energy and secondary electron production coefficient for the target material at maximum yield and Z is the atomic number of the target material.

The Sternglass/Prokopenko expression was successful in explaining the high voltage

---

[†] $\qquad$ Information on the NASACAP and DYNAPAC programs is available through Dr David Cooke, AFRL/VSBS, Hanscom Air Force Base, Massachusetts 01731.

3

charging (to ~100 V levels) observed with the DMSP (Ref. 9) (Defense Meteorological Satellite Program) satellite from high energy electron flux (again ~10's keV).

$$\delta_{SP} = 7.4*\delta_{max}/\cos(\theta)*R*\exp(-2*\sqrt{R}) \qquad (1.3)$$

The Katz expression could not explain the DMSP observations, nor could the Sternglass/Prokopenko expression explain the SCATHA observations; either Katz over-predicted or Sternglass/Prokopenko under-predicted the secondary electron and backscatter electron yields. The environments for both satellites were similar: both were in a low density plasma (one near-geosynchronous orbit, the other in low altitude polar orbit), both were in eclipse, and both experience intense high-energy electron flux (one from substorm electrons, the other from auroral electrons).

Differential charging within a spacecraft (between conductors and insulators), and abnormalities present in surface charging in the wake region of a spacecraft are all dependent on the secondary and backscatter electron emission energy distributions and on the integrated production coefficients. With only scant data available, it is the usual practice to assume both distributions are isotropic. This is an adequate assumption for most space environments. If the source is assumed isotropic, detailed knowledge of the emission angle dependance is not required, but the energy distribution is still important. If the 'source' is not isotropic, as in the wake, then the angular dependance of the emission can become important. As discussed above, there is very limited data available for insulators, because it is very difficult to measure the secondary electron and backscatter electron yield coefficients due to surface charging of the

4

insulator.

This report presents measurements of the electron emission yield spectrum (differential in energy and angle) as a function of incident electron energy and angle:

$$d^2\sigma(E_p,\theta_p,T,E_s,\theta_s,\phi_s)/dEd\Omega$$

where E_p is the incident electron energy, and E_s is the emitted electron energy, θ_p is the off normal incident angle, θ_s and ϕ_s are the in-and-out-of-plane emission angles. The measurements are unique in that a number of problems normally associated with this type of measurement have been eliminated. This can be attributed to the technique chosen to measure the energy of the emitted electron, 'time of flight' (TOF). There are many advantages associated with this technique:

a) Simplicity: only length and time need be measured to determine electron energy. This technique can also be used to analyze the energy and charge state of excited or ionized species emitted from the surface by particle bombardment.

b) The measured energy is absolute: problems with contact potentials and work functions between surfaces are eliminated, hence reference energy calibrations are not required.

c) Pulsed electron source: minimizes the effects associated with beam-induced heating of the target, surface and deep charging effects in measurements of insulating surfaces, and energy shifts due to space charge effects.

There are a few disadvantages with this technique:

5

a)   The lowest energy measured was determined by the residual magnetic field along the

flight path and by electrons that 'bounce' around the chamber before detection.

b)   A long flight path is required for good energy resolution at high emission energies.

Excellent energy resolution is possible at low emission energies where the flight time is

long, but the resolution at high emission energies where the flight time is short was

correspondingly poor.

c)   TOF required a pulsed source: an electron packet time width of less than 1 ns FWHM

(driven by the above resolution requirements) is difficult to generate. Also the reduced

duty factor required longer data collection periods (an advantage in reducing target

interaction).

The sections to follow will examine various aspects of the measurements. The design

considerations discussed in Section 2 establish limitations in the measurements. Section 3 is

devoted to a description of the experimental apparatus optimized using the design consideration

(relative to accuracy) discussed in Section 2. Section 4 examines the measurement parameters,

while Section 5 discusses the data acquisition process. Section 6 discusses the calibration of the

apparatus and the potential error sources for the measurements. Section 7 presents the

measurement data for carbon, copper and aluminum targets. Section 8 presents conclusions from

this research.

Section 2: Measurement Considerations

Introduction:

This section will discuss the design parameters important in this type of measurement. The factors which influence the accuracy in the measurement of the energy of the incident and emitted electron, the energy range covered (i.e., the lowest measurable electron energy) and the precision of the emission energy measurement.

Absolute Energy Determination:

The absolute energy of both the incident electron and the emitted electron are needed from this measurement. The kinetic energy of the incident electron (E_p), after it exits the electron gun (e.g., at the center of the vacuum chamber) is given by:

$$E_p = E_1 + E_2 \tag{2.1}$$

where E_1 is the kinetic energy of the incident electron just outside the cathode, and E_2 is the potential energy of the cathode relative to the vacuum chamber surface. E_1 has a distribution of energies determined by the emission process (expressible with a Maxwellian energy distribution with a temperature equal to the cathode temperature):

$$E_1 = +0.04 \pm (+0.28/-0.02) \text{ eV} \tag{2.2}$$

where a cathode operating temperature of 1000 K is assumed and the total width at half height of the distribution is used as a measure of the uncertainty in the emission energy (i.e., the 0.30 eV FWHM term).

7

E_2 is given by the sum of the contact potential differences of the metals in the circuit from the carbon coating on the chamber walls, through the power supply to the tungsten (or oxide coated) cathode:

$$E_2 = e^* \{ |V_{ps}| + \sum \Delta\Phi_{i,j} + \Delta\Phi_{W,C} \} \qquad (2.3)$$

where $\Delta\Phi_{i,j}$ are the contact potential differences between two metals, V_{ps} is the voltage applied to the cathode (measured correctly by a voltmeter) by an external power supply, $\sum$ is over the various metals in the circuit at room temperature, and $\Delta\Phi_{W,C}$ is the difference between the work function of tungsten (at emission temperature) and the carbon coated chamber (at room temperature). The potential change around the circuit ($\sum$) is zero for all metals (if at the same temperature). Only the contact potential differences at the two vacuum interfaces ($\Delta\Phi_{W,C}$) contribute, i.e., vacuum/carbon and tungsten/vacuum:

$$\Delta\Phi_{W,C} = +0.05 \pm 0.21 \text{ V}. \qquad (2.4)$$

where the room temperature values used for Φ_i came from various published tabulations with the range of the published data available (Ref. 10) taken as a measure of the uncertainty in these values.

When the metals are at different temperatures the Seebeck effect needs to be included. These values are not known, nor the temperatures involved[†].

---

†   For example, in the electron gun, a nickel wire (one end near room temperature, the other end near cathode temperature) was used to connect the power supply (copper wires) to the filament (tungsten). A worst case estimate for the Seebeck effect contribution would add ~+0.02 V to the room temperature value (based on the maximum temperature difference and values from high temperature thermocouple tables).

Combining the expression for the contact potential differences (E_2) with the offset and width in the emission energy of the electron (E_1) results in the final offset and uncertainty in the energy for the incident electron beam.

$$E_p = |V_{ps}| + 0.09 \pm (+0.35/-0.21) \text{ eV}. \tag{2.5}$$

Equation 2.5 represents the accuracy in the final beam energy that can be quoted in this measurement (i.e., a measurement at 500 V has an incident electron energy of 500.16 ± 0.28 eV). From the above, it is clear that the uncertainty in the incident energy comes equally from the energy spread in the cathode emission process as from the uncertainty in the knowledge of the work function of the metals used in the apparatus.

A similar examination of the energy of the emitted electron is not needed, since the energy is determined from the time of flight and does not depend on the contact difference between the target and the detector surface[†].

Low Energy Cutoff:

The experiment measures the emission spectrum over an energy range from the incident beam energy (backscattered electrons) to the lowest possible energy (secondary electrons). The energy of the emitted electron is determined by measuring the time of flight from the target surface to the detector surface. The time axis on which the measurement is made consists of

---

[†]   It could be augured that Equation 2.4 should equally apply to the emitted electron energy as to the incident energy, i.e., a correction of 0.05 eV should be applied to the emitted energy scale. This point is considered further in Section 8.

4096 time intervals (or channels) of equal width. The lower limit of the timing precision will be determined by the width in time of each of these channels.

In principle, the lowest measurable energy could be '0 eV.' One just needs to wait for the electron to reach the detector. Most of the secondary electrons produced are in a peak centered below 2 eV emission energy. When compared to the incident beam energy, the emission energies are in a narrow energy range (e.g., in a 2 eV range out of a possible 2 keV range). In comparison, the corresponding flight times cover a very large range (e.g., an electron with an emission energy of 0.1 eV will have a flight time of 5.1 μs while that with an emission energy of 10 eV will have a flight time of 510 ns). Therefore at the lowest energies, the number of true secondary electrons that arrive in a particular time interval (channel) will be very small. The low energy cutoff for the present measurements is determined by one of three processes. The first two processes considered depend on the point (in flight time) at which the true secondary electron 'signal' level reaches the level attributed to a competing 'noise' level process. The third process involves the removal of the low energy electron from the detector aperture.

The first process dominates when the true signal level equals the noise level due to the uniform background generated by the random pulse rate of the detector. A dark current count rate of only 3 cps (typical for the detectors used) will generate a background noise level of almost one count per time channel over a 30 minute data run. The 'dark current noise' level typically equaled the true signal levels at electron flight times longer that 5 μs. This therefore sets the low energy cutoff to an energy value of 0.1 eV.

10

The second process dominates when the true signal level equals the noise level due to high energy electrons reaching the detector by a route other than the straight line path from the target to the detector. High energy electrons that scattered off the chamber walls (and therefore made one or more bounces before entering the detector aperture) arrived at the detector much later in time. These electrons are classified as low energy electrons based solely on the arrival time. During a measurement, it is not possible to distinguish a true low energy electron from a 'late high energy' electron. A second measurement was therefore needed to separate the 'true' secondary electron signal from the 'late' signal. When the target is displaced along the incident beam direction (i.e., the target was moved out of the field of view of the detector), a measurement of the emission spectrum would now be only those electrons that reach the detector by a route other than the 'direct' straight line path. After normalization (for total charged delivered to the target), the 'late high energy' signal was subtracted from the direct measurement[†]. The 'late high energy' noise level typically equaled the true signal level at electron flight times longer that 3 μs. This moves the low energy cutoff to a higher energy value of 0.2 eV.

The third process dominates when the residual magnetic field along the electron flight path deflects the electron out of the detector aperture. Any magnetic field between the target and the detector will deflect the electron from a straight line path and therefore modify the

---

†   There are a number of assumptions in the measurement of the 'late high energy' signal distribution that must be understood. The main assumption was whether, in displacing the target, the 'late high energy' signal was in any way changed. That this was so was indirectly verified by displacing the target both toward and away from the electron gun. The displacement spectrum did not change the normalized 'late high energy' signal.

measured emitted electron energy spectrum. The deflection of the electron in a uniform magnetic field is given by:

$$\Delta R = \tfrac{1}{2} q * L^2 * B_n / \sqrt{(2mE_s)} \tag{2.6}$$

where ΔR is the off axis deflection, L is the flight path length, B_n is the component of the magnetic field <u>normal</u> to the flight direction, q and m are the charge and mass of an electron and E_s is the energy of the emitted electron. For a given magnetic field, the deflection is largest for low energy electrons. The low energy cutoff is here defined (arbitrarily) as the energy at which the emitted electron is just deflected out of the detector aperture by a uniform magnetic field in a direction normal to the flight path. With a detector aperture radius of 10 mm (for the 25 mm diameter MCP detector), a uniform magnetic field normal to the chamber axis (flight path) of 0.1/0.2/0.3 mG results in a low energy cutoff of 0.02/0.07/0.16 eV.

The component of the magnetic field <u>parallel</u> to the chamber axis could cause an electron that was not emitted into the detector aperture to spiral into the detector aperture and again modify the measured emitted electron energy spectrum[†]. In the above analysis, the fields are assumed to be uniform along the entire flight path, which gives a worst case value for the low energy cutoff. Figure 1 is a typical map of the magnetic field along the flight path (i.e., the emitted electron's flight path). H_t is the magnitude of the vector sum of the three rectangular

---

[†]   If the low energy electron angular emission can be assumed to be isotropic, any electrons deflected out of the detector aperture (by a uniform magnetic field) would be compensated, to first order, by an equal number of electrons deflected into the detector aperture. Essentially, the emission angle would be biased by the angular deflection caused by the magnetic field. The angular bias is a function of the emission energy and distorts the emission spectrum.

components of the magnetic field. Although H_y has the largest contribution to H_t, it will have the

least influence on the deflection of the electron from the straight line path to the detector as

emitted electron's velocity is parallel to H_y. The target and detector positions are marked. In all

Magnetic field along chamber axis
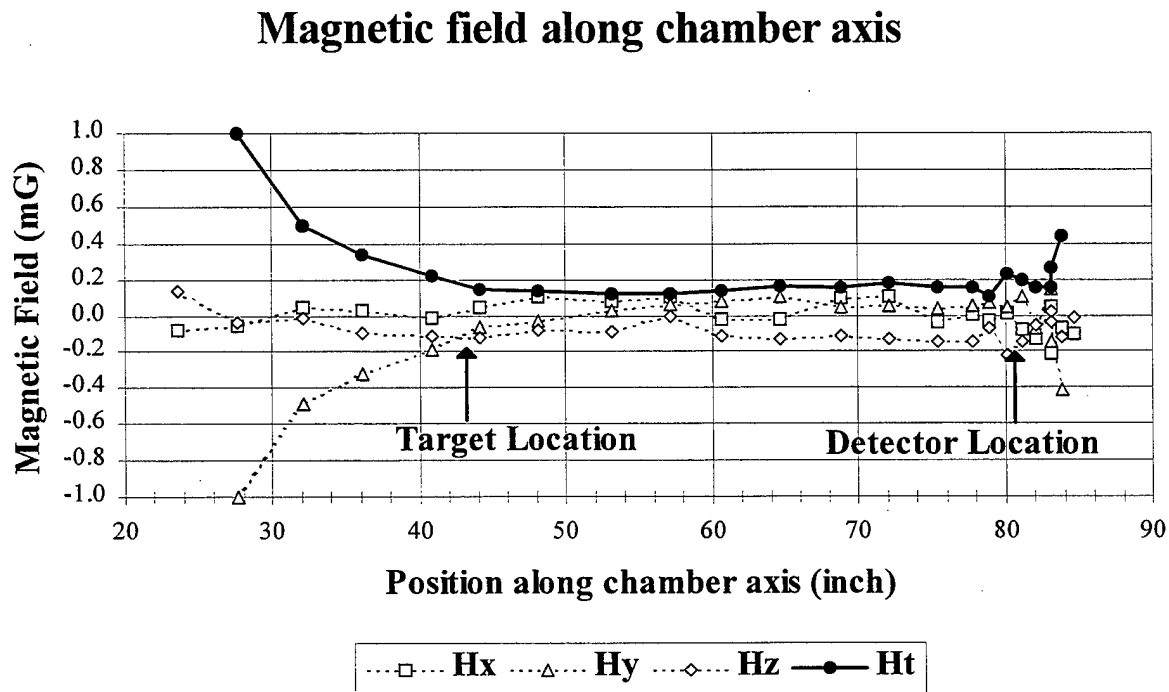
Figure 1: Map of the magnetic field along the chamber axis.

cases, the measured magnetic field was always less than 0.2 mG, and the low energy cutoff due

to this process was always less than 0.1 eV.

Energy Resolution:

The energy of the secondary and backscattered electrons can be determined by measuring

the time of flight (TOF) of the emitted electron. The flight path was assumed to be a straight

13

line[†] along the chamber axis from the target to the detector (L = ~0.95 m). The energy resolution

of the emitted secondary and backscattered electrons was determined from the uncertainty in the

measurement of the flight time (ΔT) and the uncertainty in the measurement of the flight path

(ΔL). These uncertainties are considered independent, and the total uncertainty can then be

obtained by adding each effect in quadrature.

$$(\Delta E/E)^2 = (2*\Delta L/L)^2 + (2*\Delta T/T)^2 \qquad (2.7)$$

Note that the uncertainties related to the flight path are independent of the energy. This

uncertainty will therefore dominate at low emission energies.

The uncertainty in the measurement of the path length (ΔL) has three potential sources.

The first source was the effective 'size' of the target (δL_t), which was related to the size of the

electron beam spot on the target[‡]. The second source of uncertainty is the effective

'length' of the detector (δL_d), which was related to the projected length of the detector input

surface along the direction of the incident electron beam. Two detectors were used during these

---

[†]   Extra effort was taken to keep the local magnetic field less than 0.2 mG and to keep the emitted electrons well away from any surfaces.

[‡] δL_t is the axial length of the electron beam spot on the target as seen by the detector. This equals the beam diameter multiplied by the cosine of the target cut angle (Ω) divided by the cosine of the angle between the normal to the target surface and the incident electron beam (θ_p). With solid targets, the uncertainty in path length always contributed less than 1% to the final electron energy resolution. For example the worst case would be an incident beam skimming the target surface ($\theta = 80°$) and a small target cut angle ($\Omega = 30°$). Under these conditions, $\delta L_t = $ ~5 mm (assuming an incident beam of 1 mm diameter), and $\delta L_t/L = $ ~0.5%. With a gas target, the movement of the focus position and size would have a much larger affect on the energy resolution obtained and would consequently need to be tightly controlled.

measurements: a spiral electron multiplier (SEM) and a pair of micro-channel plates (MCP)[†].

The projected length for a MCP was zero (since the MCP pair was mounted normal to the incident beam direction), while that for a SEM was ~1 mm (due to the length of the input cone). The third source of uncertainty was related to the accuracy with which the total flight path can be measured (δL_p). This also includes the uncertainty of placing the electron beam at the center of the target. For the present series of measurements δL_p was calculated to be less than 0.5 mm. Therefore

$$(\Delta L)^2 = (\delta L_t)^2 + (\delta L_d)^2 + (\delta L_p)^2 \qquad (2.8)$$

$$\Delta L_{MCP} = 5.02 \text{ mm}$$

$$\Delta L_{SEM} = 5.12 \text{ mm}$$

where the worst case contribution to δL_t was used in the above calculations.

The uncertainty in the measurement of the flight time (ΔT) had four potential sources. The first was the time width of the electron pulse at the target (δT_b), which was determined by the injection stage voltage, the slew rate of the sweep pulse and the diameter of the skimmer hole. The second was the uncertainty associated with the time jitter of the detector (δT_d). The timing jitter is related to the physical length of the detector, the shorter the detector the smaller the timing jitter. The timing jitter for the MCP pair was ~30 ps, while for the SEM was ~500 ps. The third source of flight time uncertainty was the timing jitter associated with the electronics used to measure the flight time (δT_e). With care, the electronics uncertainty can be as small as

---

†   Both supplied by Galileo Electro-Optics Corporation, Sturbirdge, MA

~50 ps. For the present set of measurements, δT_e was ~100 ps. The fourth source of uncertainty was associated with the calibration of the time axis (δT_c), which contains the error associated with determining the 'time-zero' channel and the absolute time width of each channel. For the present series of measurements δT_c was ~100 ps. If the value for δT_b from Equation 3.1 (page 38) is used, we have:

$$(\Delta T)^2 \quad = \quad (\delta T_b)^2 + (\delta T_d)^2 + (\delta T_e)^2 + (\delta T_c)^2 \tag{2.9}$$

$$(\Delta T_{MCP})^2 \quad = \quad (0.53)^2 + (0.14)^2 \ ns^2$$

or $\quad \Delta T_{MCP} \quad = \quad 0.55 \ ns$

$$(\Delta T_{SEM})^2 \quad = \quad (0.53)^2 + (0.52)^2 \ ns^2$$

or $\quad \Delta T_{SEM} \quad = \quad 0.74 \ ns.$

Fortunately, the total energy resolution can be measured directly. The time width in the X-ray flash generated when the incident electron beam packet hits the target contains all of the above uncertainties except those associated with the flight path length uncertainty (δL_p) and the calibration uncertainty of the flight time (δT_c). The X-ray flash was also used as a fiducial to determine the 'time-zero' location on the measured time axis. Each data set included an X-ray flash which allows one to monitor and calibrate the energy resolution for a data run.

For each measurement, the time of flight spectra were recorded using two separate time axes. The first time axis spanned 150 ns and was centered about the time-zero channel (referred as 'short') and was used to measure, at high time resolution (~40 ps/channel), the X-ray flash and the high energy emission electron spectra. The second time axis spanned 6 μs and also included

16

the time-zero channel (referred to as 'long'). This axis was at a much lower time resolution (~1.5 ns/channel), but contained the entire emission energy spectra. Figure 2 shows a typical X-ray
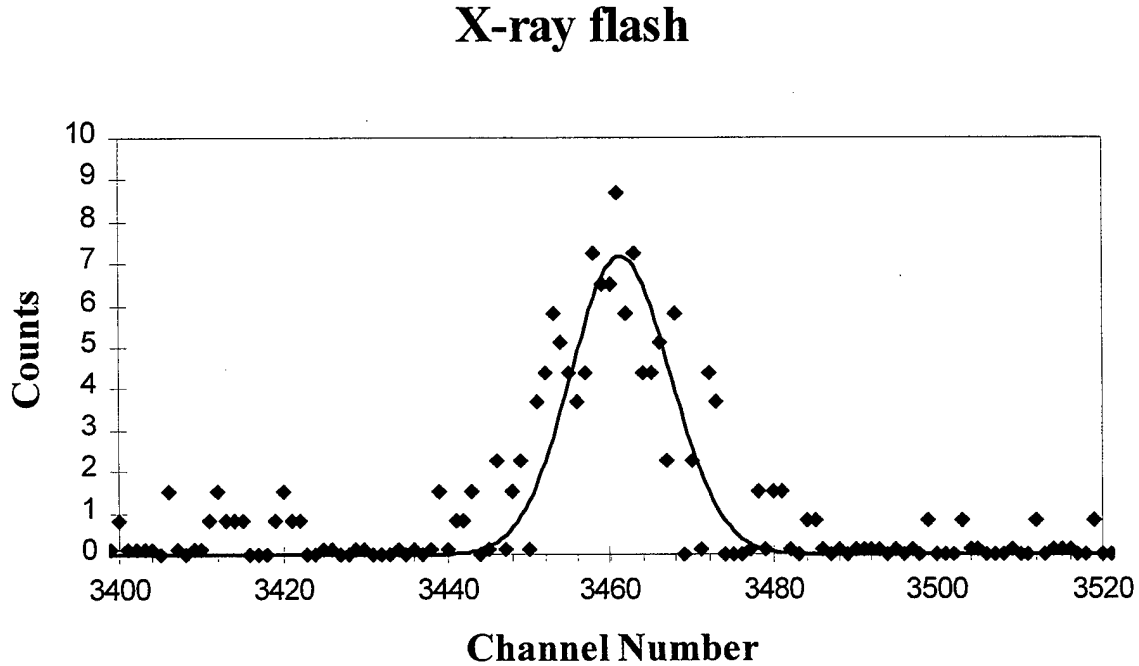
Figure 2: X-ray flash measured using the 'Short' time axis.

flash taken from the short time axis measurement. Figure 3 shows a plot of the energy resolution of the emitted electron ($\Delta E/E$) as a function of electron energy. At low emission energies, the dominate contribution to ΔE comes from uncertainty in the measured flight path length ($\Delta L = 5$ mm), while at high emission energies, the dominate contribution comes from uncertainty in the measured time of flight ($\Delta T = 0.6$ ns). As seen, the cross over from ΔL dominance to ΔT dominance occurs near 280 eV (0.1 μs).

In summary, the absolute energy of the incident electron beam is given by Equation 2.5.

The lowest possible emission energy for the present measurements is determined by the late

arrival of high energy electrons (i.e., the 'late high energy' electron spectrum) and therefore both

a direct and 'offset' spectrum were made for each measurement. The energy resolution for

emission energies above ~300 eV is determined by uncertainties in the flight time measurement

(ΔT) while, at energies below ~300 eV, will be determined by the uncertainty in the measured

flight path length (ΔL).

Energy Resolution

Figure 3: Emitted electron energy resolution (ΔE/E) as a function of electron energy.

The following section will examine how the above considerations were incorporated into

the design of the experimental apparatus.

Section 3: Machine Description

Introduction:

This section will discuss the physical description of the apparatus used to make the

secondary and backscattered electron emission measurement. The scattering geometry is

examined first. The geometry places restrictions (predominantly in scale) on the vacuum

chamber discussed next. The requirements placed on stray electric and magnetic field internal to

the vacuum chamber are then examined. Next the internal components are examined: the

electron gun (the source of the electron packets), the electron detector (Faraday trap) and the

beam trap. The section ends with a discussion of the high voltage supply system.

Scattering Geometry[†]:

The experiment requires making secondary electron yield measurements which are

differential in emitted electron energy and angle as a function of incident electron energy and

angle. The flight path length was considered the most important parameter, as it ultimately

determines the energy resolution of the measurement at high emission energies. The target-to-

detector distance chosen was a compromise between 'as-far-as-possible' (to improve energy

resolution at high emission energies) and 'as-close-as-possible' (to reduce the flight time of the

lowest electrons of interest). A flight path of ~1 m was considered adequate for energy

---

†   Throughout this report, θ_p, θ_s and ϕ_s (all small with subscripts) refer to the incident primary (p) electron beam angle and the emitted secondary (s) electron emission angles measured from the target surface normal. Θ, Φ and Ω (all caps) refer to the machine angles: electron gun angle, target rotation angle, and target cut angle.

resolution, and enabled a resolution of 0.2% at 1 eV and 9% at 15 keV (a 5.1 μs flight time for a 0.1 eV electron).

Furthermore the electron gun-to-target distance chosen was a compromise between 'as-close-as-possible' (to reduce space charge spreading of the incident electron beam at low energies) and 'as-far-away-as-possible' (to allow emission angle measurements close to the incident angle). An electron gun to target distance of 10 cm was considered adequate and would enable emission measurement to within 10° of the incident electron beam.

An obvious experimental geometry would be to mount the target on the floor of the vacuum chamber and the electron gun and detector on structures that place them individually at any location within the hemisphere above the target plane. Such an arrangement would allow the incident angle (θ_p) and the emission angles (θ_s, ϕ_s) to range over the entire phase space available, i.e., the complete forward hemisphere or a full 2π sr solid angle. Such an arrangement gives the most freedom of choice between the various incident and emission angles, but unfortunately required a very complicated structure on which to mount the detector and electron gun. This geometry would also require the chamber to have a diameter of over 6'. As the energy was determined from time of flight measurements, the entire flight path from the target to the detector would need to be free of stray magnetic and electric fields (i.e., a residual magnetic field less than 0.2 mG and a residual electric field of less than 5 mV/m over the various flight paths), i.e., the entire chamber volume.

20

The magnetic field requirement was the most difficult to obtain and was ultimately the driver in choosing the final geometry. The magnetic field along the axis of a long, thin cylinder was the easiest to control. The length of the cylinder was governed by the flight path requirement (1 m). The diameter governed by the length of the electron gun (~10 cm) and the distance to the target (10 cm). The final design chosen was a cylinder 5' long and 3' in diameter (these dimensions were ultimately determined by the size of the largest lathe in the machine shop). The electric field requirement was easily obtained by coating the entire chamber surface with graphite.

The electron detector was mounted, on axis, approximately 6" from one end of the cylinder, and the electron gun was mounted on a rotating table with the vertical axis of rotation intersecting the chamber axis approximately 1½' from the opposite end of the chamber (i.e., 1' from the center of the cylinder). With the detector fixed in space (on the chamber axis) and the rotation of the incident electron gun limited to the horizonal plane, complete coverage of the incident/emission phase space could still be obtained if the target were mounted on a three axis goniometer. This arrangement could not be chosen for two reasons: 1) extensive hardware was required to control the goniometer and 2) the target exchange had to be made without venting the main chamber[†]. Therefore the target was mounted so it could easily be removed to another

---

[†]   The electron gun originally chosen used an oxide coated cathode. This cathode surface, once activated, could not be exposed to air without a loss of emission efficiency (oxygen and water vapor would poison the oxide surface). In addition, once the chamber was opened, it required a minimum of 12 hours to pump it down to 5×10^{-7} Torr (needed to reduce the poisoning of the oxide surface at operating temperatures).

(smaller) chamber. The smaller chamber was isolated from the main chamber, vented to

atmospheric pressure, the target replaced, and finally the small chamber was again pumped down

to high vacuum. The new target was then reinserted into the main chamber.

The goniometer design was replaced by a simpler system which still enabled coverage of

almost (but not) all of the available phase space. Here, the target was mounted in a holder at the

Electron Gun-Target-Detector
Top View
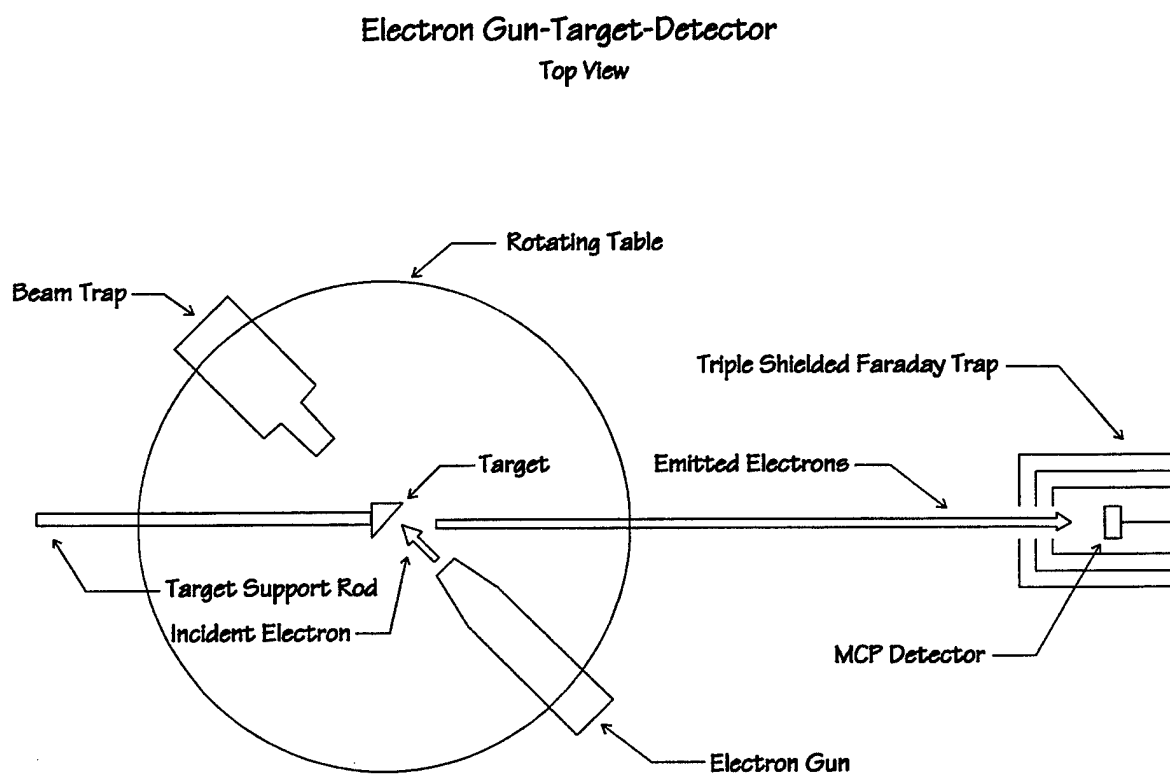
Figure 4: Overhead view of the scattering geometry.

end of a rod which was placed coaxial with the chamber. The holder was, in turn, mounted at a

fixed angle (Ω) to the rod axis (which determines the emission angle). As the electron gun was

rotated (Θ), various incident and emission angles (θ_p, θ_s and ϕ_s) are selected. As the target was

rotated (Φ) about the chamber axis, a different set of incident and emission angles are selected[†].

This arrangement was much simpler than the goniometer, while still allowing measurement of

out-of-plane emission. The out of plane measurements are useful for systematic checks and to

examine expected backscattered structure at higher emission energies. Figure 4 is a diagram of

the electron-target-detector geometry. The electron gun/beam trap move about the target on a

rotating table. The target can be rotated about the target support rod. The MCP detector is

mounted on the chamber axis and is fixed in space.

Figure 5 shows the phase space addressable by θ_p, θ_s and ϕ_s. Θ is the machine angle

corresponding to the rotation of the electron gun about the target ($0° \leq \Theta \leq 170°$), Φ is the

machine angle corresponding to the rotation of the target about the chamber axis ($-75° \leq \Phi \leq 75°$)

and Ω is the "cut" angle of the target surface relative to the chamber axis ($15° \leq \Omega \leq 90°$). The

allowed ranges of Θ, Φ and Ω are determined by restrictions in machine geometry. θ_p (small Θ),

is the incident angle relative to the normal to the target, θ_s (small Θ), is the emission angle

relative to the normal to the target and ϕ_s (small Φ), is the angle between the scattering planes.

---

†   As will be seen from Figure 5, almost all of the forward hemisphere is available to θ_p, θ_s
and ϕ_s. A problem exists in the ability to preselect a particular set of values for θ_p, θ_s and ϕ_s.
This is because the final scattering angles are very sensitive to small changes in the machine
angles Θ, Φ, and Ω at particular values for Θ, Φ, and Ω : e.g., at $\Omega = 45°$, $d\phi_s/d\Phi$ ranges from -
0.8 to +6.6 while $d\phi_s/d\Theta$ ranges from 1 to over 20. Since the ability to set a machine angle Θ, Φ,
or Ω is at most ±1°, this would correspond to an uncertainty of as much as ±20° at particular
combinations of Θ, Φ, and Ω .

The scattering angles available as Θ, Φ and Ω vary through there respective ranges are: $0° \leq \theta_p \leq 90°$, $0° \leq \theta_s \leq 75°$ and $-90° \leq \phi_s \leq 90°$. The plot in Figure 5 (ϕ_s vs θ_p) was generated by allowing

Angle between incident plane and emission plane
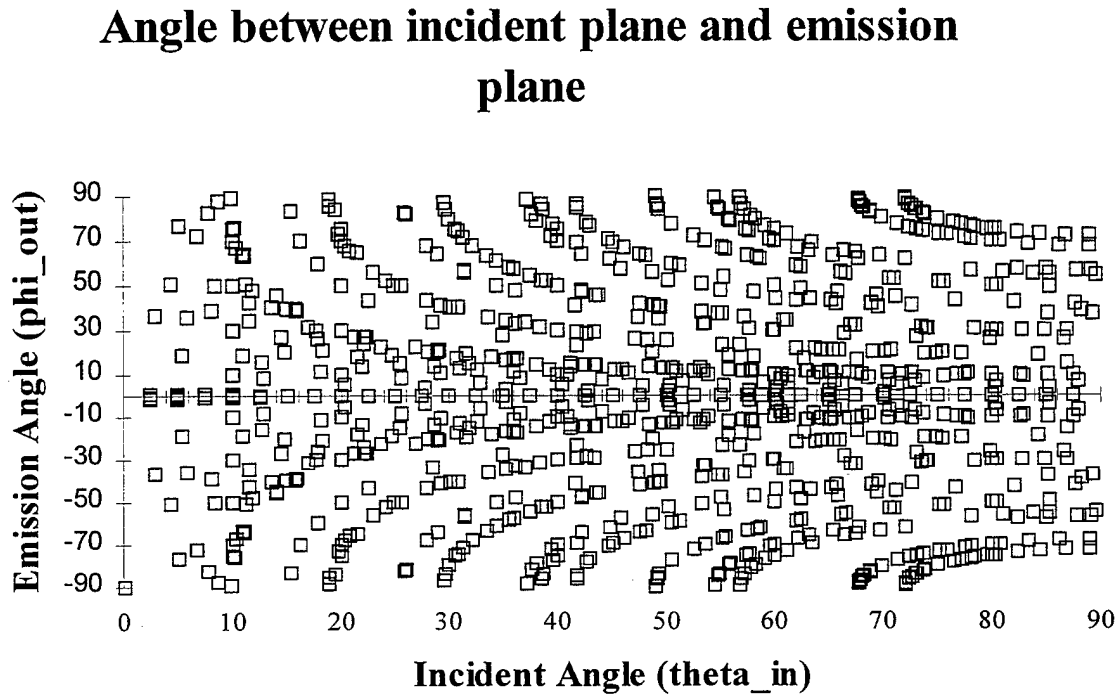
Figure 5: Phase space (θ_p, θ_s ϕ_s) addressable by Θ, Φ and Ω

Θ, Φ and Ω to vary over their respective ranges.

Vacuum Chamber:

The quality (composition of the rest gas) and the quantity (total vapor pressure) of the vacuum in the experimental chamber established operational limits for various experimental parameters. The lifetime of the oxide coated cathode used in the electron gun was limited due to poisoning by water vapor, oxygen and various hydrocarbon compounds present in the rest gas.

24

In addition, the buildup of insulating contaminants[†] on vacuum surfaces may become charged with electron bombardment and effect the stability of the incident electron beam or generate electric fields along the flight path (i.e., deflect low energy electrons away from the detector aperture). Contamination of the target surface under test directly effects the work-function of the target material and thereby modifies the low energy emission spectrum. Another consequence attributed to contamination is the buildup of conducting layers on insulating surfaces used in the Faraday trap (here the leakage resistance must remain above 10 TΩ).

The vacuum chamber was designed with the following characteristics:

1) a low outgassing rate: this is determined by evolution of gas from the materials used in the construction of the vacuum chamber and internal components (care was taken with vacuum welding and material selection).

2) a low base pressure: this background pressure is usually dominated by the evolution of adsorbed water from the chamber walls and diffusion of atmospheric gases through the O-rings (double O-ring grooves were used when needed).

3) bakeable to at least 100°C (high temperature helps in removing water contaminations from the vacuum chamber walls)

4) large enough to keep any emitted electrons far away from any surfaces along the flight path to the detector (reduce local electric fields seen by the emitted electron)

5) a low residual magnetic field over the flight path from the target to the detector (reduce local

---

† Most notability, inorganic compounds which crack under electron bombardment, forming electrically insulating surface coatings.

magnetic fields seen by the emitted electron).

Figure 6 is a simplified diagram of the chamber. The internal dimensions are 3' diameter by 5' long. The chamber is mounted with the chamber axis 6' above the floor. The trolley seen
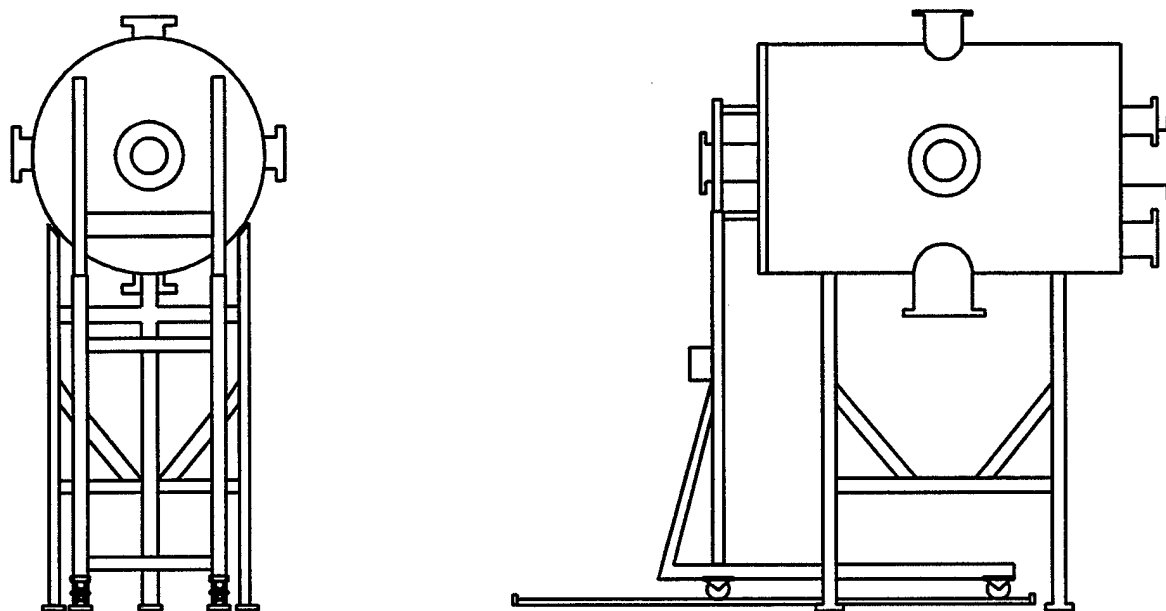
Figure 6: Chamber diagram.

at the left in the figure supports the chamber door when the system is vented to atmosphere.

The experimental apparatus was housed in an all aluminum chamber constructed from a 3/8" thick sheet bent and welded into a cylinder with an interior diameter of 90 cm and length of 150 cm. One end was sealed with a 3" thick flat flange welded to the main cylinder while the other end was sealed with a similar flange bolted to the main cylinder and used as a door. The

welded flange had 4 ports: an ISO-200 port, mounted on axis, and three ISO-160 ports, mounted about the chamber axis (spaced 120° apart starting from the bottom). The door flange had a single ISO-160 port mounted on axis. In addition, the cylindrical section of the chamber had four ports located in a plane normal to the chamber axis cutting through the middle of the chamber. A large ISO-250 port was mounted at the bottom, with the three small ISO-100 ports spaced at 90° intervals about the chamber axis. The interior volume of the main chamber was approximately 1 m^3.

The chamber was designed to be pumped with a 10" oil diffusion pump[†], but for the present series of measurements (with metal targets), an 8" cryo-pump (CTI Cryogenics CRYO-TORR 8) was used. The vacuum pump was mounted on an 8" gate valve adapted to the bottom ISO-250 port. After baking the chamber at 90°C for 6 hours, the empty chamber had an outgassing rate of 2×10^{-10} Torr*l/sec*cm^2 (i.e., a pressure rise of 7×10^{-7} Torr/min when the valve between the chamber and the cryo-pump was closed). Any higher baking temperature would accelerate the decomposition of the O-rings. Four heating tapes were wound on the outside of the chamber, with 6" of insulation covering the entire chamber. The chamber was supported on six short legs and thermally isolated (using marble slabs) from the main chamber support frame. After heating, the chamber required over 24 hours to return to ambient temperature.

[†]   An Edwards Diffstak 250/2000 unit. In future experiments, gas targets were to be used and a high gas throughput would be needed.

Greaseless elastomer O-rings were used throughout the chamber. The residual gas load

for the vacuum chamber was calculated as dominated by diffusion of atmospheric gases through

the O-rings and not from outgassing of the O-rings themselves. The choice of which O-ring

elastomer (Viton or Buna-N) to use was based on the diffusion coefficient. Buna-N had a

smaller gas diffusion coefficient, although a larger outgassing rate, than Viton. Figure 7 is a plot

of the residue gas mass spectrum. The line at m/q = 1 is from hydrogen, the lines at m/q = 16, 17

Vacuum Chamber Spectrum
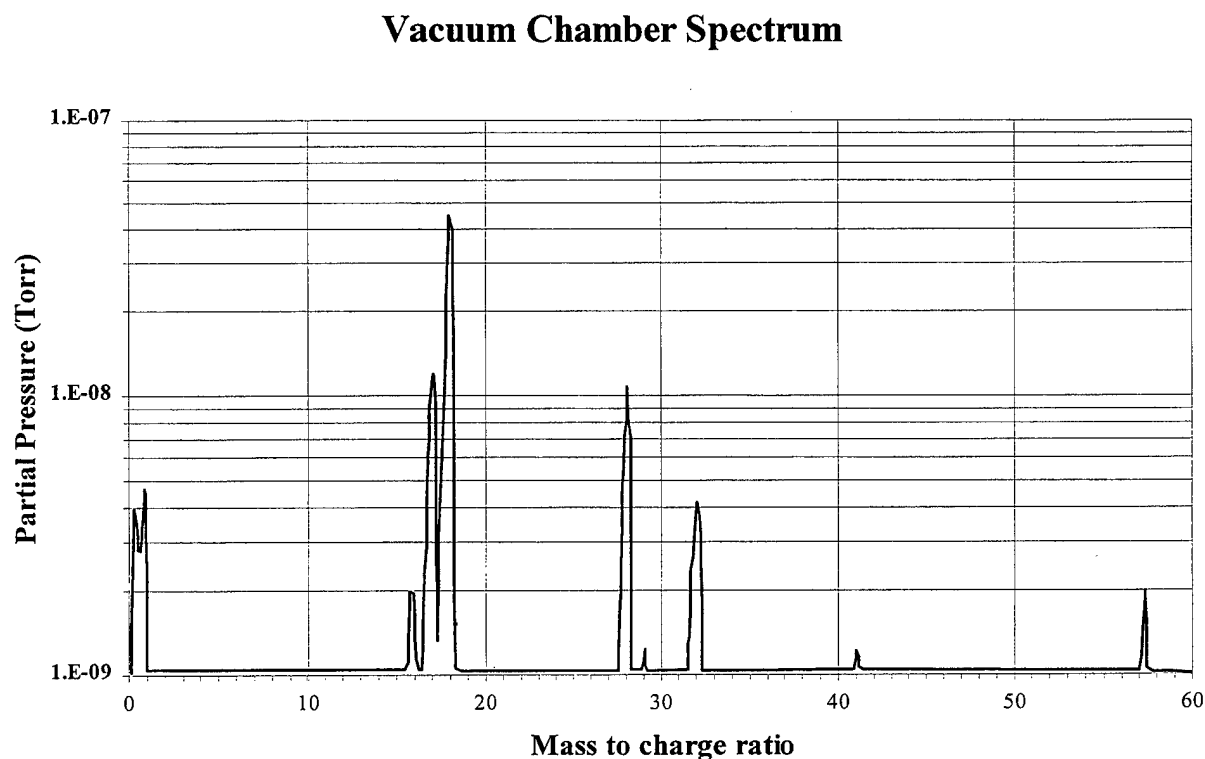
Figure 7: Residue gas mass spectrum.

and 18 are from water, the line at m/q = 28 is from molecular nitrogen, the line at m/q = 32 is

from molecular oxygen. The appearance of the lines at 28 and 32 indicate a leak in the vacuum

system; the water lines result from adsorption of atmospheric water vapor by the vacuum system

when vented to the atmosphere. The lines at m/q = 29, 41, 57 are from organic solvents that were previously used to clean the chamber surfaces and vacuum components (e.g., Acetone). The residual gas was dominated by water vapor (98%), then air (2%) followed by trace amounts of hydrocarbon compounds.

The largest O-ring used was that on the door flange of the chamber (3/8" cross section diameter). To reduce the gas load from diffusion through this O-ring, the door was machined with a double O-ring groove. The gap between the two O-rings was pumped to eliminate the diffusion of air through the inner O-ring. The outgassing value stated above was obtained without using the outer O-ring groove.

In normal operation, the chamber was vented with filtered (0.5 μm pore diameter), dried air[†]. After venting to atmosphere, the chamber normally required 12 hours of pumping to reach 4×10^{-7} Torr. The minimum vacuum pressure reached was 8×10^{-8} Torr. The normal operating vacuum pressure, with all internal components present, was 2×10^{-7} Torr.

A small aluminum target chamber (30 cm long by 18 cm internal diameter) with an 8" gate valve was mounted on the ISO-200 port. This chamber allowed the exchange of targets without the necessity of venting the main chamber. The target was attached to a support

---

†   Initially, oil-free nitrogen was used to vent the vacuum chamber to eliminate the exposure of the oxide coated cathode to oxygen. Unfortunately this technique did not appreciably lengthen the lifetime of the oxide coated cathode.

mounted on the end of a hollow brass rod[†] (5/8" diameter). The brass rod was 6' long and allowed placing of the target near the center of the main chamber. To exchange targets, the brass rod was withdrawn from the main chamber into the target chamber, the gate valve between the two chambers was closed, and the target chamber vented. The vacuum seal between the brass rod and target chamber end flange was developed using a double O-ring seal with differential pumping between the O-rings. The elastometers used were Teflon coated, India rubber O-rings. Teflon was used to permit easy movement of the rod over the 4' draw, the India rubber was needed to give the Teflon surface some elastic properties (even though the rod was uniform in cross section to ±0.0015", without this elasticity, bursts of gas would enter the main chamber as the brass rod was moved due to the changing cross section of the brass rod).

Complete access to the entire interior volume of the main chamber was available through the 3' diameter end flange. The end flange was mounted on a support frame that rolled in a track and allowed the entire flange to move away from the chamber. The door flange had alignment pins used to locate the door relative to the chamber axis (the detector was mounted in the ISO-160 port on the door) as reproducible alignment relative to the chamber axis was required.

Electric Field:

All of the chamber surfaces (except the target surface and target support) were coated

---

[†]   A hollow rod was used as the deflection from its own weight was less than that of a solid rod.

with Aerodag[†]. This material, as well as reducing contact potential problems, provided an additional advantage in that the secondary electron production coefficient for carbon is very low compared with that for most metals (conductors). Therefore the production of secondary electrons at the chamber wall by stray incident or emitted electrons is reduced. This means that the number of electrons that may, after repeated bounces, be detected and classified as low energy electrons, is greatly reduced (these are the 'late high energy' electrons discussed in Section 2).

Magnetic field:

The size of the magnetic field was important in two regions in the vacuum chamber. The first was along the incident electron beam axis, i.e., from the exit aperture of the electron gun to the bottom of the beam trap, a distance of ~50 cm. As the incident electron gun was rotated about the target, the beam axis sweeps out a disk shaped region centered on the target location. Any magnetic field here will effect the flight of the incident electron beam. Equation 2.6 gives the deflection due to a uniform magnetic normal to the flight path. Assuming a maximum residual magnetic field of 0.5 mG (worst case) and an incident electron beam energy of 100 eV (lowest examined here) would result in a net deflection of 0.15 mm. The entrance aperture diameter of the beam trap was 13 mm, therefore the deflection of the incident electron beam was insignificant.

[†]   Aerodag G is a aerosol suspension of graphite in alcohol with a CO_2 propellent manufactured by Acheson Colloids Company, Port Huron, MI.

The second region of importance was along the chamber axis, from the target to the electron detector. The residual magnetic field along the emitted electron flight path was required to be less than 0.2 mG. The magnetic field in this region will effect the low energy cutoff for the emitted electrons. (See the discussion of "Low energy cutoff" in Section 2.)

Conservative calculations indicated that three shields were needed to reduce the earth's magnetic field from the nominal 700 mG to the 0.2 mG field (a total attenuation of 3,500:1). In these calculations, the chamber was approximated by either an infinitely long cylinder or a sphere. Both models ignored the effect of the holes for the vacuum ports. In addition, the value used for the permeability of the magnetic material was that quoted by the manufacturer. Any mechanical stress of the magnetic material (generated in cutting and deforming the metal to match the chamber) reduced the permeability from the quoted value. As any calculation of the magnetic field attenuation (using either model, ignoring the effect of the holes and the reduced permeability) was overly optimistic, it was thought best to over shield the chamber.

The need for the third outer shield was eliminated by using three sets of Helmholtz coils[†]. The dimensions of the chamber and the laboratory space available drove the chamber to be positioned with the chamber axis 6' above the floor and the size of the Helmholtz coils to be approximately 12'x20' on a side[‡]. The shielding calculations indicated that the attenuation of a

---

†   Due to funding restrictions.

‡   The field from a Helmholtz coil pair is uniform to 1% over a volume defined by 10% of the radius of the coils. This rule also holds for the rectangular coil pairs used here (based on field

magnetic shield in the shape of a cylinder was worse for the component along the cylinder axis. The chamber and the coils were therefore positioned so that the smallest component of the earth's magnetic field was along the chamber axis. The currents in the three Helmholtz coils were adjusted to zero the local field at the center of the chamber. The bucking field generated by the Helmholtz coils reduced the local magnetic field strength from 700 mG to less than ±50 mG over the volume occupied by the chamber. With the local magnetic field reduced, the magnetic shielding need only attenuate the remaining field by ~250:1.

The above calculations are valid for both variable (AC) and static (DC) magnetic fields. Eliminating the third shield by reducing the local magnetic field worked only for the DC magnetic field. A local AC magnetic field was present in the chamber area due to high current-carrying cables in cable trays near the ceiling of the laboratory area. The peak-to-peak magnetic field was measured as 90 mG at 60 Hz. The penetration of the AC field into the chamber volume was attenuated by two mechanisms. The first was the direct attenuation of the two magnetic shields (~250:1 based on the measured DC residual field). The second was a reduction of the magnetic field due to induced eddy currents in conducting medium. A calculated attenuation of ~5:1 for each of the two layers of magnetic shield material (0.020" wall thickness) and ~3:1 for the aluminum chamber (3/8" wall thickness). The expected AC magnetic shielding factor should be ~18,000:1 (=250*5*5*3). The AC magnetic field strength measured on axis at the center of the chamber was less than 0.01 mG, this was in fact the lower limit set by noise within the

---

calculations using Mathematica).

magnetic field probe itself[†].

The chamber was surrounded by two layers of magnetic shielding metal[‡]. The 0.020"
thick magnetic shielding only came in 30"x120" sheets. Therefore the sheets were positioned
over the chamber outer surface with the sheets touching throughout a 2" overlap between
adjacent sheets (which improved the flux linkage between adjacent sheets[§]). The shield on the
movable door required special treatment. The gap between the door sheets and the chamber
sheets was increased from 0" to ½" and the door sheets were designed with a 4" overlap with the
adjacent sheets on the cylinder.

The inner shield was mounted flush against the outside of the chamber wall. The 3"
space between the inner and outer shield was filled with thermal insulation. The outer shield was
covered with an additional 3" of thermal insulation. Each magnetic shield also had the holes for
the vacuum ports and the support legs punched in them. Any such hole allows an external

---

[†]   The triaxial magnetic field probe (fluxgate sensor) was model MAG-03MC supplied by
Bartington Instruments LTD, Oxford, England.

[‡]   Type AAA supplied by the Eagle Magnetic Co. of Indianapolis, IN. This shielding
material had magnetic properties that are similar to Co-netic AA which is the most commonly
used magnetic shield material (and the most expensive).

[§]   The flux linkage between adjacent sheets must be made with a minimum reluctance for
maximum shielding. Reducing the gap between adjacent sheets and increasing the contact area
will reduce the reluctance between sheets. The preferred method would be to butt weld the
sheets followed with a heat treatment at 1000°C. The butt welding reduces the joint reluctance to
zero while the annealing process returns the permeability of the magnetic material to the high
value initially quoted by the manufacturer.

magnetic field to penetrate into the interior volume of the chamber. To reduce the field penetration, each hole (cylinder tube) was lined with two additional layers of magnetic shielding material.

All but one porthole were well removed from the electron flight path, and any external field penetration into the chamber axis by these holes was minimal. The porthole for the detector had the worst geometry for field penetration. It was large (6" diameter), on-axis and the electron flight path extended up to within 6" the main chamber door. The penetration of the external field normal to the chamber axis due to the detector porthole was reduced by adding another pair of magnetic shields. The shields (18" diameter by 24" long) surrounded the detector housing mounted on the outside of the door flange. The added shield successfully extended the 'zero' field (but only for components normal to the flight path) up to within 2" of the main chamber wall (i.e., 4" behind the detector located at the end of the emitted electron flight path). The added shield had only a minimal reduction in the axial component of the penetrating field (discussed below).

The assembly (cutting, forming, stressing, ...) or simply moving one shield relative to another (i.e., opening the chamber door) would result in the magnetic shield material becoming slightly magnetized. To remove this residual magnetic field, the shields must be demagnetized or de-Gaussed. The degaussing process involved taking the magnetic material into saturation by

applying a slowly alternating magnetic field[†]. The field was then slowly (compared to the cycle frequency of the alternating field) reduced to zero. The cycling current in the degaussing coils effectively walks the magnetic material down the hysteresis curve and leaves the shield with zero residual field. The degaussing coils must generate a magnetic field strength of at least 0.1 Os to bring the magnetic material into saturation.

Since it was important that no residual magnetic field remain after degaussing, the inner magnetic shield used two different degaussing coil geometries. The first was wound toroidally around the shield (the central cylinder and the two end caps). The second coil was wound radially. It was not certain that the radially-wound coil would degauss the inner shield completely, therefore the second degaussing toroidally-wound coil was added. The outer magnetic shield was wound with a single radially-wound coil. Each of the portholes also had separate degaussing coils. The magnetic field strength generated by current in the degaussing coils was ~0.2 Os/A (a calculated value based on a 3 cm spacing between successive windings of the degaussing coils). Therefore, a 1 ampere (peak-to-peak) current was needed to degauss the shields completely. Based on the final residual field measurement, the inner shield was degaussed successfully using only the radially-wound coil.

---

†   Any frequency will do, but higher frequencies will induce eddy currents which effectively reduce the penetration of the degaussing magnetic field into the magnetic shield metal. At 60 Hz, the skin depth for the Eagle AAA material was 0.01" while that for the aluminum chamber wall was 0.02." (This same physics was used as an advantage to reduce the external AC field penetration.)

With the two magnetic shields in place and degaussed, the residual magnetic field measured along the electron flight path was less than 0.2 mG. The major component of the residual magnetic field was due to fields along the chamber axis (as anticipated). The field component was parallel to the electron path and therefore results in the smallest effect on the flight path of a low energy electron. To reduce the axial component to less than 0.1 mG, a small bucking permanent magnet was place downstream on the chamber axis (approximately 3' from the detector location). The final distance from the detector position was chosen to force the axial magnetic field at the detector location to 'zero.' This may seem klutzy, but with the magnet in place, the magnetic field over the entire flight path was less than 0.15 mG.

Electron Gun:

Table 1   Electron Gun Requirements

Energy Range:	100 eV to 20 keV
Energy Width:	< 0.3 eV FWHM
DC Fluence:	> 50 nA over energy range
Focus Position:	~ 10 cm beyond last lens element
Focus Diameter:	< 1 mm FWHM at target position
Beam Pencil Angle:	< 0.5°
Pulse Fluence:	~ 20 pA DC equivalent
Pulse Time Width:	< 1 ns FWHM
Pulse Rate:	up to 1 MHZ
Time Pickoff:	< 50 ps FWHM jitter
Construction:	non-magnetic
Incident Angle:	rotate a full 180° about target position

Table 1 lists the parameters that the electron gun was to meet. Each of these requirements are discussed in the following paragraphs.

37

Electron Packet Generation:

The generation of an electron packet with a FWHM of <1 ns by the direct application of a pulse to a grid element would require a transmission bandwidth near 1 GHz. Retaining such a bandwidth is difficult to do[†]. The transmission bandwidth requirement can be reduced to less than 200 MHZ by using a "trick." The injection electron gun has two pairs of electrostatic deflection plates. A small aperture (the skimmer, with a diameter, $D \approx 1.1$ mm) was mounted on the electron gun axis ≈ 9.7 cm (L) from the deflection plates. The DC electron beam was focused on the center of this aperture. When a DC bias ($X_0 \approx +5$ V) was applied to one of the first pair of deflection plates (plate separation, $h \approx 1.5$ mm and length, $l \approx 3$ cm), the DC beam was deflected and no longer passed through the aperture. Then when a pulse with a peak voltage larger than the bias voltage (typically $V_{peak} \approx +10$ V with a rise time $T_r \approx 3$ ns) was applied to the remaining half of the first deflection plate pair, the DC beam sweeps back across the aperture. The electron packet transmitted by the aperture as the DC beam sweeps across the aperture had a time width (δT_b) given by:

$$\delta T_b = T_r * V_{anode}/V_{peak} * (D+d) * h/[(l/2)^2 + (l/2)*L] \tag{3.1}$$

where eV_{anode} is the energy of electron beam at the deflection plates and d is the electron beam diameter (≈ 0.3 mm). Using the above values, the calculated time width (FWHM) of the transmitted electron packet is 0.7 ns. In principle, the time width (δT_b) can be made as small as necessary to obtain the required energy resolution. The packet time width can be decreased by 1)

[†] The additional requirements that the cathode, and therefore the electron gun where the electron packet will be formed, needs to be floated at DC voltage levels up to -20 kV and the electron gun along with its supporting hardware must be mounted inside of the vacuum chamber on a rotatable table, added to the difficulty.

increasing the slew rate of the sweep pulse V_{peak}/T_r, which can be done either by increasing V_{peak} or by decreasing T_r[†], 2) decreasing the electron beam energy (V_{anode}), 3) decreasing the aperture diameter (D), or 4) increasing the distance from the deflection plate to the aperture (L)..

An additional advantage of this procedure was that all beam adjustments and measurements (the beam focus position and diameter) can be made using a DC beam. This greatly simplified the required diagnostics, as the measurements need not be made on a nanosecond time frame with picoampere currents. There is an assumption made in going from DC beam to pulse beam operation: any space charge effects in the transmitted DC beam must be negligible. This meant no appreciable space charge voltage depression was present anywhere along the electron beam path. For the measurements discussed here, the nominal DC current was always less than 20 nA and, even at the lowest final beam energy (100 eV), the space charge effects were calculated to be less than 1 mV.

Lens System:

The variable energy (100 eV to 20 keV) electron gun consisted of three sections: an injection or input stage, a focusing or intermediate stage and a uniform lens or output stage. The input stage was the electron gun from a Tektronix oscilloscope followed by the skimmer aperture. This stage included an einzel lens system to image the cathode on the skimmer

---

[†]   The latter will increase the transmission bandwidth required.

aperture[†] and two sets of deflection plates to sweep the DC beam across the skimmer aperture. The skimmer aperture was the last element in the input stage and served as the object for the following intermediate stage. The intermediate stage also had two sets of deflection plates to adjust beam location and a telefocal lens system to focus the beam on the target. The output stage consisted of an 'energy add' lens system to bring the exit beam energy to the required level.

The electron gun of the injection section was modified by replacing the oxide coated cathode with a tungsten cathode (using a modified filament from a commercial electron microscope). This was necessary because of the limited lifetime of an oxide coated cathode. An oxide coated cathode will become poisoned and (Ref. 11)[‡] typically nonfunctional after six vacuum-atmosphere cycles (only slightly more if vented with dry nitrogen). But the real driver that forced the switch to a tungsten cathode was a problem associated with the operation of the electron gun at high voltages. The filament heating circuit was always at the beam voltage. When operating at voltages above 10 kV, an occasional 'arc or spark' would burn out the fine wire used in the oxide coated cathode heater. This mechanism depleted the supply of injector stage electron guns (the tungsten wire filament had a diameter of 0.1 mm and was less subject to burnout).

---

† The skimmer typically intercepted less than 0.5% of the transmitted beam from the wings of the focused DC electron beam.

‡ Even after over 50 years of use, the exact method by which oxygen and water vapor poison an oxide coated cathode is not clear. The most accepted process involves the chemical combination of oxygen with the free metal (barium or strontium) on the surface of the cathode. The oxide compound has a much higher work-function than the free metal and the electron emission is thereby reduced.

The electrostatic lens systems following the injector stage (operating voltage of 1.9 kV) was used to focus and accelerate/decelerate the electron beam to the final voltage (100 V to 20 kV). A computer code[†] was written specifically to examine the various design possibilities and to optimize the design before manufacture. The design consisted of an intermediate stage (focusing section) that matched the injection stage output energy (1.9 keV) to the input energy of the output lens stage (uniform lens system). Figure 8 is a schematic diagram of the intermediate and output lens stages of the electron gun assembly. The electron trajectories shown are at the extreme edges of the electrons entering the skimmer aperture.

At the highest beam energies (20 keV), the output energy add lens system had almost 12 kV across it. This stage consisted of five lens elements (creating four sections) and therefore had a maximum voltage of approximately 3 kV between adjacent lens elements (which was the maximum possible without breakdown).

A three element telefocal lens system was used as a base design for the intermediate stage. Using a telefocal lens, the beam focus size and position should vary minimally as the final electron beam energy is varied (i.e., each should ideally be independently adjustable). In the final design, the focus diameter, pencil ray angle, and focus position were only approximately

---

†   See Appendix A for a discussion of this code.

independent of the beam energy[†]. For a measurement with a gas target, this dependence on beam

energy, would be inconvenient, but not impossible, to work with. With a gas target, the overlap

of the incident electron beam (diameter, divergence, ...) and the gas target (diameter, divergence,

density, ...) is a important parameter which must be well characterized throughout the

Electron Trajectories at 2keV Beam Energy
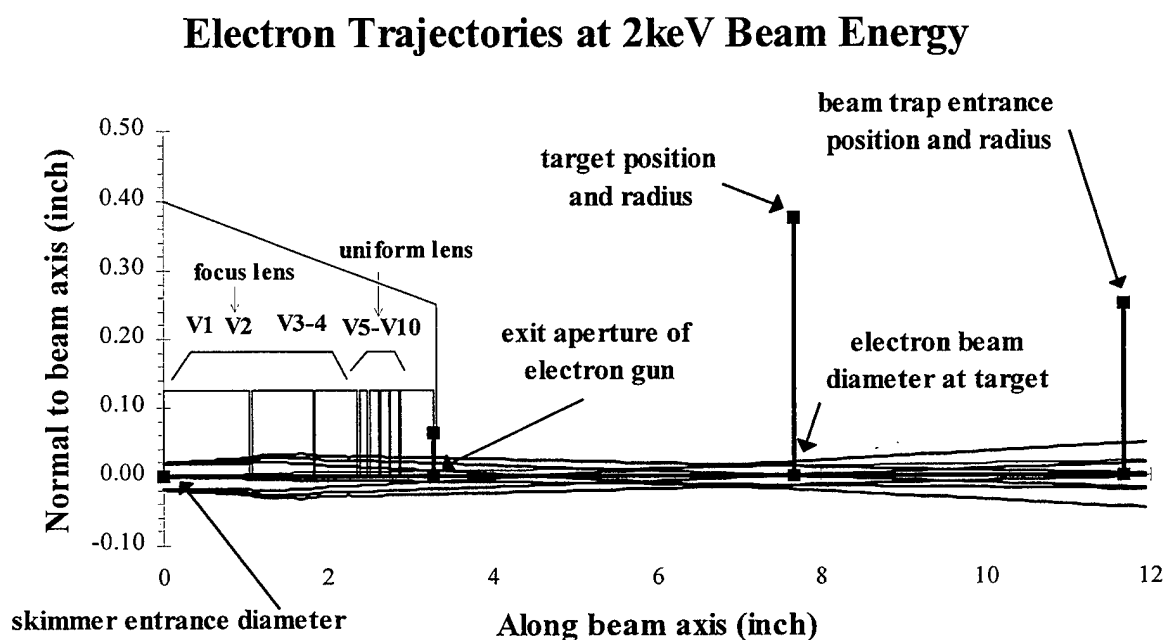
Figure 8: Schematic diagram of the electron lens system.

measurement. Any change in the value of the overlap integral as the beam energy is varied,

would require re-normalization.

The electron gun was mounted inside two concentric aluminum cylinders. The inner

[†]   The voltage range covered during this experiment spanned almost three orders of
magnitude. The design voltage span for a typical telefocal lens system is usually only two orders
of magnitude, so the dependance of the focus parameters on final voltage is not surprising.

cylinder was at the final beam voltage plus 1.9 kV. The outer cylinder was at chamber potential. The inner cylinder was electrically isolated from the outer cylinder using six ceramic spacers to reduce leakage current. The electron gun was mounted ~25 cm above a rotating table. The electron gun beam axis was in the same horizontal plane as the chamber axis. The outer cylinder and support frame completely covered the inner cylinder and any components at voltages other than chamber potential.

As discussed earlier, great care was taken to reduce the magnetic field along the emitted electron's flight path. Components mounted within the vacuum chamber must also be non-magnetic. Two sources of stray magnetic fields were present within the vacuum chamber, both were from the electron gun assembly. The acceleration/deceleration lens system was constructed from components of a 'EV kit'[†]. Since these parts were manufactured from 304 stainless steel, they where slightly magnetic. A second source of magnetic fields inside the chamber was the magnetic field from the wires supplying current to the filament (~0.1 A for the oxide coated cathode and ~2 A for the tungsten cathode). The two wires carrying the heating current were bundled together to reduce local magnetic field projection (any future design will use a coaxial cable which will eliminate the magnetic field produced by the heating current). The magnetic field generated by both were reduced to below 0.1 mG using a single layer of magnetic shielding (0.005" thick Co-netic sheet) which surrounded the electron gun housing. This internal shield was degaussed with a set of coils draped over the shield. The degaussing coils were removed

---

[†]   Obtained from Kimbel Physic Inc., Wilton, NH.

before the chamber was closed.

A packet of electrons was generated by sweeping the DC beam across the skimmer aperture. To do this, a flat top voltage pulse (typically 100 ns wide) was applied to the horizontal deflection plate of the injection section. This pulse was then delayed an additional 17 ns (using coaxial cable) and applied to the vertical plate. This double pulse sequence was necessary to prevent the generation of a second packet at the falling edge of the sweep pulse (i.e., after 100 ns). The sweeping pulse was typically 10 V high with a rise time of 3 ns[†]. The time spacing between packets must be longer than the time required for the slowest electron of interest to reach the detector traveling along a direct path. Since the time of flight of a 0.1 eV electron was ~5 μs, a maximum pulse repetition frequency of 100 kHz was chosen. The above arrangement resulted in a time width of the electron packet of less than 0.6 ns. As such, a DC current of 20 nA would generate a packet that contains ~90 electrons, or an equivalent DC current of 1.4 pA on target.

To retain good energy resolution at low emission energies, the diameter of the beam

---

[†]   A faster rise time pulse generator was available. When used, it would improve the available energy resolution at high emission energies (as seen in a much narrower X-ray flash). This improved energy resolution would be needed in examining energy-loss spectra. However in this experiment, only the total electron yield is of interest and the use of a narrow electron packet reduces the electron current delivered to the target and thereby increases the time required to obtain suitable counting statistics in a data run.

delivered to the target needed to be less than 1 mm[†]. An indirect measurement can be obtained

using the DC beam current intercepted by the three elements of the beam trap. This value was

then projected to the target location. A direct measurement of the diameter of the incident

electron beam at the target position was also made. The procedure is as follows: 1) replace the

target with a metal wire bent in the shape of an inverted "U" 2) rotate the electron gun to its 90°

position (at a right angle to the chamber axis and therefore to any horizontal target displacement)

3) pass the vertical section of the inverted "U" in front of the incident electron beam at the target

location. The incident electron beam profile is directly given by the measured beam trap current

as a function of the wire position. If the wire diameter is greater than the electron beam

diameter, extract the incident beam profile from the width of the falling and rising edges of the

beam trap current. Figure 9 is a typical profile of the electron beam (1.9 keV) measured at the

target location. As the wire diameter was 1.6 mm (and the incident beam diameter was less than

this) the rising and falling edges of the beam trap current are used to calculate the incident beam

profile. The estimated base width is 0.7 mm and the half width is 0.32 mm. The structure in the

target current graph is due to the changing incident angle as the wire moves through the electron

beam.

[†]   The diameter of the beam delivered to the target is a function of the beam energy and the
voltage applied to the focus lens elements (V_2, V_3 and V_4). The measured diameter of the beam
varied from almost 1½ mm (FWHM) at 200 eV beam energy to less than 0.4 mm at 2 keV and
above. A non-optimal adjustment of the focus lens element voltages could produce a diffuse
defocused beam. Therefore, at each incident beam voltage, the diameter of the electron beam
delivered to the target was optimized (i.e., minimized) by adjustment of the voltages applied to
the focus lens elements.

There are two sources of energy spread in the incident electron beam: 1) the energy

spread due to the electron emission process at the cathode (Equation 2.2) and 2) an energy spread

caused by beam electrons hitting lens elements within the electron gun. The first source was

determined by the temperature of the cathode used. The temperature of an oxide coated cathode

Beam Trap Current
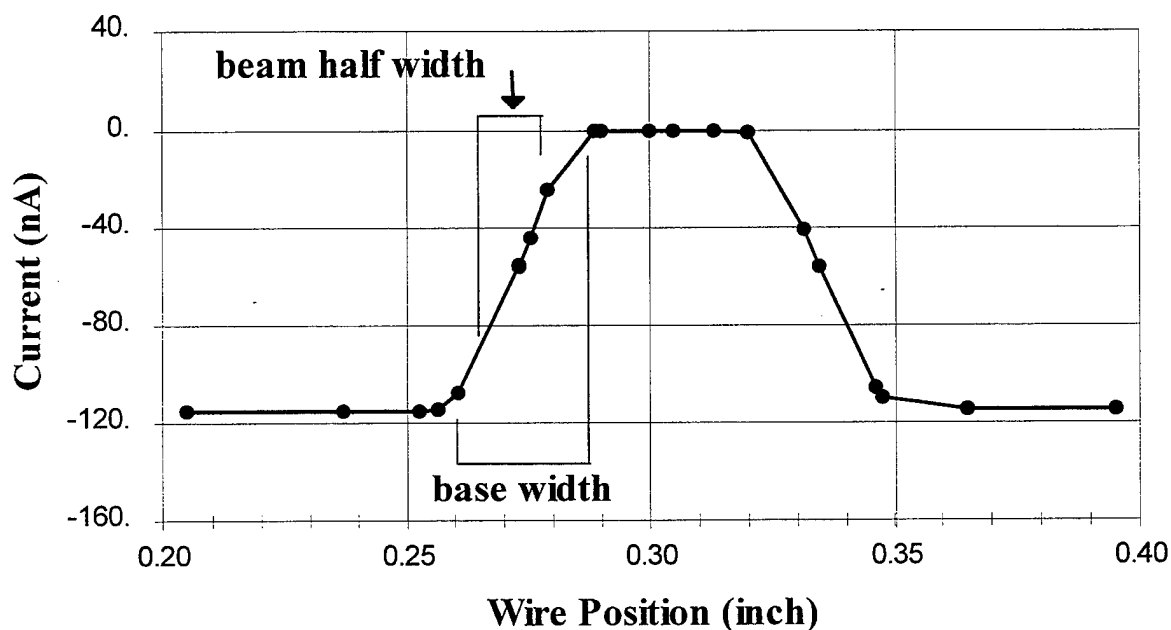
Figure 9: Profile of electron beam measured at target position.

(and therefore the energy width of the emitted electrons) is much less, for the same electron

emission density, than a tungsten cathode. The thermal width of an oxide coated cathode is ~0.1

eV while that of the tungsten cathode is ~0.3 eV.

The second source does not result in simply a 'spreading' in the energy of the incident electron beam, but instead the creation of a second electron beam displaced in energy (possibly by 100's eV) which accompanies the primary energy beam. Within the electron gun, if a primary beam electron intercepts a lens element (e.g., an aperture or deflection plate), secondary electrons will be produced. It is possible for the electron optics that follow this lens element to transport these secondary electrons (a satellite beam) through the electron gun to the target. The number of satellite beams present will be determined by the number of apertures hit and the ability of the following optics to transport the resulting electrons to the target. The standard technique to eliminate this energy spread is to insure that any window (an aperture that determines the beam diameter) is at a voltage that is slightly higher than an immediately following lens element, so any secondary electron produced will not be able to overcome the potential hill between these two elements[†]. In the electron gun discussed here, the diameter defining aperture was the skimmer aperture. The tube lens following the skimmer was 20 V below the skimmer potential. Any secondary electrons generated at the skimmer will not pass the following element and therefore not make it out of the electron gun. The energy of the incident beam at the skimmer location was at 1.9 keV and therefore any focusing effects from this 20 V gradient were negligible.

Electron Detector:

The energy of the emitted electron was calculated from the measured time of individual

---

[†]   Remember, most secondary electrons have emission energies less than 5 eV.

electrons to travel from the target to the detector. Therefore the electron detector needed to be sensitive to individual electrons. Both a spiral electron multiplier (SEM) and a microchannel plate (MCP) pair are capable of detecting single electrons. The SEM (10 mm active area) is a more rugged electron detector and was used in the initial experimental setup and "tweaking" period and some initial measurements, the MCP pair (25 mm active area) was used during the final measurements because of its larger diameter and superior timing resolution. The nominal

Table 2	Electron Detector Parameters		
Parameter	SEM	MCP pair	Unit
Gain	~3x10^9	~10^7	$\#_{out}/\#_{in}$
Time jitter	<0.5	0.03	ns FWHM
Active area	10	25-40	mm diam
Rise time	5	1	ns
Pulse width	20	3	ns FWHM
Maximum input rate	~1	2-5	Mcps
Dark current	<0.5	3-7	cps

properties of these detectors, quoted by the manufacturer (Galileo Electron Optics), are presented in Table 2.

A SEM or MCP can be considered as a very compact electron multiplier; a single electron at the input will be amplified by approximately 10$^{7-9}$ at the output. The amplification process is statistical in nature and therefore the output pulse has a distribution in gain. Figure 10 shows a typical "pulse height distribution" for a MCP pair. This distribution is a measure of the charge contained in the output pulse delivered by a MCP due to a single input electron. The gain

48

(charge in the output pulse or pulse height) is plotted along the abscissa with the frequency of occurrence of this output charge is plotted along the ordinate. The distribution is characterized by a peak which corresponds to the most probable gain of the MCP (~6x10^6) and a valley which corresponds to the onset of dark current noise pulses from the MCP. Figure 10 shows a typical

Pulse Height Distribution
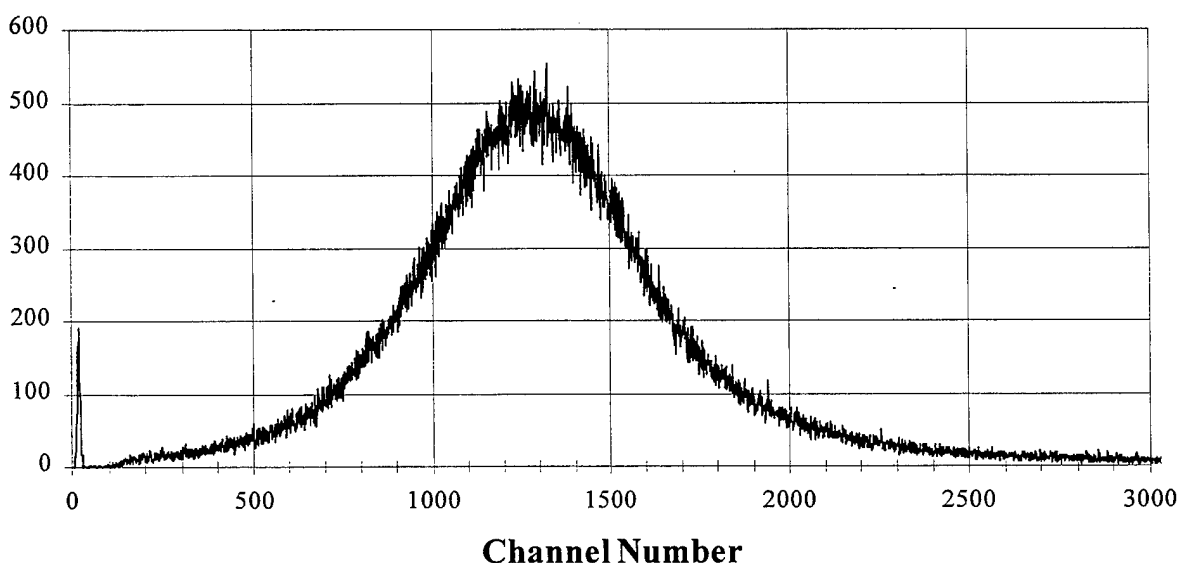
Figure 10: A typical "pulse height distribution" for a MCP pair.

"pulse height distribution" for a MCP pair. The peak position corresponds to a gain of ~6x10^6 (horizontal axis scale is ~0.8 fC/channel). The "peak to width" figure of merit for this MCP pair is 1.7. The discontinuity in the distribution near channel 100 is associated with the discriminator level setting in the following electronics, i.e., any electron event, with a gain of less than ~5x10^5, will be missed by the following electronics.

A gross figure of merit is the ratio of the peak location to the FWHM of the "pulse height distribution (a new MCP will have a large gain and a narrow distribution width, i.e., the figure of merit is >1). As a MCP pair ages, the peak value slowly decreases (as gain falls) and the valley slowly fills up (due to increased darkcurrent noise pulses). The useful life of a MCP pair ends when the noise pulse distribution is larger than the signal pulse distribution.

A key performance parameter for either the SEM or MCP device was the timing jitter of the detector. This directly effects the measured energy resolution of the emitted electron. In the worst case, the timing jitter needs to be less than the time width of the electron package at the target (~0.5 ns). The poor timing jitter (~0.5 ns) and the increase in flight path length uncertainty (~1 mm) due to the shape of the input surface (a concave funnel) increased the electron energy resolution obtainable with a SEM (Equation 2.9 from page 16).

Another important performance parameter for both electron detectors was the output count rate. At the maximum output rate quoted by the manufacturer (~1 Mcps), the gain (ratio of the number of electrons in the output pulse to a single incident electron) decreases dramatically from the gain at low output count rate. Figure 11 shows the same MCP pair (as in Figure 10) at three detector output count rates: a) 30 kcps, b) 60 kcps and c) 100 kcps. The peak position decreases from channel ~1250 to channel ~500 and the "peak to width" figure of merit decreases from ~1.7 to ~1.2 as the output count rate increases. At high signal count rates, a substantial number of electron events will be lost.

The gain decreases because the time required to replace the charge removed from the wall of the detector by a previous pulse was longer than the time to the following pulse. This gain decrease was most pronounced in the output plate of the MCP pair since this plate supplies most of the electron gain in a pulse[†].

The MCP detector assembly was mounted inside the inner cylinder of the Faraday trap. An electron entering the Faraday trap aperture (1.9 cm diameter) drifted an additional 8 cm to the front surface of a grid (4.2 cm diameter). The grid is formed from a tungsten wire mesh, and was coated with graphite to reduce the production of secondary electrons by incident electrons. The grid was at chamber potential and had an measured optical transmission of $93.4 \pm 0.5\%$. The front surface of the MCP (front edge of the cone of the SEM) detector was mounted 1 cm behind the grid and was biased approximately +270 V relative to the grid. The potential difference between the grid and the surface of the front MCP increased the kinetic energy of the incident electron by 270 eV. This energy addition at the end of the flight path was included in the

---

[†]   The gain of a single channel of a MCP is a function of the secondary electron production coefficient at the wall of the channel. The electron gain within a channel is optimized with respect to the channel diameter. An electron emitted from an interior point will drift to the opposite wall of a channel tube, at the same time being accelerated down the channel tube by the axial electric field present in the tube. If the distance down the tube is sufficient to increase the electrons kinetic energy to a value equal to the peak in the secondary electron production process (~150 V), the gain will be a maximum. If the electric field down the tube is reduced (though charge removal from the wall), then the emitted electron will drift to the opposite wall before it has traveled down the tube a distance sufficient to acquire the optimal energy for secondary electron production. This means the charge removed by the previously processed pulse has not been replaced and therefore the gain of the following pulse has been reduced. The replacement charge comes ultimately from the power supply through the bias resistors to the micro-channel plates.

calculation of the final emission energy of the electron[†].

The detection efficiency of an unbiased MCP/SEM was less than 10% for incident

MCP Pulse Height Distribution
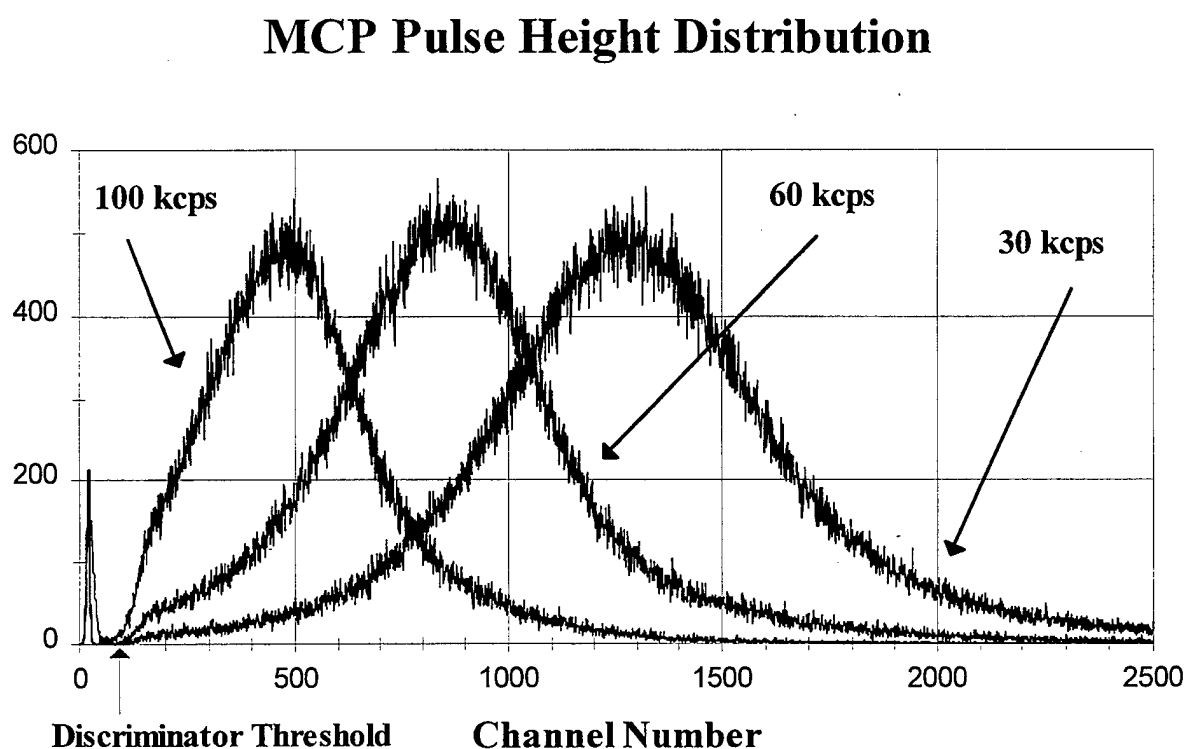
Figure 11: Pulse height distributions for a MCP pair at three detector output count rates.

electrons with kinetic energies less than 5 eV, rises to near 100% at kinetic energies near ~300

eV, and then slowly falls to ~50% near 20 keV. The addition of the bias voltage on the front of

the electron detector added ~300 eV to an incident low energy electron and assured that the low

---

† The calculation assumes a straight line flight path (i.e., no magnetic and electric fields along the path) from the target to the grid followed by a region of uniform acceleration from the grid to the MCP input face. The maximum correction was ~100 ns for low energy electrons.

energy electron would be detected with near full efficiency while only slightly decreasing the detection efficiency of a high energy electron.

The operating voltages needed for the MCP/SEM operation were supplied by a resistor chain mounted behind the MCP pair inside the vacuum chamber. Figure 12 shows the voltage configuration used for the MCP pair (that for the SEM detector is similar). The bias resistor chain was mounted inside the inner shield of the Faraday trap. Two high-voltage capacitors, one used as a power supply filter capacitor, the second as a blocking capacitor in the signal line, were also mounted inside the inner shield. The high-voltage resistor chain had a total resistance of 29.7 M$\Omega^\dagger$. During pulse mode co figuration, all three shields were connected. Typically, the overall voltage applied to the MCP was 2,700 V: 950 V across each MCP, 270 V from the exit MCP surface to the anode, and across the filter resistor. The final 270 V was between the grid and the input surface of the first MCP.

To retain the fast rise time of the output pulse (necessary for good timing resolution), coaxial cable was used to transmit the output pulse to the vacuum feedthrough and from the vacuum feedthrough to the following electronics. Because of potential leakage paths from the inner cylinder of the Faraday trap to ground, the number of electrical connections brought out of

---

† Initially a smaller value of 4.4 MΩ was used in the resistor chain, but under voltage would dissipate over 1.6 W within the vacuum chamber. The heating and subsequent outgassing of the resistor chain increased the noise count rate in the detector by over two orders of magnitude. A resistor chain with 29.7 MΩ total resistance dissipates just over 0.2 W within the vacuum chamber (~1/8 of the original value).

53

the inner cylinder was limited to four: 1) the anode signal line, 2) the high-voltage source for the

Microchannel Detector
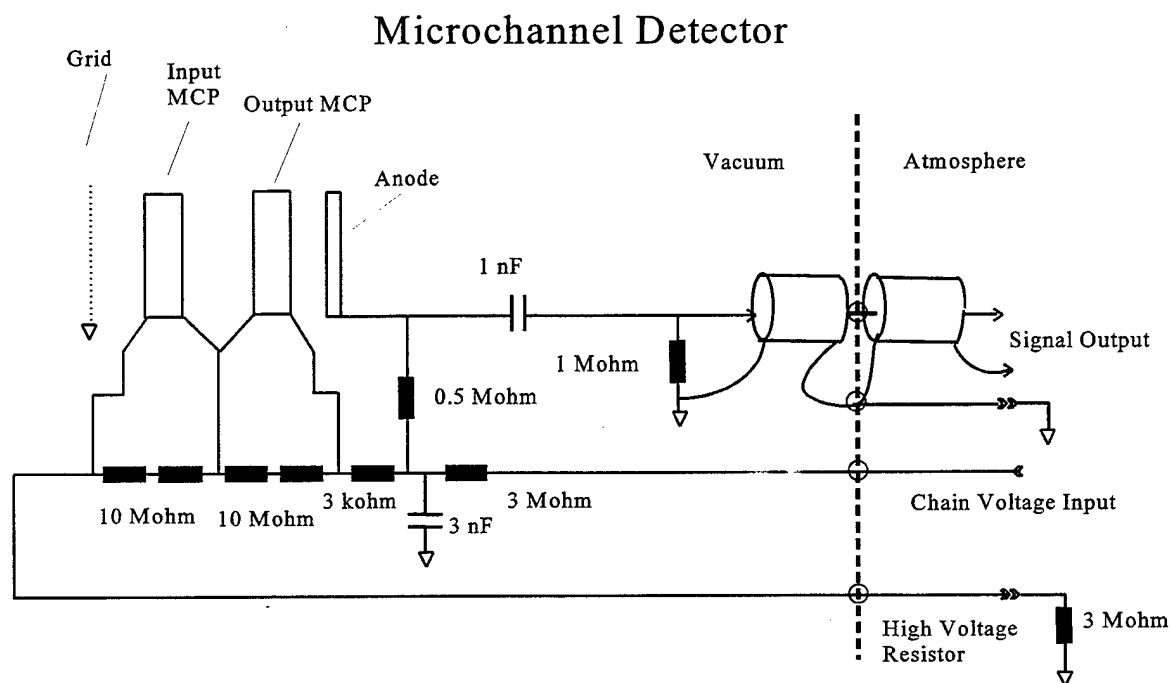
Figure 12: Voltage configuration of the MCP pair.

resistor chain, 3) the connection to the input surface of the first MCP (or SEM) and 4) the inner

cylinder, i.e., the grid connection. The input bias for the front surface of the detector was

established using a single resistor, mounted outside of the vacuum chamber. This resistor was

connected between the front surface lead (3) and the power supply return (4).

Faraday Trap:

The Faraday trap was constructed using three concentric cylinders, each electrically

54

isolated from the others. Figure 13 is a schematic drawing of the Faraday trap. The overall

length is 30 cm, the inner diameter of the inner cylinder is 9.5 cm, the outer diameter of the outer

cylinder is 12.4 cm. The Faraday trap is mounted on a ISO-160 flange which in turn is mounted

on the vacuum port on the chamber door. The volume occupied by the detector is pumped
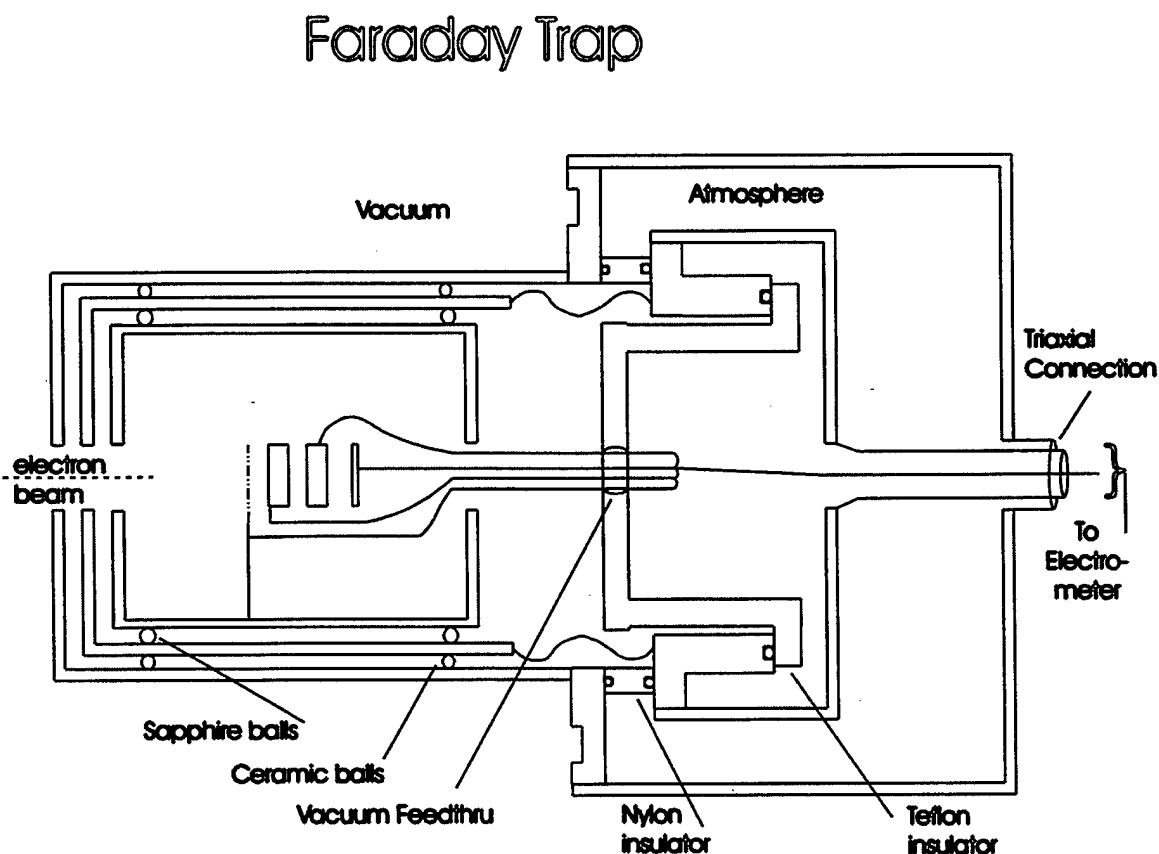
Faraday Trap

Figure 13: Schematic drawing of the Faraday trap.

through the input aperture (which will vary depending on the required acceptance solid angle of

the detector) and through pumping holes around the back side of the chamber flange. The input

grid on the MCP detector is 14 cm behind the input aperture. The triaxial geometry of the Faraday trap cylinders is continued outside of the vacuum chamber up to the electrometer. During "Current Mode" configuration, the four signal lines from the inside of the inner cylinder are shorted to the inner cylinder (as shown) and constitutes the center conductor of the triaxial cable connection to the electrometer. During "Pulse Mode" configuration, the four signal lines are connected to the resistor chain voltage source, the bias resistor for the input surface on the MCP pair and the coaxial cable for the pulse output.

This triple shielding was needed to reduce the noise and leakage currents during the measurement of the absolute detection efficiency of the MCP/SEM detector. The leakage resistance between the inner cylinder and the middle cylinder was 30 TΩ. Sapphire spheres were used to mount the inner shield inside the middle cylinder, with virgin PTFE[†] as the vacuum-atmosphere insulator. The middle cylinder to outer cylinder leakage resistance was 5 TΩ (ceramic spheres were used to mount the middle cylinder inside the outer cylinder, with nylon as the vacuum-atmosphere insulator). The outer cylinder was electrically connected to the chamber. The three cylinders established a triaxial configuration that was continued up to the triaxial input connector of the electrometer (Keithley 617).

Beam Trap:

The electron current incident on the target (I_{in}) generated the secondary electrons

---

†   Virgin PTFE (polytetrafluoroethylene) has a higher volume resistivity and surface resistance than reconstituted PTFE.

measured by the MCP/SEM detector. This incident current cannot be measured directly. Any direct measurement of the target current (I_{tr}) only measures the difference between the incident current (I_{in}) and the total secondary and backscattered emission current ($\sigma * I_{in}$). Since the target was removable and the electron gun was limited to rotation in a horizonal plane, a beam trap was mounted coaxial with the incident electron beam directly across from the electron gun. The beam trap moved with the electron gun as it was rotated about the target. To monitor the electron current incident on the target (I_{in}), the target was translated out of the electron beam and the incident electron beam measured by the beam trap (I_{tp}).

To assure that the measured trap current (I_{tp}) equals the incident beam current (I_{in}), the beam trap must be "deep," i.e., have unit efficiency over the entire incident electron energy range from 100 eV to 20 keV. Here "deep" refers to the ratio of the entrance diameter to the length of the trap, i.e., the aspect ratio of the trap. If the aspect ratio is small, the probability that an electron hitting the bottom of the trap will generate secondary (or backscattered) electrons that can escape through the entrance is small. Figure 14 is a schematic drawing of the beam trap. The overall length is 30 cm, the diameter of the input aperture is 12.7 mm. The diameter of the inner cylinder is 22. mm, while the diameter of the pin hole at the base of the inner cylinder is 1.27 mm., or an aspect ratio of less than 1:20. The geometric probability of an incident electron escaping the trap was therefore ~1:3,000[†]. This probability can be decreased further by first

---

[†]   This assumes that both the secondary and backscattered electrons are emitted isotropically. Under this assumption, the ratio of the solid angle of the entrance aperture as seen from the bottom of the trap to the forward hemisphere (2π sr) determines the probability of escape ($1/4$ $\pi(1.27)^2/(25^2)/2\pi \approx 1/3000$).
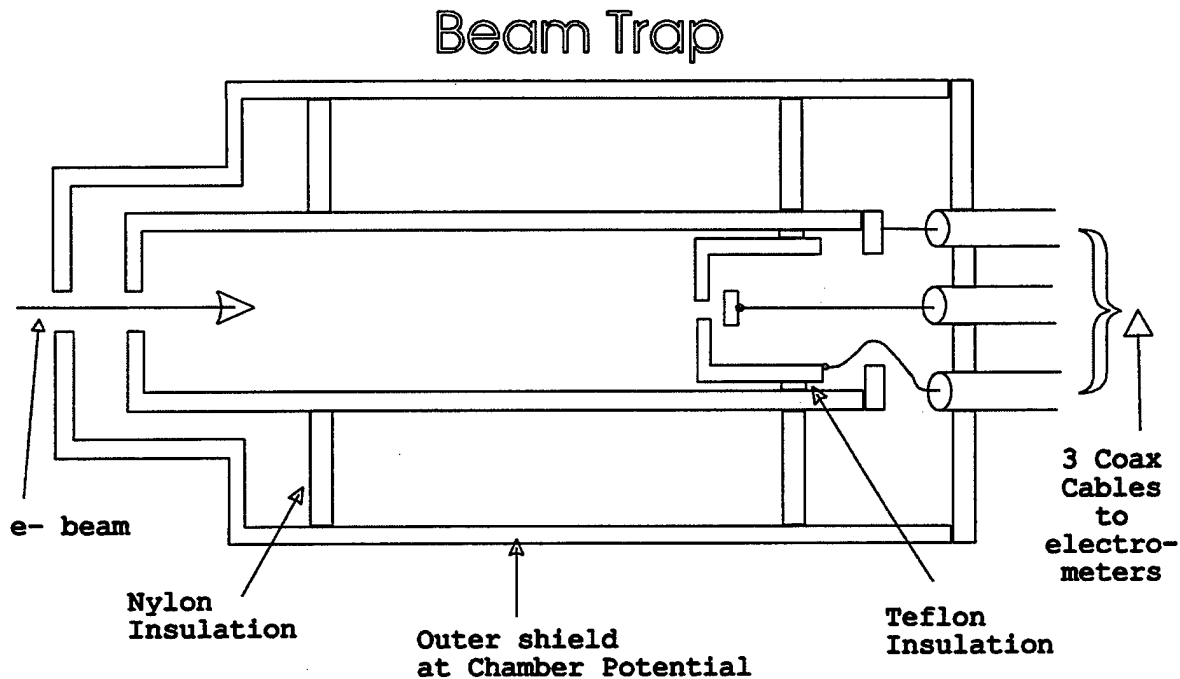
Beam Trap

Figure 14: Diagram of the incident beam trap.

coating the interior surfaces with graphite (which had a low secondary electron production

coefficient) and then biasing the bottom of the beam trap +20 V relative to the exit aperture.

With this bias, any secondary electron with emission energy less than 20 eV cannot exit the beam

trap. The 'unit' efficiency for the beam trap was checked using this bias on the bottom element,

for the measurements reported here, $I_{in} = I_{tp}$.

The interior of the beam trap contains three electrodes. The first was a tube (2 cm

internal diameter) electrically isolated from the surrounding shield (at chamber potential). This

tube had an entrance aperture slightly larger than the beam trap entrance aperture. The tube

extends the full 25 cm to the base of the trap. The current to this electrode was designated I_s ('s' for shield). The base of the beam trap was electrically isolated from the tube. Current to this electrode was designated I_m ('m' for middle). This electrode had a pin hole in it (1.27 mm diameter). Behind this hole was the third electrode, electrically isolated from the other electrodes. This electrode measured the current passing the hole; this current was designated I_c ('c' for center). The sum of all three currents gives a measurement of the total current to the trap (I_{tp}).

The ratio of the current passing to the third element (I_c) to the total incident current (I_{tp}) can be used as an indirect, on-line measurement of the size of the incident electron beam. Two assumption are made, a) the incident electron beam has a gaussian shape and b) I_c measures that fraction of the incident beam current that lies within the pin hole diameter with unit efficiency (i.e., scattering by the hole is ignored)

$$\Delta W = 2*\sqrt{(2*\ln(2))}* R / \sqrt{(2 * \ln\{1/[1-I_c/I_{tp}]\})} \tag{3.2}$$

where ΔW is the FWHM of the incident electron beam, R is the radius of the pin hole in the base. These measurements agree with the direct measurement described earlier (made when the target was replaced with a metal wire in the shape of a "U").

High-Voltage Cage:

An extensive set of bias voltages were needed for the electron gun operation. Over 30 separate signal voltages were passed into the vacuum chamber. Figure 15 is a schematic drawing

of the electron gun and associated operating voltages[†]. The overall length is 30 cm, the diameter of the output aperture is 3.2 mm. The diameter of the inner cylinder (which is at beam energy) is 25.4 mm, while the diameter of the outer cylinder (which is at chamber potential) is 51 mm. Also shown are the signal voltages that pass into the vacuum system. The majority of these
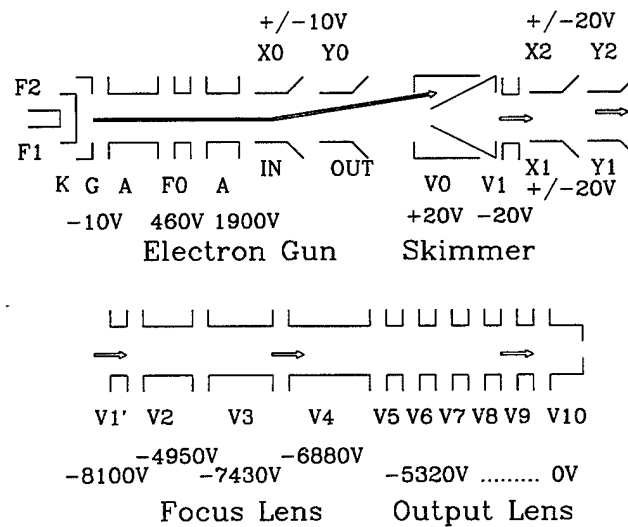
Figure 15: Schematic drawing of the electron gun.

voltages were needed to control the operation of the injection electron gun. Consequently, these

---

† The voltages on the electron gun elements are relative to the cathode, those on the skimmer and deflection plates are relative to the anode and those on the focus and output lens elements are relative to the chamber. The values shown are for an output beam energy of 10 keV.

voltages were at levels near the electron beam voltage (which reached values as large as -20 kV).
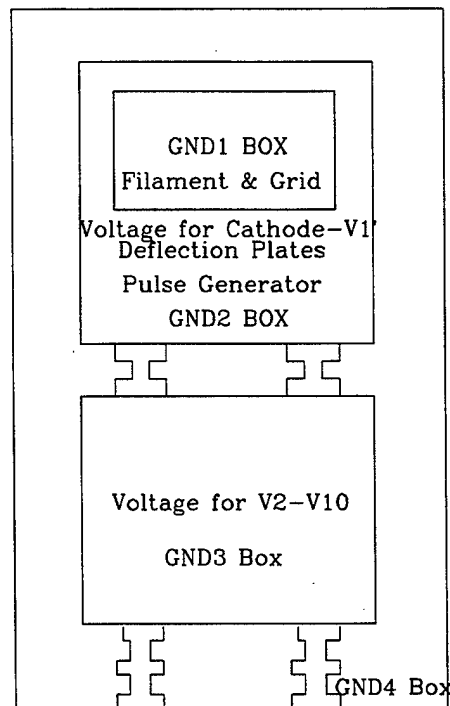
Figure 16: Simplified schematic of the overall voltage distribution system showing the four 'grounds:' GND_1, GND_2, GND_3 and GND_4

The remaining voltages were near the acceleration/deceleration electron lens voltage (which reached only the -10 kV level). All voltages required for the lens element systems could be obtained using a simple resistor divider chain (i.e., no current source was needed). The power supplies needed for the various resistor chains were housed in three shielded metal boxes, which were, in turn, housed in a shielded, high-voltage cage. All voltage and power adjustments were

made using an insulated plastic rod.

To simplify visualization of the distribution, each of the metal boxes can be associated with a different 'ground,' (depending on the beam energy required, one 'ground' could be as much as 10 kV below an adjacent 'ground,' with both of these being an additional 10 kV below earth 'ground'). All power supplies, voltage sources and the pulse generator required for the injection electron gun were located in the first isolation box (referenced as GND_1). All power supplies, voltage sources and the pulse generator required for the deflection and intermediate stage were located in the second isolation box (referenced as GND_2). All power supplies and voltage sources required for the final acceleration/deceleration lens system were located in the third isolation box (referenced as GND_3). The chamber was at earth potential (referenced as GND_4). Figure 16 shows a simplified schematic of the voltage distribution system. The AC power requirements for the three 'grounds' were supplied using three isolation transformers (25 kVDC isolation).

The cathode or filament of the electron gun was connected directly to GND_1. Figure 17 shows a schematic of the signals generated in the GND_1 cage. In operation, GND_1 was placed at the final beam voltage, e.g., at beam energy of 10 keV, GND_1 was at -10 kV relative to GND_4 (chamber potential). The final beam voltage was established using an ultra-stable, low-noise, high-voltage power supply referenced to GND_4. GND_1 was the only stage that had power requirements (5 W for the electron gun filament heater) that extended into the vacuum chamber. The voltages for this stage were supplied by two low-voltage power supplies: one for the filament voltages, F_1 and F_2 (5 V at 3 A), and a second for the 'grid DC bias,' G_0 (0 to -100 V). A

low-voltage pulse generator (+10 V with a time pulse width of 100 ns) was capacitively coupled

to G_0 and supplied the 'grid enable' pulse. The various voltage and current levels were monitored

using a battery-operated voltmeter which used a resistor divider or a shunt resistor to sample the
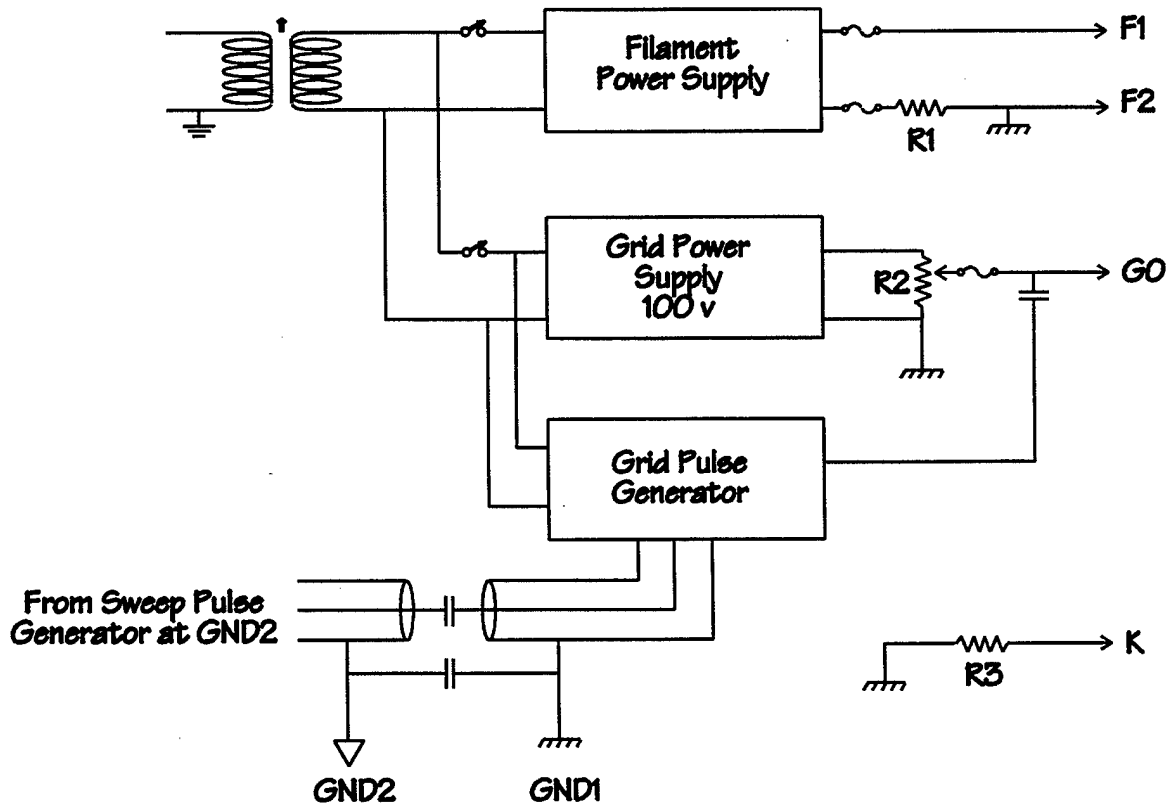
Figure 17: Schematic of the signals generated in the GND_1 cage.

required signals. R_1 (0.01 Ω) was used to monitored the filament current, R_3 (1 kΩ) to

monitored the filament emission current, R_2 (100 kΩ) is a 10-turn potentiometer with which the

DC voltage level applied to G_0 is adjusted. The capacitors C (3 nF) were used to couple the

pulse from the sweep pulse generator into the grid enable pulse generator and the grid enable

pulse onto the grid. Four 'wires' leave the first isolation box (GND_1) for transfer into the vacuum chamber: F_1, F_2 (filament voltage), G_0 (grid voltage) and K (cathode potential).

The anode (A) of the injection electron gun was connected directly to GND_2. Figure 18 shows a schematic of the signals generated in the GND_2 cage. The working voltage of the injection electron gun was 1.9 kV, and therefore GND_2 was always at +1.9 kV above GND_1. The voltage requirements for this stage were supplied by two low voltage power supplies: one for the working voltage for the injection stage (-1.9 kV), and a second for the resistor chains for each set of deflection plates and the bias voltages for the skimmer collector (V_1)[†]. The focus voltage (F_0) required by the injection stage was obtained using a resistor divider chain between GND_1 and GND_2. A pulse generator, which supplied the sweep pulse to one side of the injection stage deflection plates (Out), was also located in the GND_2 box. The trigger output pulse from sweep pulse generator was capacitively coupled to the 'grid enable' pulse generator at GND_1. The various voltage levels were monitored using a battery-operated voltmeter and resistor dividers to sample the required signal level. R_4 (451 kΩ), R_5 (396 kΩ) and R_6 (903 kΩ) are a resistor chain used to establish the voltage applied to the einzel lens (F_0) on the Textronix electron gun. The 10-turn potentiometers $(R_7 - R_{16})$ were used to supply the bias voltages to various electron-optical lens elements. The currents to the skimmer (V_0) and skimmer collector (V_1) were monitored

---

[†]   A very fast pulse generator (0.5 ns rise time at +100 V) was to be mounted inside the vacuum chamber physically below the electron gun. The power for this pulse generator was supplied with a third power supply. The use of this fast pulse generator was included in the original design since it was not clear that the rise time of the sweep pulse generated in the high voltage cage could be retained at the deflection plates inside the vacuum chamber.

using a battery operated null meter shunted with resistors R_{17} (10 kΩ) and R_{18} (100 kΩ). Twelve

'wires' leave the second isolation box (GND$_2$) for transfer into the vacuum chamber: V_0, V_1
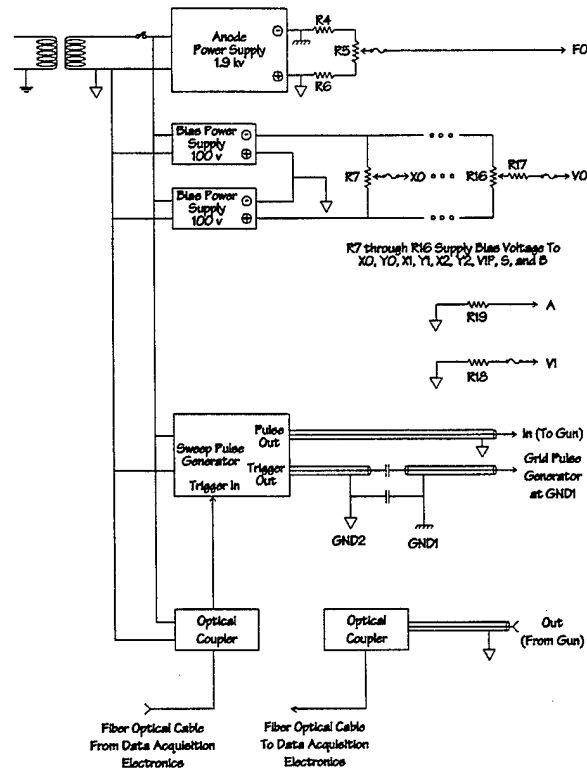
Figure 18: Schematic of the signals generated in the GND$_2$ cage.

(skimmer and skimmer collector); deflection plate biases: X_0 and Y_0 (on the injection gun) X_1,

Y_1, X_2 and Y_2 (located in front of the acceleration/deceleration lens); two coaxial cables (Out and

In) for the sweep pulse to and from the injection deflections plates; F_0 (focus voltage for the

injection electron gun); and A (anode potential for the injection electron gun).

The final isolation box, GND$_3$, was float at ±3 kV relative to GND$_2$. Figure 19 shows a

schematic of the signals generated in the GND_3 cage. This stage is essentially four resistor

divider chains (each at 6 kV) which supply appropriate voltages to the acceleration/deceleration

lens system. Resistors R_A (14 X 301 kΩ), R_B (9 X 150 kΩ), R_C (11 X 39 kΩ) and 10-turn

potentiometer (100 kΩ) supply the voltages to lens elements V_2 - V_4. Depending on the resistor

settings, the output resistance for these voltage source can be as large as 3 MΩ. Resistors R_E (14

X 150 kΩ), R_F (11 X 39 kΩ) and R_G (5 X 20 MΩ) supply the voltages to lens elements V_5 - V_9.

The source resistance for the V_5 voltage supply is 1.3 MΩ. The 6 kV voltage difference is
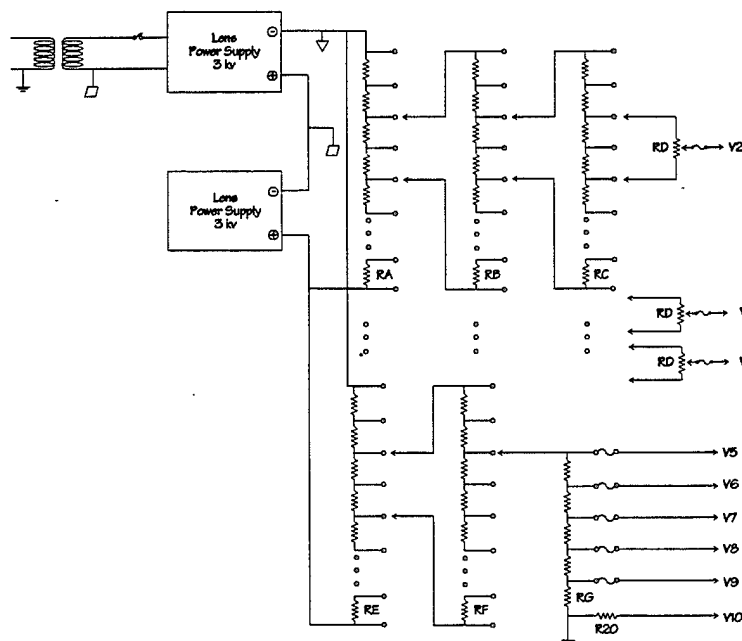
Figure 19: Schematic of the signals generated in the GND_3 cage.

supplied using two 3 kV power supplies referenced to GND_3. The acceleration/deceleration lens

system consists of a 'focus' lens constructed from three (tube) lens elements followed by a

'uniform' lens constructed from 5 (aperture) elements. The 'focus' lens elements were connected

to three of the above resistor divider chains. The first element of the 'uniform' lens was connected to the last resistor divider chain. The last aperture element was connected to chamber potential (GND_4). This 'uniform' lens system was highly stressed with respect to voltage breakdown (at a beam energy of 20 keV, the voltage across these five aperture elements could be as large as 12 kV). The various voltages were monitored using a simple battery-operated voltmeter and resistor dividers. Nine 'wires' leave the third isolation box (GND_3) for transfer into the vacuum chamber: V_2, V_3 and V_4 (focus lens elements) and V_5, V_6, V_7, V_8, V_9 and V_{10} (uniform lens system).

High-Voltage Feedthrough and Cabling:

The 25 wires from the high-voltage cage where transported to the vacuum chamber using unshielded graded dialectic insulated wire (without shield). The transfer of the DC voltages into the vacuum chamber was made using three glass vacuum feedthroughs. Each vacuum feedthrough had a 20 pin connector on the end of a 6" length of glass tubing. Since adjacent pins could hold-off only ~3 kV, the 25 wires were distributed among the pins so that only a maximum of ~2 kV was between adjacent pins. When it was necessary to connect wires with a larger potential difference, the pin between the two wires was skipped. The skipped pin's potential was not allowed to float, but was set to a value half way between the other two adjacent pins (using a simple resistor voltage divider). Essentially only half of the pins were available from each feedthrough. The two coaxial signal cables passed into the vacuum chamber using a fourth glass vacuum feedthrough to keep signal cable environment equal to 50 Ω (necessary to retain the fast risetime of the sweep pulse).

The high-voltage cabling within the vacuum chamber used the same unshielded graded dialectic insulated wire as outside. The connections were made using non-magnetic nylon and copper press-fit junctions. The coaxial cable within the vacuum chamber was RG58U/C placed inside of two Teflon extruded tubes (0.04" wall thickness). The maximum standoff voltage for this combination was calculated at well over 20 kV.

The following section discusses the 'numbers' that need to be recorded during a secondary electron emission spectrum measurement. The 'size' of the measured parameter and the required resolution in 'real' time and 'flight' time are examined.

Section 4: Measurement Parameters

This section discusses limitation on data signal rates and the measurement parameters recorded during a secondary and backscatter electron yield experiment. The section divides the electronics into two systems: that needed to acquire the machine signals and that needed to process the machine signals to generate the final TOF spectra.

<u>Signal</u> <u>Rate</u> <u>Considerations:</u>

During normal operation, the detector output pulse count rate was kept less than 5 kcps. This restriction on the output count rate was imposed because of three error sources that develop at high output count rates: 1) the distinction between spectrum of 'all' and 'first' arrivals, 2) gain shifts in the electron detector, and 3) limitations in the data acquisition computer (lock-up and dead-time corrections).

The time of flight spectrum measured during the experiment was a spectrum of first arrivals, not a spectrum of all arrivals. The distinction develops because of the finite time (8 μs) required by the data acquisition electronics to process a single event. Any electron that follows an initial electron (within the 8 μs window) will be missed. The measured spectrum therefore would be distorted since a larger number of slow electron events will be missed compared with fast electron events. Under certain assumptions (related to possibility of structure in the final spectra), the spectrum of all arrivals can be re-generated from the measured spectrum of first arrivals. Such an unfolding procedure was not done for the data presented here. Instead, if the

69

input count rate was kept less than 1% of the sweep pulse repetition rate, the measured spectrum will be that of 'all' arrivals (i.e., will not be distorted due to 'missed' events). Appendix B contains a discussion of missed event statistics and shows that at a 1 kcps data rate, only 0.5% (i.e., 5 following electrons per second) will be missed.

The second reason for keeping the signal count rate below 5 kcps was that at count rates above 50 kcps, the gain of the electron detector will decrease (see the discussion of the SEM/MCP detector in Section 3). At some point in the following electronics, a discriminator with a <u>fixed</u> threshold is used to select events. Those events with low gain are missed due to the pulse height falling below the discriminator threshold level[†].

The third reason for keeping the signal count rate below 5 kcps was that, although only 8 μs was required to process an event, the time required to transfer a block of events stored in RAM to the hard disk was very long (on the order of many tens of milliseconds). A disk write occurred whenever the block was full (1024 events) or 10 s had passed. The data acquisition electronics was 'dead' during this write time. Any detected electron event that occurred during this transfer 'dead time' was lost. The system 'dead-time' and 'live-time' was measured by the data acquisition electronics (by counting a reference 10 MHZ clock). The data analysis program

---

[†]   The discriminator threshold level was set to a value which is as low as possible, subject to being high enough to remove background noise events generated within the electron detector itself. Another noise pulse source was sometimes present. It was traced to the operation of the vacuum pump on the main chamber (thought to be due to dirty brushes on the motor). When present, this noise source could inject background count rates of up to 100 cps into the start pulse electronics.

applied the dead-time correction to the target current (I_{tr}) and trap current (I_{tp}) measurements. During beam off condition, the system was typically dead for 4% of the time, while during beam on condition (2 kcps), the system was dead for as much as 15% of the time.

A final reason for keeping the data rate low, was that at very high data rates, the data acquisition program would lock-up and the entire data run would be lost (a problem with the data acquisition software, SDIDAS; competing interrupt flags "confused" the CPU).

Acquisition Electronics:

The primary machine generated signals were:

- Detector signal: End

- Sweep pulse signal: Begin

- Beam trap current signal: I_{tp}

- Target current signal: I_{tr}

The interfacing of these signals with the data acquisition system (located ~20' from the main vacuum chamber) is discussed below. Figure 20 is a schematic of the electronics used to generate the 'End' and 'Begin' signals needed by the CAMAC data acquisition system.

Detector Signal: The 'End' signal comes from the MCP detector. The output pulse from the MCP pair is amplified (x10) and the time pickoff was generated with a constant fraction discriminator (minimal timing jitter from pulse height variation). The 'End' digital pulse signal (NIM-negative) was used to generate the 'Start' signal for the TOF spectrum measurement.

71

Sweep Pulse Generation:

The 'Begin' signal comes from the sweep pulse used to sweep the DC electron beam

PS 6950

Detector

1 nF

X10

Amplifier
0-500 MHz

To "END"
Circuit

Tek FG502

Function
Generator
100kHz

Jaycor 2400

Fiber Optic
Coupler to
HV Cage

GND(4) GND(2)

HP 214B

Pulse Generator
+10V, 100ns

Trigger   Pulse
Input   Out

Electron Gun
Deflection
Plates

X   Y

17 ns Delay Cable

HP 1412 HP 2414

Fiber Optic
Coupler to
Earth

GND(2) GND(4)

TC 455

Constant
Fraction
Discriminator

To "BEGIN"
Circuit

Figure 20: Schematic of the electronics used to generate the 'Begin' and 'End' signals.

across the "skimmer" aperture (Hewlett Packard 214B, ±50 V, 3 ns risetime). The 'Begin' digital

72

pulse signal (NIM-negative) was used to generate the 'Stop' signal for the TOF spectrum measurement.

The maximum sweep frequency was determined by the flight time required for the lowest energy electron to reach the detector (a 0.1 eV electron required a flight time of 5.1 μs). The sweep frequency was usually set to 100 kHz, as the longest usable flight time was 6 μs. The sweep frequency signal was transmitted to the high voltage cage, GND_2 (-20 kV relative to earth ground, GND_4) using a fiber-optic coupler. The recovered electrical signal was used to trigger the sweep pulse generator.

Two output signals from the sweep pulse generator were used. The 'trigger output' signal was coupled (using capacitors in both the source and return signal paths) to the G_0 pulse generator at GND_1 (-1.9 kV relative to GND_2). The G_0 pulse generator was advanced or delayed relative to the sweep pulse generator using the delay/advance control on the sweep pulse generator. The pulse height of the G_0 pulse was set at +10 V (the maximum possible) with a pulse width of ~100 ns for all of the measurements reported here. This pulse was used to reduce the background noise current in the detector when the DC electron beam was positioned at the edge of the skimmer.

The second signal output from the sweep pulse generator was the positive output pulse. This signal was delivered to the electron gun 'X' deflection plate in the main vacuum chamber. Approximately ~10' of RG58A/U coaxial cable was used inside of the vacuum chamber. The

sacrifice in bandwidth (pulse slew rate) due to the use of this cable was a tradeoff made to obtain

needed cable flexibility inside the vacuum chamber. The twin coaxial cables within the vacuum

chamber needed to bend through 180° as the electron gun was rotated about the target (RG233/U

cable has a much wider bandwidth, but was too stiff). After the connection to the 'X' deflection

plate, the sweep pulse was delayed an additional 17 ns (using ~3' of RG233/U) and applied to the

'Y' deflection plate. The pulse was then returned to the high voltage cage using another ~10'

section of RG58A/U cable. At the high voltage cage, the sweep pulse was transmitted to earth

ground (GND_4) using a fiber-optic coupler[†]. The time pickoff from the recovered electrical

signal was generated using a constant fraction discriminator and delivered to the data acquisition

system (as the BEGIN signal). This digital pulse signal (NIM-negative) was used to generate the

'Stop' signal for the TOF spectrum measurement.

Current Measurements:

Figure 21 is a schematic of the electronics used to generate the 'Target' and 'Beam Trap'

current signals needed by the CAMAC data acquisition system. These two signals are further

---

[†]   The fiber-optic cable from the sweep frequency generator to the high voltage cage was
over 200' long. The cable length, coupled with a transmitter/receiver (Jaycor Model 2400) rise
time of only ~20 ns, resulted in a time jitter in the final sweep pulse relative to the sweep pulse
generator of 3 ns. The fiber-optic cable on the return leg from the high voltage cage to earth
ground was only 6' long. The transmitter/receiver (here a Hewlett Packard HFBR-2414/1414
series) had a rise time of <1 ns with a measured jitter time of ~30 ps FWHM. As the stop signal
was obtained from the pulse used to sweep the DC beam across the skimmer, only the 30 ps time
jitter contributed to the time uncertainty in the TOF measurement.

processed by the CAMAC data acquisition system. The nominal noise current in the target

current measurement (I_{tr}) was ~0.05 pA RMS, while that in the beam trap current measurement
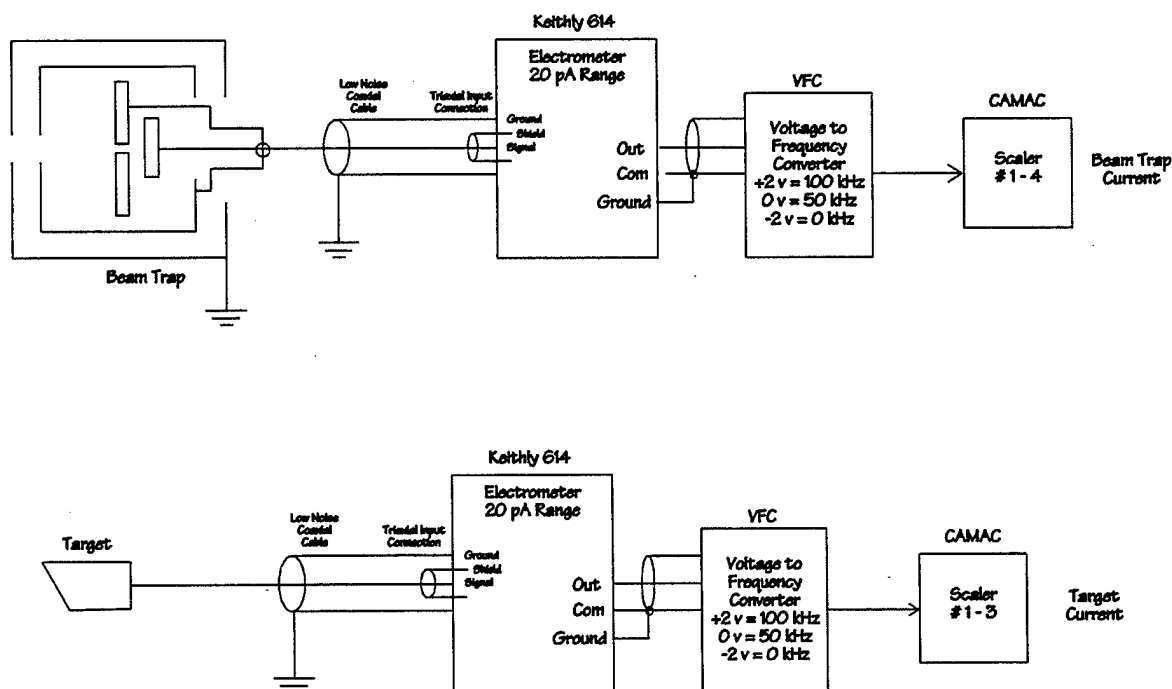
Figure 21: Schematic of the electronics used to generate the target and beam trap signals

(I_{tp}) was ~0.2 pA RMS. The difference was thought to be due to the lack of low noise cable from

the beam trap to the vacuum feedthrough (interchanging the electrometers resulted in the same

noise values). The latter noise, although large, was not considered significant since the incident

beam current was in the 2-4 pA range (S/N ~20:1).

The measured target current (I_{tr}) is related to the incident beam current (I_{in}) through

$I_{tr}=I_{in}*(1-\sigma)$, where σ is the sum of the secondary (δ) and backscatter (η) electron yield

75

coefficients. The measured target current was negative whenever the total electron production coefficient was less than unity, and positive whenever the total electron production coefficient was greater than unity. The target current can therefore be much smaller than the beam current (equal to zero when $\sigma = 1$). Both the target current (I_{tr}) and the beam current (I_{tp}) were monitored continuously during an emission spectrum measurement.

Figure 22 shows a typical plot of the measured target, measured beam trap and calculated
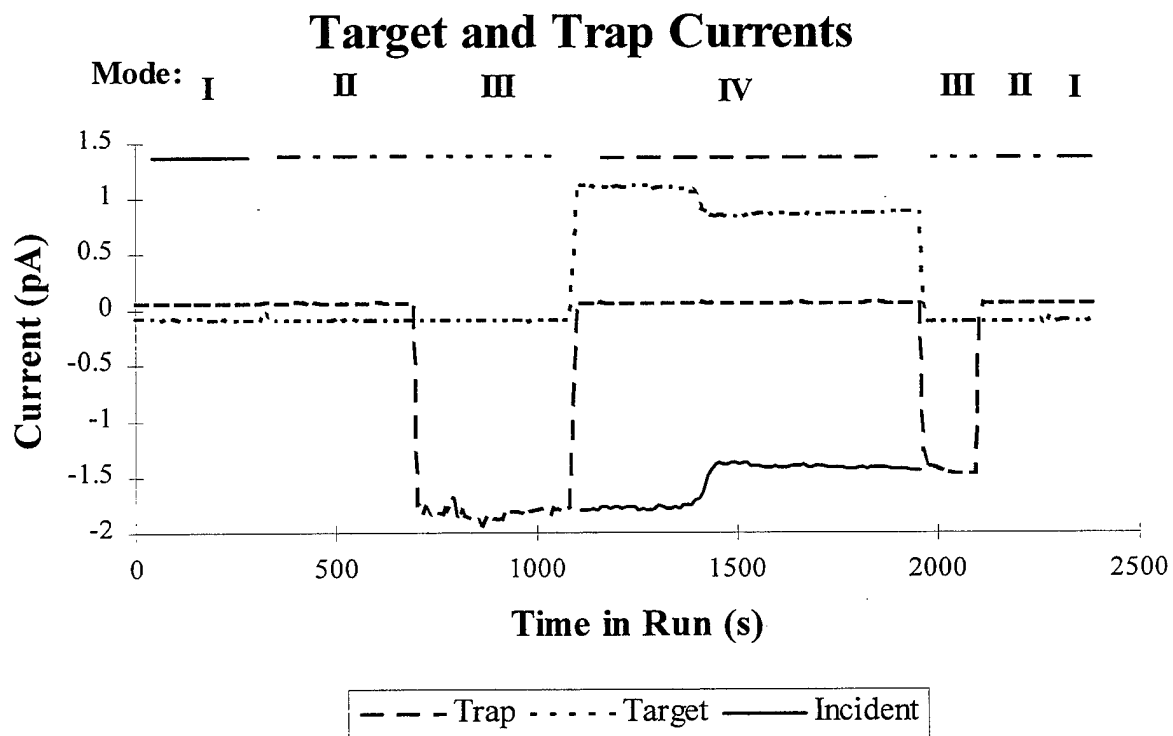
Figure 22: Plot of measured beam, measured target and calculated incident current.

incident beam currents. The four operational modes during the measurement are indicated on the diagram. During modes I and II, machine background currents (I_{tr0} and I_{tp0}) are measured.

76

During mode III, the incident pulsed beam (I_{in}) is measured directly by the beam trap (I_{tp}).

During mode IV, the target current (I_{tr}) is measured directly. The measured target current is related to the incident beam current (I_{in}) through the secondary and backscatter emission coefficient σ:

$$I_{tr} \quad = \quad I_{in}*(1 - σ).$$

In Figure 22, the curve marked 'Incident' is calculated from the measured target current corrected by the factor "1 - σ". The value used for σ comes from matching the measured trap current (I_{tr}) with the calculated trap current (I_{in}) at the change from mode III to mode IV. The data run shown here is atypical as the sharp decrease in the incident beam current that occurred near run time 1400 s is not normally seen. This data run was included to show that the measured trap and target currents can be used to determined the incident beam current during the emission measurement. The integral of the calculated target current over the length of time in mode IV is the total charge delivered to the target and is used to normalize the measured yield spectra.

Target Current Measurements:

The connection to the target was made using low-noise coaxial cable (within the vacuum chamber, the exterior insulator on the coaxial cable was removed to reduce outgassing from the cable and to eliminate charging of the outer shield by stray electrons). The current to the target was measured with a Keithley 614 digital electrometer (used on the 20 pA range with a manufacturer quoted 10 fA resolution). The ±2 V analog output signal was further amplified and

then digitized using a voltage-to-frequency converter (VFC)[†]. The current range of ±20 pA was thereby mapped onto an output frequency range 0-100 kHz with 0 pA input current having an output frequency of 50 kHz. The resulting current sensitivity was ~0.4 fA/Hz.

Beam Trap Current Measurements:

The beam trap had a separate coaxial cable for each electrode of the trap (center, middle, shield). The DC current to the electrodes (for beam focusing adjustments and characterization measurements) were measured using two Keithley 528 Picoammeters (20 nA range). During emission spectra measurements (when the incident beam was swept across the skimmer aperture), the three signal cables were combined into a single cable and measured with a second Keithley 614 digital electrometer (again used on the 20 pA range). The digitation system used for the beam current measurement was identical to that used for the target current measurement discussed above.

Processing Electronics:

Another data rate limitation relative to processing and storage of the final TOF spectra is examined first. This is followed by a discussion of the electronics needed to process the two time axis spectra and the electronics needed to generate the dead time corrections to the yield spectra.

---

† A VFC, instead of an ADC, was used because of a limitation in the data acquisition software. The only parameter which could be continuously monitored (normally at a 10 s sample rate) over the duration of the measurement was a count rate.

<u>Timing Considerations:</u>

Two time axes were used to measure the time of flight of the emitted electron. The 'short' time axis spanned ~150 ns and was used to measure the X-ray flash and the elastic line at high resolution. The energy range covered by this time axis were only those events with emission energies above ~250 eV. The 'long' time axis spanned ~6 μs and was used to measure the total emission spectrum (from the X-ray flash down to 0.05 eV). The electronics used for each axes were essentially identical, differing only in the time frame measured.

The pulse used to sweep the electron beam across the skimmer and therefore to "begin" the sample, occurs in real time, before the signal from the detector indicating that an electron has been detected at the "end" of the sample. The "beginning" count rate is 100 kHz, the "ending" count rate is ~2 kcps (with a maximum of ~5 kcps). The electronics (time-to-amplitude converter or TAC) that measure the flight time requires a finite time to process an event and reset itself after it has been started. As this time is ~8 μs (6 μs (axis time length) + ~2 μs (reset time)), if the "begin" signal (@ 100 kHz) were used to start the TAC, the TAC would always be "dead," i.e., unable to process any signals. If, instead, the "end" signal (2 kcps) were used, the TAC would rarely be "dead." This method requires that the "begin" signals be delayed in time until after the "end" signal is presented to the TAC. Therefore, for this measurement, the "end" signal was used to 'Start' the TAC and a delayed "begin" signal was used to 'Stop' the TAC. This process generates an inverted time scale, with time increasing to the left.

Figure 23 shows a typical TOF spectrum showing the inverted time axis. High energy

79

electrons (with short flight times) are just to the left of the X-ray flash. Low energy electrons

(with long flight times) are at the extreme left side of the plot. The signal to the right of the X-

ray flash comes from background noise counts.

Time Of Flight Spectrum
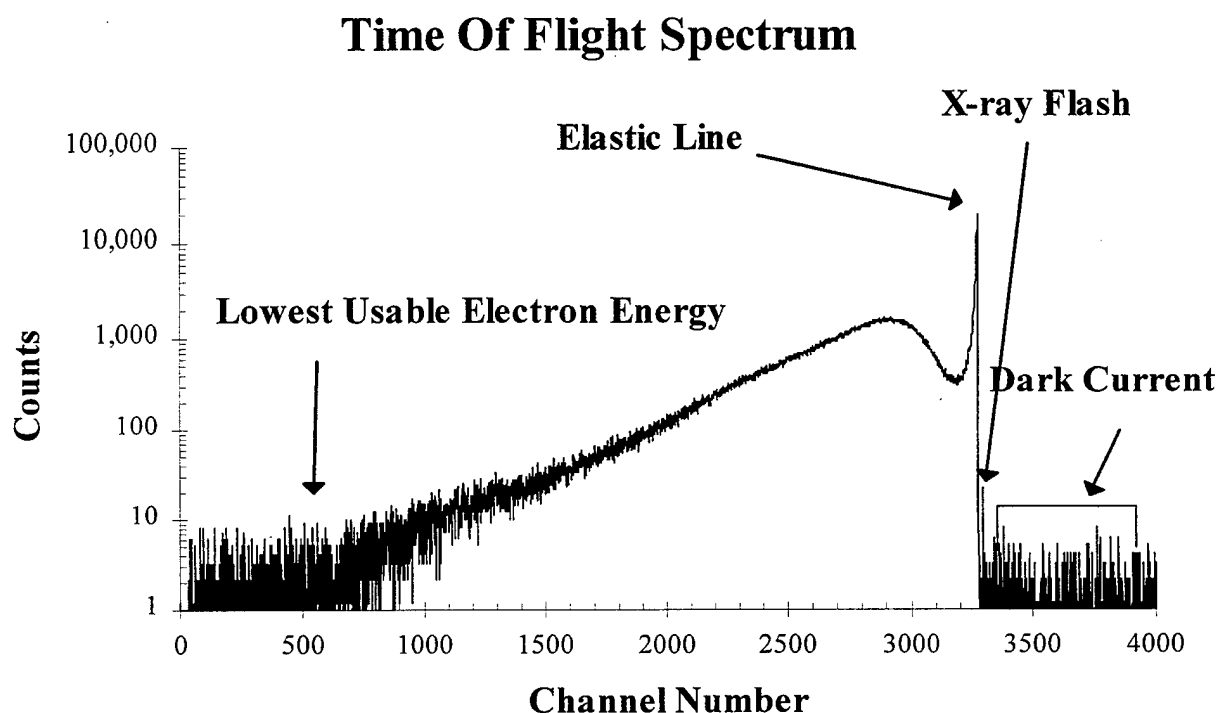
Figure 23: Time of flight spectrum with inverted time axis.

The energy resolution at high emission energies was limited first by the time width of the

incident electron pulse, and second by the timing jitter of the detector and the following

electronics. For this experiment, care was taken to ensure the contribution from the latter was

minimal, i.e., any flight time signal was processed using NIM-negative signals.

Processing Signals:

The primary processing signals were:

- Start signal

- Stop signal

- Time calibration signals

- Dead time and live time clock

- CAMAC system

Figure 24 is a schematic of the electronics used to process the yield signals on two time axis. A single time of flight spectrum is measured, but at two different time resolutions. The 'Long' time axis covers flight times up to 10 μs and therefore measures the entire emission spectrum ($\Delta T = 1.5$ ns). The 'Short' time axis covers flight times up to 200 ns and is used to measure the high energy electron spectrum at a much higher time resolution ($\Delta T = 15$ ps). The electronics in both legs are essentially identical. The 'End' signal is used to generate the 'Start' signal for both of the time to amplitude converters (TACs). The 'Begin' signal is delayed (5.6 μs for the 'Long' and 0 ns for the 'Short' time axis) and is used as the 'Stop' signal for the TACs. Delaying the 'Begin' signal and using it to generate the 'Stop' signal for the TACs produces the inverted time spectrum shown in Figure 23. The measured flight times are then digitized and recorded in event mode by the CAMAC data acquisition system. As the digitation and recording process takes from 2 to 8 μs, a 'Busy' signal for each leg is generated. These signals are used to gate (veto) the system clock and therefore is a measure of the amount of time the electronics was busy and unable to process subsequent events. The gated clock signal is used to calculate the dead time correction for each leg of the CAMAC data acquisition system.
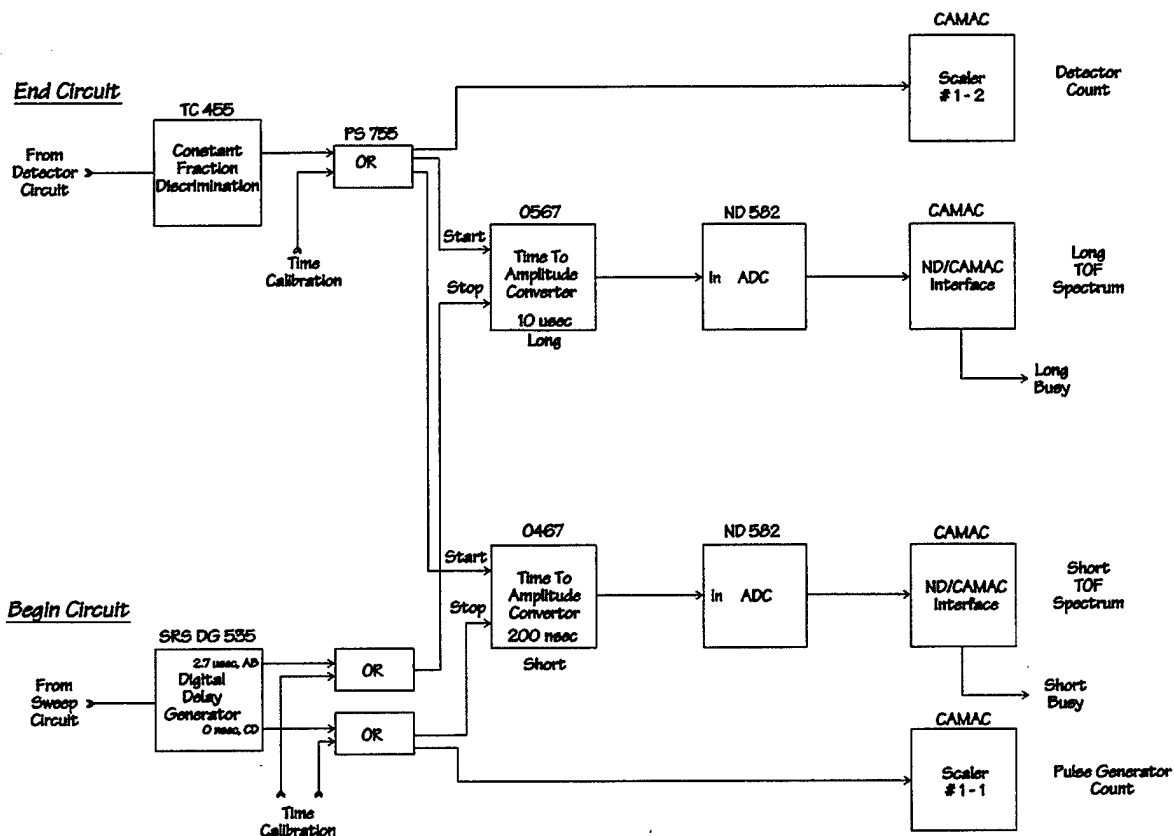
Figure 24: Schematic of the electronics used to process the yield signals on two time axis.

Start Pulse Generation:

The digital Start signal (from the time pickoff of the detector signal, i.e., the 'End' pulse) was "ORed" with the Start signal of the time calibrator. This enabled a time calibration signal to be injected without modifying any existing electronics. The "ORed" signal was presented at the Start inputs for the "long" and "short" time to amplitude converters. This "ORed" signal was also counted by a CAMAC scaler and a visual display to monitor the detector count rate.

Stop Pulse Generation:

The digital Stop signal (from the time pickoff of the sweep pulse signal, i.e., the 'Begin' pulse) was used to trigger the digital delay generator. Two delay times were needed. A longer delay time (channels A&B: 5.57 μs at 100 ns wide) was used with the "long" time axis measurement. The longer delay output was 'ORed' with the time calibration Stop pulse and
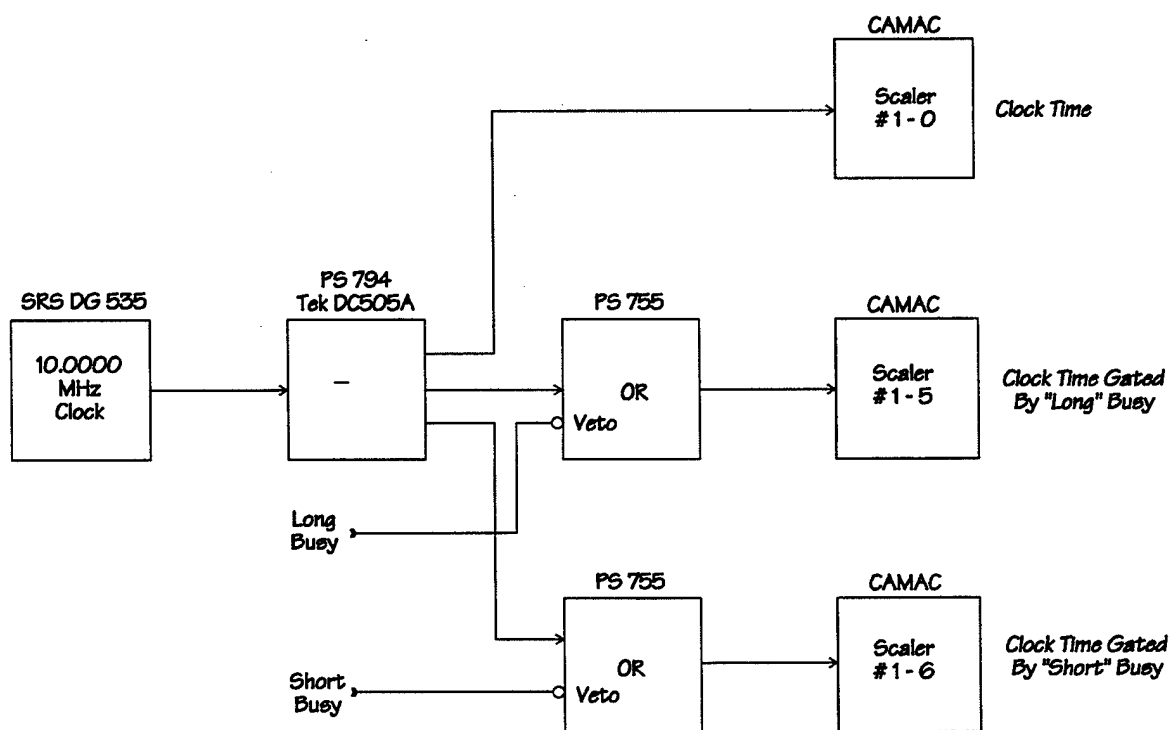
Figure 25: A schematic of the electronics used to process the dead time correction to the yield signals.

presented to the Stop input of the "long" time axis (10 μs full scale) time-to-amplitude converter. This pulse was also fanned out to a visual counter and the CAMAC scaler. The shorter delay

time (C&D: 0 μs at 100 ns wide) was used with the "short" time axis measurement. The shorter delay output was again 'ORed' with the time calibration Stop pulse and presented to the "short" time axis (150 ns full scale) time-to-amplitude converter. This pulse was also fanned out to a visual counter and the CAMAC scaler.

Time Axis Calibration:

The two time axes were calibrated using a standard time calibration unit. The calibration consisted of injecting signals with known time spacing into the Start and Stop signal circuits. This also allowed a check of the "dead time" correction circuity.

Dead Time and Live Time Clock:

Figure 25 is a schematic of the electronics used to process the deadtime correction to the yield signals. The digitation and recording process for the two TOF spectra takes from 2 to 8 μs. A 'Busy' signal for each time axis is generated by the CAMAC data acquisition system. These busy signals are used to gate (veto) the system clock and therefore are a measure of the amount of time the electronics was busy and unable to process subsequent events. The gated clock signal is used to calculate the dead time correction for each leg of the CAMAC data acquisition system.

The dead time correction was accomplished by counting timing pulses from a master clock (10 MHZ) during the data collection interval. The master clock source was the time reference pulse train from the digital delay generator (stable to 1 ppm). The CAMAC data

acquisition system generated a 'Busy' signal whenever a data acquisition channel ('short' or

'long') was 'dead,' i.e., busy processing an event or writing to the disk. This busy signal was used

to gate the master clock pulse train into the dead time scaler (one for the 'short' and one for the
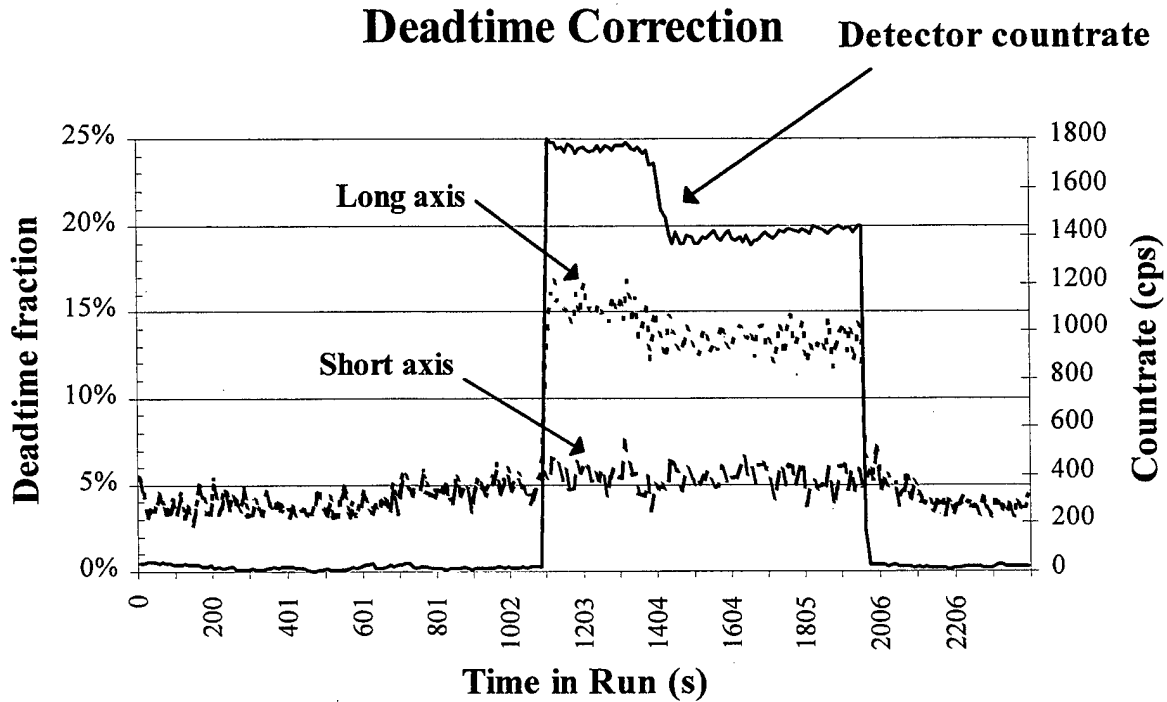
Figure 26: Plot of the deadtime correction during a typical run.

'long' time axis). The clock scaler counted the same pulse train, but without the gate signal. The

ratio of the 'gated' accumulated counts to the 'ungated' accumulated count is a direct measure of

the system dead time. This ratio was used to correct the integrated target and beam trap currents

needed for the determination of the absolute beam current on target (i.e., the corrected total

charge delivered to the target). Figure 26 is essentially a plot of the accumulated counts in 10 s

slices over a typical data run. Each 10 s slice should have 10^7 counts present, therefore the

measured count divided by 10^7 is a direct measurement of the 'live time' for each time axis. The ordinate plotted in Figure 26 is one minis this ratio as a measure of the 'dead time.' The 'Long' time axis shown here is dead for a larger amount of time because each time an electron event is detected, the 'Long' time axis will require ~8 μs to process the event, while the 'Short' time axis will only require ~2 μs. Also shown in Figure 26 is the measured detector count rate. The time interval from ~1100 s to ~1980 s corresponds to the mode IV measurement period of Figure 22.

CAMAC Electronics:

The various signals discussed above were interfaced to the data acquisition system using a microprocessor controlled CAMAC crate. The data was collected in "event" mode. The scaler data (I_{tr}, I_{tp}, live time clock, dead time clocks, detector count and pulse generator count) were accumulated over a 10 s interval and stored on disk with a real time flag attached to the data block. The TOF spectrum ('Long' and 'Short') were acquired in blocks (each block holding up to 1024 events). This data was then stored either when a block was filled or when 1 s of real time had elapsed. This method allowed various systematic checks to made on the data stream, and most importantly, allows an interrupted run to be continued without loss of data. The CAMAC back-plane data bus was controlled with software and allowed the acquisition of multiparameter data. This feature was not used during this experiment (but would be very useful when multiple detectors were present, e.g., during a $X(e,2e)X^+$ measurement.

Section 5: Data Collection

<u>Acquisition Procedure:</u>

The target was mounted on the plate at the end of the target support rod. The acquisition electronics were allowed to stabilize for one hour before data collection began (the components most sensitive to drift were the electrometer and the voltage-to-frequency converter used to digitize the target and trap currents). During the warmup period, the electron filament was outgassed and brought up to working temperature over a 10 minute period[†].

The target was translated away from the detector (by ~10 cm) so as to allow the incident electron beam to enter the beam trap. If the measurement was at a new incident beam voltage value, a beam profile as a function of the lens voltages (V_2, V_3 and V_4) was taken[‡]. These measurements were used to characterize the electron beam diameter and divergence at the target location. Beam diameter and divergence are required to be such that the beam will be fully collected by the beam trap (only a problem at low incident beam energies). Once a beam was characterized, the various lens element voltages were recorded for future use. The electron beam

---

[†]   The 'outgassing' of the filament was distinct from the original activation of an oxide coated cathode. The activation requires a particular sequence of power levels applied to the oxide coated cathode and takes place over a 45 minute time period. During the above outgassing period, no voltages are applied to the electron gun optics.

[‡]   The beam profile measured at the target location is correlated with the beam FWHM measured at the beam trap location (using Equation 3.2 (page 59) and the currents to the pin hole in the middle and center elements of the beam trap). The measured FWHM when projected to the target location agrees with the direct measurement of the beam profile.

characteristics were very reproducible and stable over a ~5 day period. The largest variations occurred after venting the main chamber to atmosphere or replacing the electron gun.

Typically a DC beam current of 10 - 20 nA was established into the beam trap. When packaged by the sweep pulse, this DC value would produce a 1 - 2 pA DC equivalent beam during normal emission spectrum measurements. The DC beam was adjusted to maximize the current into the pin hole in the middle element of the beam trap (I_c) and minimize the current to the last lens element, V_{10}, of the uniform lens system at the output of the electron gun.

The target was then returned to the position on the axis-of-rotation of the electron gun. The location for the 'zero' of the angular readout of the target rotation angle (Φ) was verified against the angular readout for the minimum target current (the target current (I_{tr}) varies as the Sec(Φ) and therefore was only a weak function of the target rotation angle). The DC voltage on the X_0 deflection plate was then increased by +10 V. This bias removed the full incident electron beam from the target (all of the measurements reported here used the same sweep pulse generator, and therefore the same +10 V deflection bias offset voltage value).

The incident angle (Θ, the readout of the electron gun position) and the target angle (Φ, readout of the target rotation position) were then selected (Ω, the target cut angle, was selected when the target was mounted). Voltage was then applied to the electron detector. The data collection program (SDIDAS) was loaded into the CAMAC acquisition computer, and data collection begun. Data was taken using the four 'target location | sweep pulse generator'

88

configurations shown in Table 3:

Table 3   Beam-Target Configurations

Configuration	beam	target
- Mode I:	off	with
- Mode II:	off	without
- Mode III:	on	without
- Mode IV:	on	with

Here, 'on/off' refers to whether the sweep pulse generator was used to sweep the DC beam

across the skimmer hole. While 'with/without' refers to whether the measurement was 'with' or

'without' the target inserted in the incident electron beam. In the 'on|with' configuration, the

target electrometer measures the net target current (I_{tr} which is the difference between the

incident beam current and the backscattered and secondary electron emission currents). In the

'on|without' configuration, the beam trap electrometer measures the incident beam current (I_{in}).

In the 'off' configuration, electrometers measure the zero current values for the 'with' and

'without' configurations. Data was collected in the sequence shown in Table 4.

In the above sequence, the mode pair III/IV could be repeated up to three times during a

data run (the length of a data run was only limited by the capacity of the hard disk (20 Mbyte)

used with the CAMAC data acquisition system).

Table 4   Data Collection Sequence

Mode	Length	Important parameter	
I	~ 2 min	target current	I_{tr0}
II	~ 2 min	trap current	I_{tp0}
III	~ 5 min	trap current	I_{tp}
IV	~ 20 min	target current	I_{tr}
III	~ 5 min	trap current	I_{tp}
II	~ 2 min	trap current	I_{tp0}
I	~ 2 min	target current	I_{tr0}
IVd	~ 10 min	trap current	I_{tp}'

A modification of the fourth configuration was also used (Mode IVd: on|with). Here, the target was displaced along the incident beam direction to a location where the target was not within the acceptance solid angle of the detector. The detector signal was, therefore, a measure of the flux of electrons that arrive by other than a direct, straight-line path from the target. The resulting 'offset' spectrum peaks at long flight times. Figure 27 shows the 'direct' spectra, the 'offset' spectra and the 'corrected' spectra obtained by subtracting the offset spectrum (normalized to the same charge delivered to the target) from direct spectrum. In Figure 27, the 'corrected' spectra was multiplied by a factor of 10 to shift the display away from the original spectra. Without the correction for the offset signal, the total electron production coefficient (σ: integrating the yield spectrum from 0.2 eV to beam energy) would have been too large by 2.8%. These late, indirectly-arriving electrons are indistinguishable from 'true' low energy electrons (these are the 'late high energy' electrons discussed in the section on low energy cutoff of Section 2). This structure (peak) established the "low energy" cutoff of a measurement. The 'Mode IVd'

Direct, Offset and Corrected Spectra
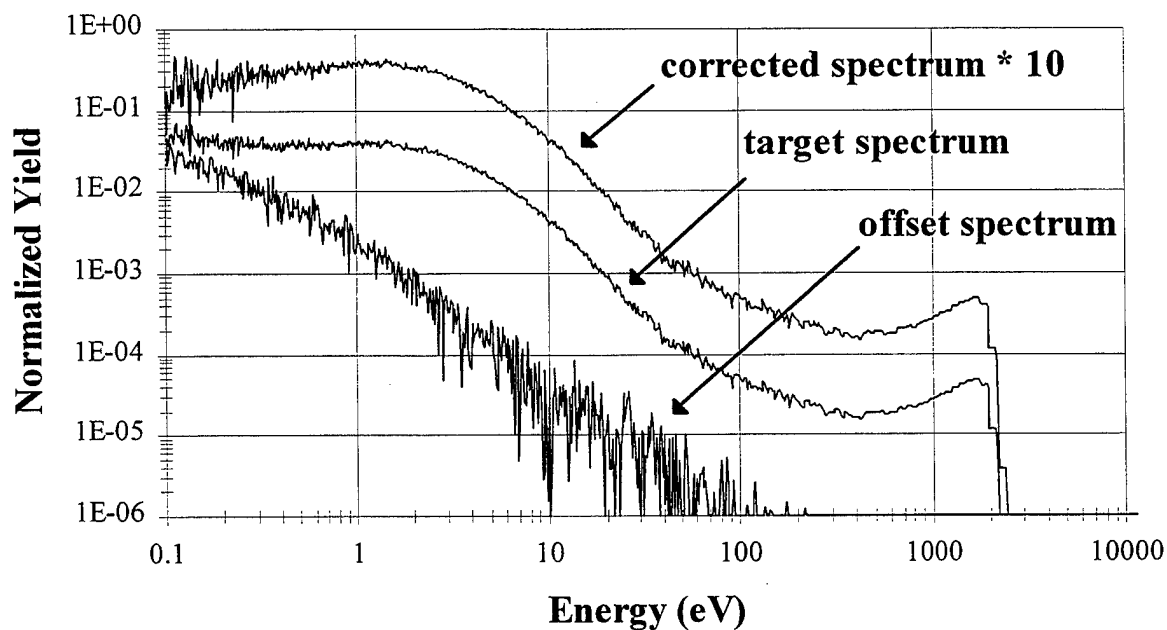
Figure 27: Direct, Offset and Corrected spectra.

measurement was not taken during the above sequence, but was normally taken in a separate data

collection run (this was necessary because of the difficulty in 'time selecting' the TOF data).

Section 6: Measurement Calibration and Accuracy

<u>Introduction:</u>

This section will examine the accuracy associated with the output of a measurement: the absolute value of secondary and backscatter electron yield as a function of emission energy and angle. To place the measured spectra on absolute energy and yield scales, various absolute normalizations are required:

Secondary and Backscatter Yield Accuracy:

1) absolute efficiency of the MCP/SEM detector: needed to correct for the energy dependance of the electron detection system

2) total charge delivered to the target: needed for spectra normalization

3) 'dead time' associated with each time axis channel: needed to correct for the charge delivered during periods when the data acquisition system is unable to process an event

Energy Scale Accuracy:

4) calibration of the time axis, including "time zero" channel location: needed to put the spectra on an absolute energy axis

Solid Angle Accuracy:

5) solid angle subtended by the target and detector: needed to normalize the spectra for solid angle.

The accuracy associated with each of the above factors is discussed in the following five

sections.

I.   Absolute Detector Efficiency:

The measurements reported here are the 'absolute' secondary and backscatter electron yield differential in both energy and angle. These measurements require that the 'absolute' efficiency of the electron detector be known over the entire emission energy range measured (0.1 eV to 20 keV). A problem arises in that the gain of the detector (both for the SEM and the MCP) decreases slowly with use[†]. Therefore, the detector needs to be periodically calibrated during the measurement series.

The calibration procedure involves measuring the output count rate (R_E in counts/sec) of the detector to a known incident input current (I_E in Ampere) at each input energy of interest (E_{in}). The absolute efficiency was given by

$$\epsilon_m(E_{in}) = R_E * q / I_E \tag{6.1}$$

where 'q' was the charge on a single electron (1.6×10^{-19} C) and 'm' is for 'measured' efficiency (to distinguish it from ϵ_c used later).

Although the calibration is a straight forward process, a difficulty lies with measurement of the incident current (I_E). The maximum output count rate that a MCP pair can process without significant shifts in the output gain is ~50 kcps. This limits the input DC current to values less

---

[†]   The gain of a SEM/MCP will decrease by a factor of ~2 after processing approximately 10^{12} events.

than 8 fA. This current level can be directly measured with an electrometer only if certain

precautions (shielding against noise pickup and leakage current generation) are taken. The DC

current measurements (I_E) were made with a Faraday trap, the SEM/MCP pair counting

measurement (R_E) were made with the detector mounted inside of the same Faraday trap. The

absolute efficiency measurement then requires switching between two 'modes' of detector

operation: Pulse Mode (SEM/MCP pair) and Current Mode (Faraday trap).

The current mode configuration was used to measure the input DC current to the Faraday

trap. Figure 28 is a schematic diagram of detector (MCP pair/Faraday trap) configured in

"current mode." In this configuration, the four wires from the center cylinder (in Figures 12 and

13, the high voltage resistor chain leads, detector input surface lead and the signal lead) were
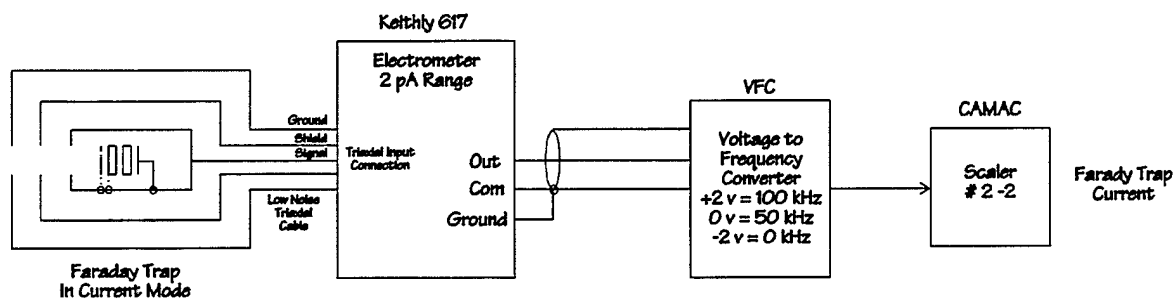
Figure 28: Diagram of detector (MCP pair/Faraday trap) configured in "current mode."

shorted together and this single wire constituted the center connector of the triaxial configuration.

The middle cylinder constituted the middle shield of the triaxial connection, and the outer

cylinder (which was a chamber ground) constituted the outer shield. The three cylinders/shields

were connected to the electrometer input using low-noise, triaxial cable. The beam current to the

inner cylinder is measured by the Keithley electrometer, the output signal (2 V output) was

digitized with the same voltage-to-frequency converter (VFC) system used to monitor the target

and beam trap currents during the secondary and backscattered emission measurements. This

count rate was continuously monitored by the CAMAC data acquisition system during the entire

calibration measurement. The electrometer current data was averaged over a 10 second sample

period. Data was taken in 'event mode' and therefore had a real-time flag attached.

The pulse mode configuration was used to measure the output count rate from the

SEM/MCP detector. In this configuration, all three shields (Figure 13) were connected to

chamber ground. The high-voltage source was connected to the resistor chain, and the anode

signal output cable was connected to a charge sensitive preamplifier (Figure 12). Figure 29 is a
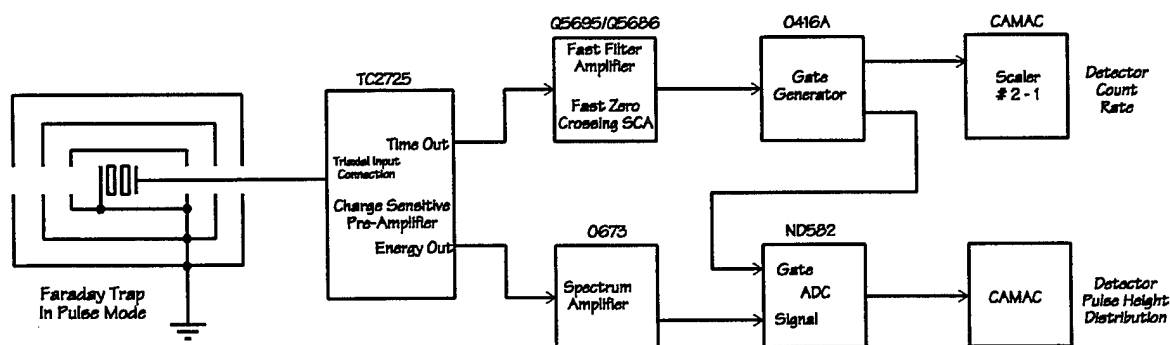
Figure 29: Diagram of detector (MCP pair/Faraday trap) configured in "pulse mode."

schematic diagram of detector (MCP pair/Faraday trap) configured in "pulse mode." In this

configuration, the detector measures individual electrons. Voltage is applied to the MCP resistor chain and the anode output is connected to a charge sensitive preamplifier. The 'Energy Output' of the preamplifier was further amplified and used to monitor the pulse height distribution of the SEM/MCP during calibration (to ensure no excessive gain shifts were present, see Figure 11). In addition, the 'Time Output' from the preamplifier was digitized and constituted the count rate from the detector. The pulse height distribution and the count rate were continuously monitored by the CAMAC data acquisition system during the entire calibration measurement. The output pulse rate was averaged over a 10 second sample period (with time flag attached), while the pulse height distribution was recorded as an average over the entire calibration run.

The measurement of the absolute detection efficiency required a slight modification of the interior electron gun/beam trap geometry. The beam trap mounted across from the electron gun was removed (it was mounted in a cradle to facilitate this change over), the target holder withdrawn into the target chamber, and the electron gun rotated to the $\Theta = 0°$ position (i.e., the electron gun beam was directed down the throat of the Faraday trap). The Faraday trap was changed to the 'current mode' configuration. The nominal 20 nA incident electron beam (at the selected beam energy E_{in}) was reduced to a value below 10 fA by adjusting the grid (G_0) voltage on the electron gun[†].

[†]   The grid voltage was routinely used to adjust the incident beam current during normal operation of the electron gun. The G_0 value had a slight effect on the focus position of the electron gun beam, but this movement was not considered significant during this measurement (the maximum beam diameter was 1 mm while the entrance aperture to the Faraday trap was 20 mm diameter). See a further discussion of this at the end of this section.

The calibration procedure consisted of (1) configuring the Faraday trap to current mode, (2) adjust G_0 to cut off the incident beam and measure the Faraday trap current without the electron beam present (I_{E0}) for ~2 min, (3) adjust G_0 to obtain the required current in the Faraday trap and measure the trap current (I_E) for ~5 minutes, (4) switch to the pulse mode configuration, (5) measure the SEM/MCP output pulse rate (R_E) for ~1 minute, (6) return to current mode configuration, and (7) re-measure the Faraday trap current (I_E). The second measurement of the Faraday trap current was needed to confirm that the incident electron beam had not drifted appreciably during the pulse mode measurement. The procedure was then repeated at one or more lower incident beam currents as a check for possible count rate gain shifts (the pulse height distribution of the output pulse was monitored continuously during these measurements, Figure 10).

Figure 30 is a plot of the Faraday trap reading during a typical calibration data run. 'Pulse mode' configuration was between run times 791 s and 994 s. The beam current before and after the MCP measurement ('pulse mode') has a linear drift as shown. The current during the MCP measurement is corrected for this drift. The ratio of the MCP count rate (right hand scale) to the linear estimate of the beam current during the MCP measurement is a direct measurement of the efficiency of the MCP.

Calibration data was processed under the assumption that any drift between the initial DC Faraday trap current measurement (procedure 2 above) and the following measurement (6 above) was linear. For most of the calibration runs reported here, the DC Faraday trap current for the

97

Detector and Faraday Trap Signals

MCP   **140 s decay**

fit to zero

fit to beam current
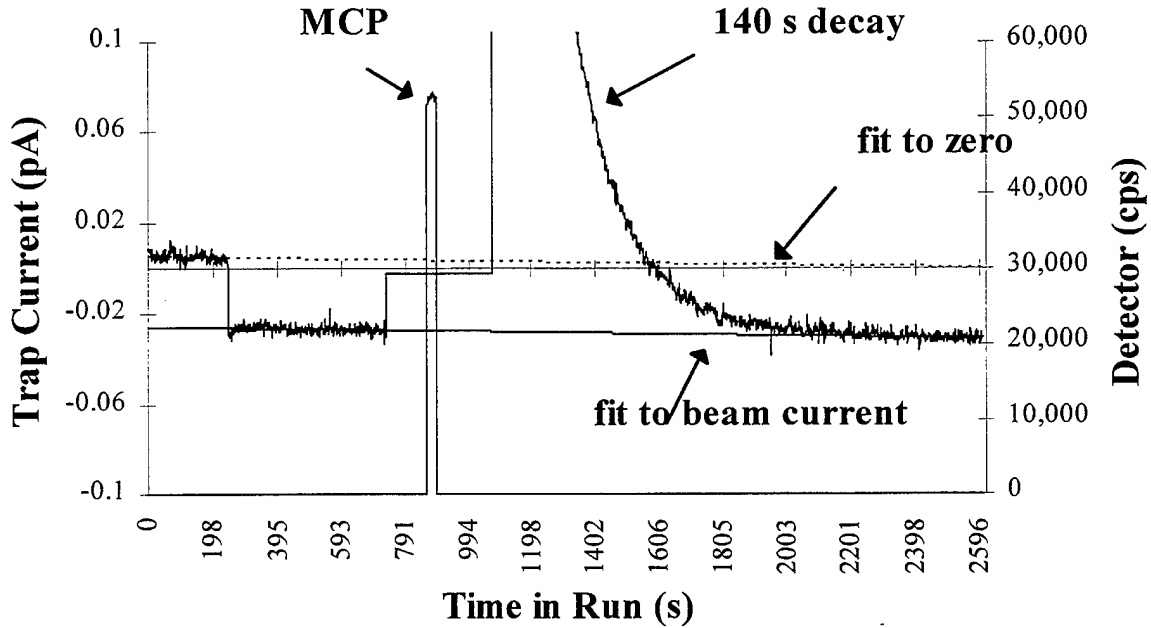
Figure 30: Faraday trap current and MCP count-rate during a typical calibration data run.

following measurement (6) overlapped the extrapolation from a regression fit of the initial DC

Faraday trap current (2), and the assumption of a linear drift was therefore considered valid.

One interesting problem developed during this measurement. As seen from Figure 30,

the measured Faraday trap current did not immediately return to the value it had before the

change over to pulse mode configuration. Instead, the Faraday trap current slowly (after 15

minutes) returned to the previous value. The slow return was due to dielectric absorption (charge

storage) in the Teflon® insulator when high voltage was supplied to the SEM/MCP detector.

Dielectric absorption occurs when an insulator temporality stores charge when placed in an

electric field. The charge is then released when the external field is removed. The amount of stored charged and the time constant associated with this process, varies with the insulator material. The time required for the stored charge in the Teflon® insulator to leak off is seen to be smaller than the time constants associated with beam drift.

Initially, a quartz glass vacuum feedthrough was used for the electrical connection to the center cylinder of the Faraday trap. As it turns out, this was a very bad choice. The glass was originally chosen because the leakage resistance needed to be above 50 TΩ. Unfortunately, the dielectric absorption decay time constant for quartz glass was over 45 minutes. Replacing the glass vacuum feedthrough with a virgin PTFE vacuum feedthrough reduced the Faraday trap current time to less than 10 minutes[†].

Figure 31 is a plot of the measured efficiency at two incident beam energies as a function of incident beam current. Not shown is a dramatic decrease in measured efficiency at count rates above 200 kcps due to gain shift. The error bars shown are estimated from the noise of the measured incident beam current. As the DC current during the MCP count rate measurement is determined from fitting the DC current before and after the measurement (i.e., a averaging process), this noise figure is an overestimate of the measurement error.

[†]   The total time required for the electrometer signal to return to the beam value depends on the total charge absorbed by the insulator. This in turn depends on the voltage applied (always 2700 V in our case) and the time this voltage is present. Therefore the time in "pulse mode" configuration was kept to a minimum.

Detector Efficiency
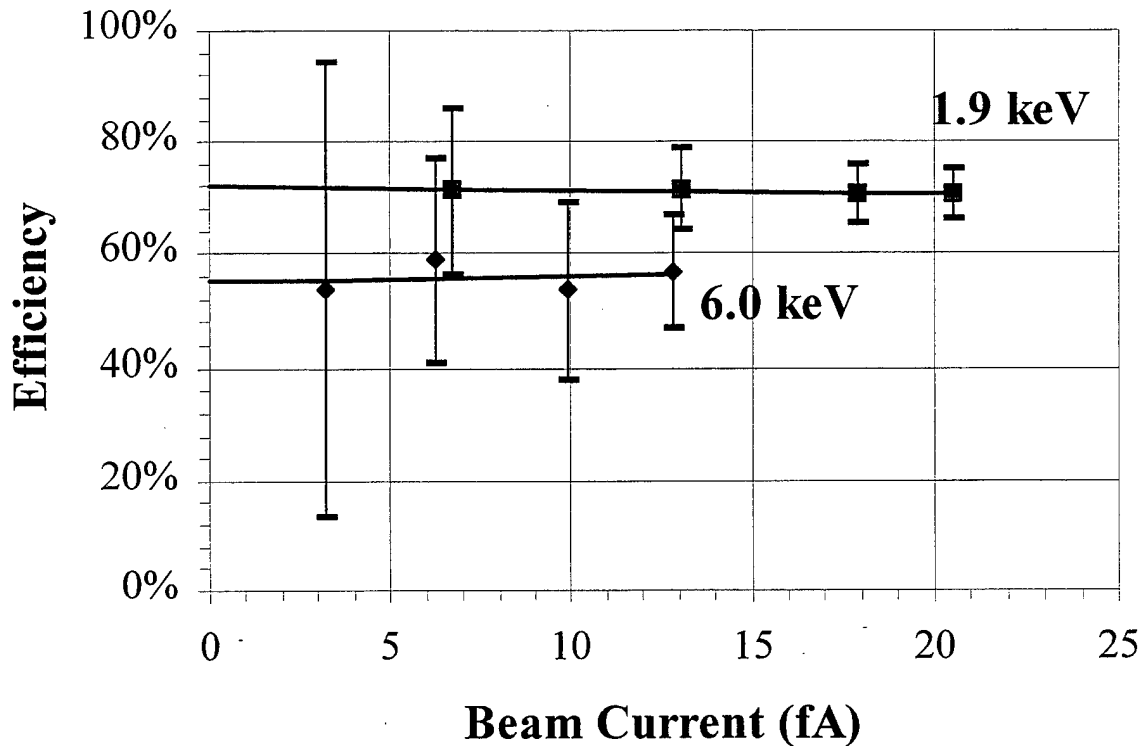
Figure 31: Plot of the detector efficiency as a function of incident electron current.

It is important to understand that the above measurement is not a direct measurement of the efficiency of a bare SEM/MCP pair ($v(E_{in})$), but is the efficiency of the detector system (which includes the physical detector and the following electronics). This distinction comes about from two sources: first the bias on the front surface of the MCP adds ~270 eV to the energy of the incident electron (this was done to improve the detection efficiency for low energy

electrons[†]). Secondly, the graphite coated grid, used to define the end of the flight path drift region, intercepts ~6.6% of the incident electron flux and thereby reduces the detection efficiency by the grid transmission (T). This reduction will be offset to some extent by the secondary electrons generated by the intercepted incident electrons. These secondary electrons (peak energy near 1 eV) will subsequently be detected by the MCP with near unit efficiency (due to the addition of the bias voltage energy).

$$\epsilon_c(E_{in}) = T*\nu(E_{in}+B) + (1-T)*\int(\sigma(E_{in},E_s)*\nu(E_s+B)*dE_s \qquad (6.2)$$

where 'c' is for 'calculated' efficiency.

The addition of the bias voltage is independent of incident electron energy, and effectively contributes the bare detector efficiency curve of the MCP shifted by 270 eV (the $\nu(E_{in}+B)$ term in Equation 6.2). The grid contribution is a function of the incident electron energy (through $\sigma(E_{in})$) and will have a small effect on the total detector efficiency (the integral over the secondary electron emission energy E_s in Equation 6.2). The integral (grid contribution) will be maximum at the electron energy corresponding to the maximum the secondary electron production coefficient (σ for carbon is ~1 at E_{in} ~300 eV).

Figure 32 is a plot of the total detector efficiency as a function of incident electron energy (with a bias voltage of 270 V on the front MCP). The curve is the calculated efficiency based upon a simple secondary electron production model (Ref. 12) given by Equation 6.2 with

---

†   The maximum efficiency of a MCP occurs at an incident electron energy of ~300 eV.

corrections for the secondary electron production at the grid and a bias voltage on the front

surface of the MCP. The data points are direct measurements of the efficiency discussed above.

Detector System with 270 V Bias on Carbon Coated Grid
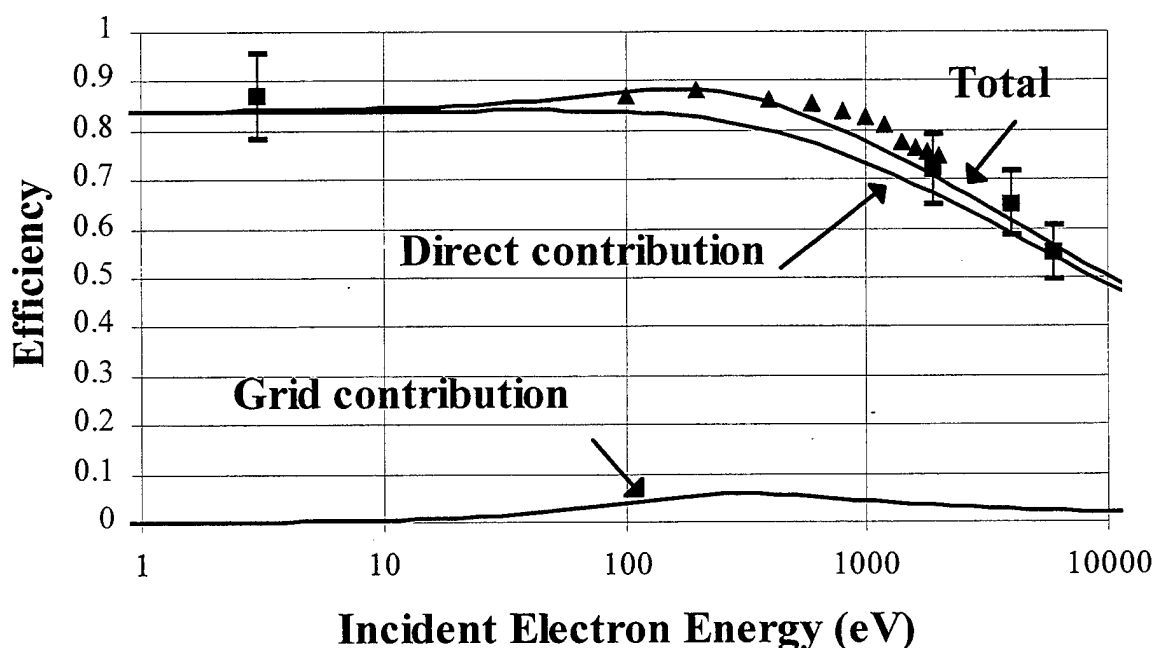
Figure 32: Plot of the detector efficiency as a function of incident electron energy.

The model prediction has a number of parameters which were adjusted to fit the shape and values

of the measured detector system efficiency[†]. The contribution of the grid is seen to enhance the

---

†   The model parameters are: the stopping power of the MCP material, a factor that takes
into account the fraction of the excited electrons that diffuse toward the surface, mean free path
for absorption of the secondary electrons during their diffusion toward the surface (an effective
escape depth), and lastly a factor related to the probability that an electron which reaches the
surface passes over the surface barrier into the vacuum. These factors essentially combine to
generate the nominal values of δ_{max} and E_{max} for the secondary production coefficient.

102

efficiency at incident energies below 300 eV. The shape of the measured efficiency curve agrees with previous measurements of the relative efficiency of a similar detector system (Ref. 13).

In the above model: $\epsilon_c(E)$ was adjusted to fit the measured calibration data while $\epsilon_m(E)$ was used to correct the measured emission spectrum for detector system efficiency. The factors that affect the accuracy of the final system efficiency derive from the two terms in Equation 6.1, the accuracy of the incident current measurement, I_E, and the accuracy of the MCP output count rate, R_E. The errors related to the accuracy of the current measurement can be divided into two groups, those associated with the current measured (i.e., the current source) and those associated with the measurement (i.e., the electrometer). In the first group are external background currents and noise and drift in the incident electron beam. In the second group are leakage currents, the electrometer voltage burden and the calibration of the electrometer and the following electronics. Errors related to the counting measurements can be divided into two groups: dead time correction and errors associated with gain shift at high output count-rates. Each of these error sources are discussed below.

Accuracy of the Incident Current Measurement:

Current Source Errors - External Sources:

It is assumed that the electrometer and the MCP measure the same electron beam. The important word here is 'beam' -- the Faraday trap|SEM/MCP will measure the same current only if the current enters the trap on axis. If the electron beam enters the Faraday trap at an obtuse angle (i.e., from the side), the beam will still be measured by the electrometer, but since it will

103

miss the grid in front of the SEM/MCP, the SEM/MCP system will not "count" it. The electrometer will measure all electrons that pass into the inner cylinder of the Faraday trap, if the incident electron enters at an angle no larger than $50°$ from axis (1.4π sr field of view). The grid of the MCP is 8 cm behind the entrance aperture of the inner cylinder. To be detected by the MCP, the incident electron must now enter at an angle no larger than $7.5°$ from axis (0.02π sr: the detector/target geometry was designed to include only the target region in the field of view). Because of machine geometry, any electron from the electron gun that enters the Faraday trap will also pass through the grid of the MCP detector. For an electron to enter the Faraday trap in this $7.5°$ to $50°$ range, it would first need to "bounced" once from the inside edge of the Faraday trap aperture or at least twice from other surrounding surfaces. Both of these possibilities are small: the inside edge of the aperture is cut to a knife edge to reduce such scattering and the interior surfaces of the chamber are coated with graphite to again reduce such scattering. An obvious potential source of such multiple scattered electrons would be a divergent electron beam from the electron gun. Such a beam would hit the front face of the Faraday trap and begin the multiple scatter sequence.

During a detector calibration measurement, the incident electron fluence is assumed to be contained in a beam with a diameter much smaller than the input diameter of the Faraday trap (1.9 cm diameter) and directed along the chamber axis[†]. The spacial diameter of the electron beam was measured at the target location and the beam divergence was derived through

---

†   A laser was used to align the internal components.

measurements of the beam diameter at the entrance of the beam trap and at the exit of the electron gun (as discussed in Section 3). Both of these measurements were made with emission currents of the order of nanoamperes. The beam current used during the calibration of the detector system is six orders of magnitude smaller (femtoamperers). The assumption is made that the electron optics (i.e., image diameter and the beam divergence) do not change as the grid voltage (G_0) is changed from -5 V (normal operating value with beam current of the order of 10 nA) to -50 V (the voltage required to reduce the DC beam current to the fA range). This assumption, although not directly checked[†], is reasonable[‡].

[†]   During the writing of this report, it was realized that this assumption needed to be checked experimentally. A future measurement is planned in which the incident electron beam, at high current, is directed down the throat of the Faraday trap. When the electron gun is rotated about the target position, the incident electron beam will sweep across the entrance aperture of the Faraday trap. The measured Faraday trap current as a function of rotation angle (or calculated displacement) will be a direct measurement of the electron beam diameter. The beam current will then be reduced to the femtoampere range and the measurement repeated. It is expected that these two measurements of the beam profile will agree, i.e., electrons measured during the detector calibration are electrons in a 'beam' from the electron gun.

[‡]   The voltage applied to the grid aperture controls the field penetration of the anode potential into the cathode region, i.e., it controls the electric field strength at the cathode surface. For an oxide coated cathode (a plane cathode), an increase in field penetration will simply increase the effective area from which electrons are extracted from the cathode. But as the focusing properties are influenced by the off-axis emission components, the final beam (image) diameter is not expected to be changed. When the oxide coated cathode is replaced with a tungsten wire filament, the simple plane geometry of the grid/cathode is replaced by that of a cone. As the grid potential is increased (i.e., becomes less negative), the anode field penetration is increased, and the emission area now used to supply the required current comes from the side of the cone (especially at high emission). The emitted electrons will have a larger radial velocity component and the image diameter is corresponding larger (this effect is observed for high current extraction from point cathodes). Fortunately in the present case, the anode field penetration is reduced to such an extend that only the very tip of the cathode supplies the beam electrons and the beam diameter is not expected to change.

Current Source Errors - Drifts:

The time scale associated with drift in the incident electron beam (30 min) is longer than that required for a measurement (10 min) (as seen from Figure 30). Even were this not true, the "pulse mode" measurement always occurs within 5 minutes of the end of the "current mode" measurement[†]. If we can assume that the drift remains constant for this short time period (i.e., 5 min), then the DC electron beam current extrapolated from the just completed current mode measurement can be used to calculated the detector efficiency. Since extrapolation is always suspect, the measurement was always extended (~30-45 min) to ensure that the DC electron beam returned to the value at the beginning of the "pulse" mode.

The drift in the "zero" of the electrometer[‡] was always on a time scale (~120 min) which was much longer than the total time required for a measurement (~45 min). The drift observed in the "zero" of the electrometer was sufficiently stable that a "zero" check at was not always repeated at the end of a calibration run.

Electrometer Measurement Errors - Voltage Burden, Bias Current and Noise:

The source impedance of the Faraday trap (R_s) was measured at over 30 TΩ. The Keithley 617 electrometer has a 'voltage burden' from the voltage drop caused by the measured

---

[†]   Remember we want to minimize the total time high voltage is applied to the MCP detector so as to minimize dielectric absorption.

[‡]   This was really the "beam off" state generated by cutting off the electron gun with a large negative value for G_0 (<-90 V).

106

input current across the input impedance of the electrometer. The voltage burden is quoted to be less than 1 mV at an input current of 2 pA; this is an equivalent input impedance (R_m) of less than 0.5 GΩ[†]. The current measured by the meter (I_m) is related to the source current (I_s) by the expression:

$$I_m = (I_s + I_b) / (1 + R_m/R_s) \tag{6.3}$$

The ratio R_m/R_s is <20 ppm and, as such, constitutes a insignificant correction.

The input bias current (I_b) for this electrometer is quoted as less than 5 fA. This bias current is of the order of the measured source current (1 to 10 fA) and as such must be corrected for. The measurement procedure, in which the difference in electrometer reading with and without incident beam was taken, automatically corrects for the presence of the electrometer bias current (i.e., I_E - I_{E0}).

The measured current noise for the Faraday trap (electrometer and electron beam noise) was 2 fA RMS[‡].

[†] The input impedance of the electrometer is a dynamic impedance which is a function of the feedback resistance and the open loop gain of the "operational amplifier" used in the electrometer circuit. The values quoted here (from Keithley literature) are maximum values and are used here only to estimate the size of potential error sources in the DC beam measurement.

[‡] As seen in Figure 30, the incident electron beam current during a calibration data run will be measured over a 5 minute period prior to the measurement of the MCP count rate. The initial beam current measurement is used to establish the drift in the incident current. The final value used to calculate the incident current during the MCP measurement is a linear fit to the measured current.

Electrometer Measurement Errors - Electrometer Calibration:

The accuracy specification of the Keithley 617 electrometer (PMEL calibration) on the 2 pA range are $\pm$(1.6% of the reading plus 6.6) fA. The first number represents the accuracy of the value for the transconductance of the electrometer and ultimately is traceable to knowledge of the value of the feedback resistor used in the electrometer and the linearity of the overall operational amplifier. The second number represents the absolute accuracy in the knowledge of the zero of the electrometer i.e., a measure of the electrometers input bias current and offset voltage. For example, the absolute accuracy of a 5 fA current would be $\pm$ 8.68 (=0.08 + 6.6) fA. Since the present measurements involve taking the difference between two current readings (I_E - I_{E0}), the absolute accuracy in the zero does not enter and only the 1.6% of the reading will enter or, for the above example, the accuracy of a 5 fA difference will be $\pm$80 aA.

The calibration of the Keithley 617 electrometer/voltage-to-frequency-converter/CAMAC scaler was performed by measuring the output frequency for a known (as read on the Keithley electrometer) current injected into the Keithley electrometer. The entire Faraday current measurement system had an conversion gain of ~41.68 aA /Hz. This number has the same overall accuracy as the Keithley 617, i.e., $\pm$1.6% of the reading.

Accuracy of the Counting Measurement - Dead time corrections:

A dead time correction, as such, to the detector count-rate is not needed during the detector efficiency data run. A dead time correction would be needed here only to correct a measured spectra for the time during which the data acquisition system is dead and unable to

process an event. During the calibration data run, the measured pulse height spectra is taken only to monitor the shape of the pulse height distribution relative to the threshold level of the following electronics[†]. The scaler reading is the accumulated count during a time period approximately 10 s long. The 10 second length is set by the computer internal clock and is only approximately constant (since the CPU does not respond to the clock interrupt immediately). Therefore the length of the measurement period is not constant. Each measurement period length is measured directly by counting a clock with a known rate (10 MHZ) during the same measurement period as the detector count. The measured clock count and the known clock frequency can then be used to calculate the unknown length of the measurement period and obtain the correct detector count-rate. The time during which the clock scaler and detector scaler are dead (i.e., when they are being read by the data acquisition system) is not of concern since only the count-rate is of interest, not the total count.

Accuracy of the Counting Measurement - Gain shift Errors:

The pulse height distributions shown in Figure 11 were data taken with an incident electron beam energy of 1900 eV at the three input currents indicated. The efficiency derived from these measurements are those shown in Figure 31. At an output count-rate of 30 kHz, only a small fraction of the electron events are missed (i.e., are below the threshold level and are not counted by the following electronics). But as seen from Figure 11, at 100 kHz output frequency,

---

[†]   If the spectra were integrated and this number used to determine the total number of electrons arriving during the measurement period, the spectra would then need to corrected for the events "missed" during the time the data acquisition system were processing a previous event.

a larger number of the electron pulse with low gain are missed. Monitoring the pulse height distribution during the efficiency measurement and insuring that the calculated efficiency is independent of output count rate (by plotting the calculated efficiency vs input current as was done in Figure 31) will eliminate any error associated with gain shift in the detector.

II. Absolute Charge Delivered to the Target:

The total charge delivered to the target could not be measured directly, instead the incident electron current (I_{in}) was integrated over the length of the data run. As discussed in Section 5, the incident beam current (I_{in}) was calculated from the target current (I_{tr}) measurement. A value for the total electron yield coefficient ($\sigma'^{\dagger}$) was chosen that would force the measured trap current (I_{tp}) to equal the calculated incident beam current (I_{in}) at the changeover from Mode III to Mode IV. This value for total electron yield coefficient (σ') was then used to normalized the total yield measurements using:

$$Q_{in} \quad = \quad \int I_{tr}/(1-\sigma') \, dt. \quad\quad\quad (6.4)$$

For those values of incident beam energy which have a value of σ' near unity (the floating potentials), the uncertainty in the value for Q_{in} becomes very sensitive to the uncertainty in the value for σ'. First, the denominator in Equation 6.4 approaches zero, and therefore any

---

† Here σ' will be used to represents the value obtained when the calculated incident current was forced to match the beam trap current at mode changeover, σ represents the value derived from integration of the emission spectrum.

110

uncertainty in the knowledge of σ' will magnify[†] the uncertainty for Q_{in}. Second, as the integral remains finite, the measured target current (I_{tr}) also approaches zero and the signal to noise ratio associated with this measurement nears one. Therefore a measurement of the delivered charge near the floating potentials will have a large uncertainty in the value of Q_{in} associated with them. The measurements reported here were all made with an incident beam energy removed from the floating potentials and therefore the uncertainty in Q_{in} is dominated by the consideration discussed in the next two paragraphs.

The choice of σ' was made by plotting the trap current and the calculated incident current against run time and adjusting the value for σ' to force these two currents to agree at the changeover points (Figure 21). The final choice for σ' was subjective and therefore the error associated with the final value for Q_{in} was difficult to quantify. In a typical run, the difference between what was thought to be a 'good' match and what was obviously a 'poor' match[‡] changed the final value for Q_{in} by less than 5%.

Another indirect measurement of the accuracy of the value for Q_{in} (i.e., the accuracy of the value for σ') can be obtained in the value for σ (= δ + η) calculated from integrating the measured emission spectrum over the emission energy range and solid angle (using Equations 0.2 and 0.3). The agreement between these two determinations of σ is sometimes poor and is

---

[†]   The relative uncertainty in the calculated incident current dI_{in}/I_{in} varies as $d\sigma'/(1-\sigma')$.

[‡]   Where the difference was a displacement in the calculated incident current (I_{in}) comparable to the beam noise in the target current (I_{tr}).

discussed in Section 8.

Measurement Error:

Voltage Burden, Bias Current and Noise

The source impedance (R_s) of the beam trap and that of the target were measured to be over 200 GΩ. The Keithley 614 electrometer has a 'voltage burden' from the voltage drop caused by the measured input current across the input impedance of the electrometer. The voltage burden is quoted to be less than 0.2 mV at an input current of 20 pA; this is an equivalent input impedance (R_m) of less than 10 MΩ. The input bias current (I_b) for this electrometer is quoted as less than 60 fA. The current measured by the meter (I_m) is related to the source current ($I_s = I_{tp}$ or I_{tr}) by the expression given in Equation 6.3. The ratio R_m/R_s is <50 ppm and, as such, constitutes an insignificant correction.

The bias current (I_b <60 fA) is much smaller than the typical beam trap current (~1 pA). As the target current is much smaller and can, in principal, equal "zero" (when σ = 1), the bias current is of importance during the target current measurement and must be corrected for. The measurement procedure, by which the difference in electrometer readings, with and without incident beam (I_{tp} - I_{tp0} or I_{tr} - I_{tr0}), was taken, automatically corrects for the presence of the electrometer bias current[†].

---

† As seen in Figure 22, the incident electron beam current and target current during a data run were measured both without (Modes I & II) and with (Modes III & IV) current delivered to the target. The 'without' measurement were used to establish the "zeros" of the electrometer and to correct for any background currents present.

The measured current noise for the beam trap (electrometer and electron beam noise) was

~0.15 pA RMS while that for the target current (electrometer and electron beam noise) was ~0.05

pA RMS.

Electrometer Calibration:

The accuracy specification of the Keithley 614 electrometer (PMEL calibration) on the 20

pA range are ±(1.5% of the reading plus ±50) fA. The first and second numbers here have the

same significants as discussed in the MCP calibration section above. Since the typical current

measured is now ~1 pA the absolute accuracy would be ±(0.015 + 0.05) pA. Again, a difference

measurement is used to remove the accuracy error associated with the "zero" error, and only the

1.5% of the reading will enter. For the above example, the accuracy of the 1 pA current

difference will be ±15 fA.

The calibration of the Keithley 614 electrometer/voltage-to-frequency-converter/CAMAC

scaler was again done by measuring the output frequency for a known (as read on the

electrometer) input current injected into the Keithley electrometer. The entire Faraday current

measurement system had an conversion gain of ~409.5 aA /Hz. This number has the same

overall accuracy as the Keithley 614, i.e., ±1.5% of the reading.

III. Dead Time Correction:

The dead time correction can be as large as 15% (at high detector count rates). The

accuracy of this correction depends on the accuracy of the master clock and the time required for

the processing electronics to gate the master clock. The worst case would be when the 'gated' dead time clock misses two master clock pulses each event. This would correspond to an uncertainty in the accuracy of the dead time correction of ±0.4% at a detector count rate of 2 kcps.

IV. <u>Time</u> <u>Axis</u> <u>Calibration:</u>

The accuracy of the time axis calibration is quoted as ± 0.005% of the full scale range (i.e., ±10 ps on the 200 ns scale and ±0.5 ns on the 8 μs scale). These numbers, along with the linearity of the TAC's and the data acquisition system ADC's, establishes the uncertainty in the width of each channel along the time axis. The final measured uncertainty in the channel width is ±90 fs/channel on the 40 ps/channel 'short' time axis and ±6 ps/channel on the 1.5 ns/channel 'long' time axis. Both of these correspond to an uncertainty of less than ±0.4%/channel. The width of the electron packet and other timing uncertainties (Equation 2.9) will add in quadrature to this channel to channel uncertainty and establishes the final <u>relative</u> uncertainty in locating the 'event' in time. The major contribution to this uncertainty is the width of the electron packet (measured during each data run) which is always less than 1 ns (typically < 0.7 ns, see Figure 2). The relative accuracy of the energy scale is then given by Equation 2.7 and plotted in Figure 3.

The ability to determine the location of the X-ray peak is much poorer and is the major contribution to the <u>absolute</u> uncertainty in locating an 'event' in time. Using, as a worst case, the value of one channel width, the uncertainty in the X-ray peak location is ±40 ps on the 200 ns scale and ±1.5 ns on the 8 μs scale. The absolute accuracy of the energy scale is again given by

Absolute Energy Scale
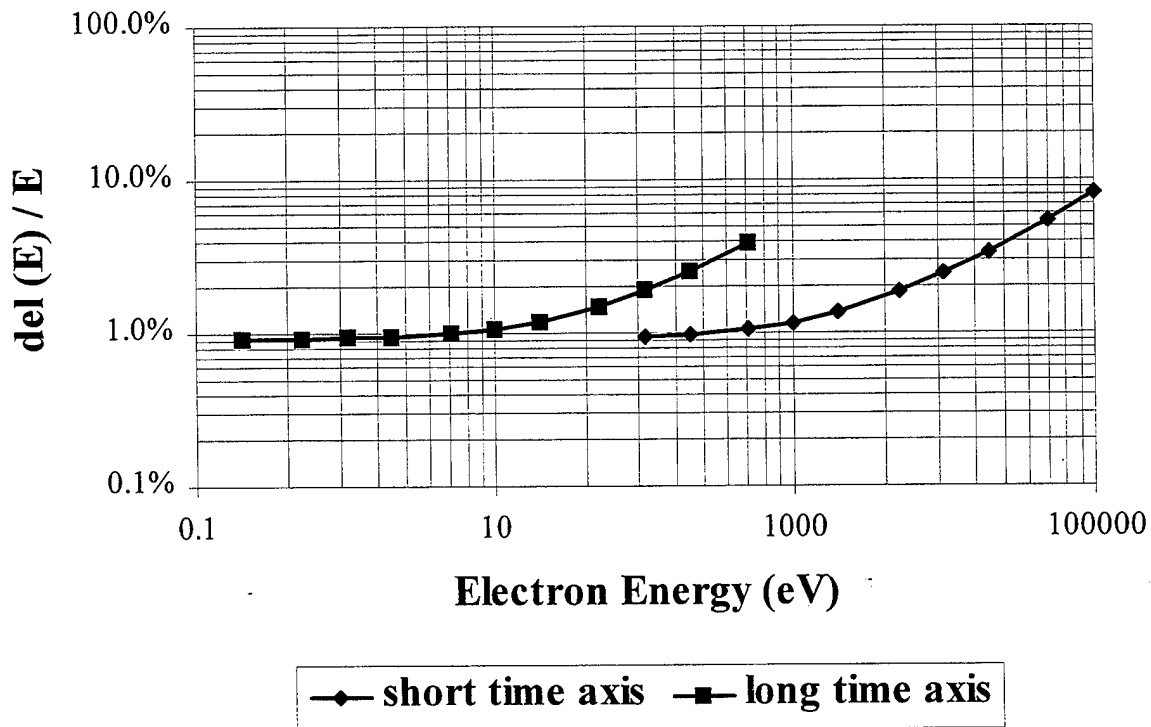
Figure 33: Absolute energy scale uncertainty.

Equation 2.7, but with ΔT given by ± 40 ps on the 200 ns scale and ± 1.5 ns on the 8 μs scale.

The resulting energy scale uncertainty is plotted in Figure 33. It is clear from this figure why

two time axes are used.

V. Machine Geometry and Solid Angle:

The solid angle subtended by the detector is determined by the target-detector geometry.

If the target were a point source, the solid angle would be the area of the detector aperture

projected on a unit sphere. The target is not a point source, but expends both along and normal to the flight path of the electron. The uncertainty in the subtended solid angle can be calculated from the possible range for the target-detector geometry. The extreme case (using $\Theta = 30°$, $\Omega = 15°$, $\Phi = 0°$) gives an uncertainty in the solid angle of $\pm 0.4\%$. The detector solid angle for the measurements presented here is:

$$\omega \quad = \quad 0.4469 \pm 0.002 \text{ msr.}$$

The next section discusses the measurements of the secondary and backscatter electron distributions for a subset of target materials.

Section 7 Experimental Results

Introduction:

The measurements presented here are the absolute yield of secondary and backscatter electrons

from aluminum, copper and carbon targets: $d^2\sigma(E_p,\theta_p,T,E_s,\theta_s,\phi_s)/dEd\Omega$. The data for the latter

two are at one incident electron energy (1900 eV) and one incident/emission angle set (in-plane

45° incident and 45° emission: $\theta_p = 45°$, $\theta_s = 45°$, $\phi_s = 0°$), while the data for aluminum cover

various incident energies and angles.

Energy Dependence:

Figure 34 is a overlay of the secondary electron emission spectrum at three incident

electron energies (i.e., $d^2\sigma(E_p=500,1900,6000eV,\theta_p=45°,T=Al,E_s,\theta_s=45°,\phi_s=0°)/dEd\Omega$). The

three spectrum shown here are for an aluminum target at 45° incident angle and 45° emission

angle. The secondary (δ) and backscatter (η) yield coefficients obtained by integrating the

spectrum over emission energy and angle are presented in Table 5. The difference between a

"secondary electron" and a "backscatter electron" is arbitrary and is defined as whether the

emission energy is below or above 50 eV. The values for the secondary emission coefficient (δ)

were obtained by integrating the measurements in Figure 34 over energy from 0.2 eV to 50 eV

and over the solid angle of the forward hemisphere (2π sr) (Equation 0.2):

$$\delta(E_p,\theta_p,T) = \int d\sigma/dEd\Omega \qquad 0.2 < E_s < 50 \text{ eV}, \theta_s \text{ and } \phi_s.$$

The error in δ associated with ignoring the data below 0.2 eV in the integration is at most 0.8%

(discussed below). The dependence on incident angle, θ_p, is removed by dividing the resulting

number by $\cos(\theta_p)$ (also an approximation).

$$\delta(E_p,T) \quad = \delta(E_p,\theta_p,T)/ \cos(\theta_p) \tag{7.1}$$

Absolute Electron Yield
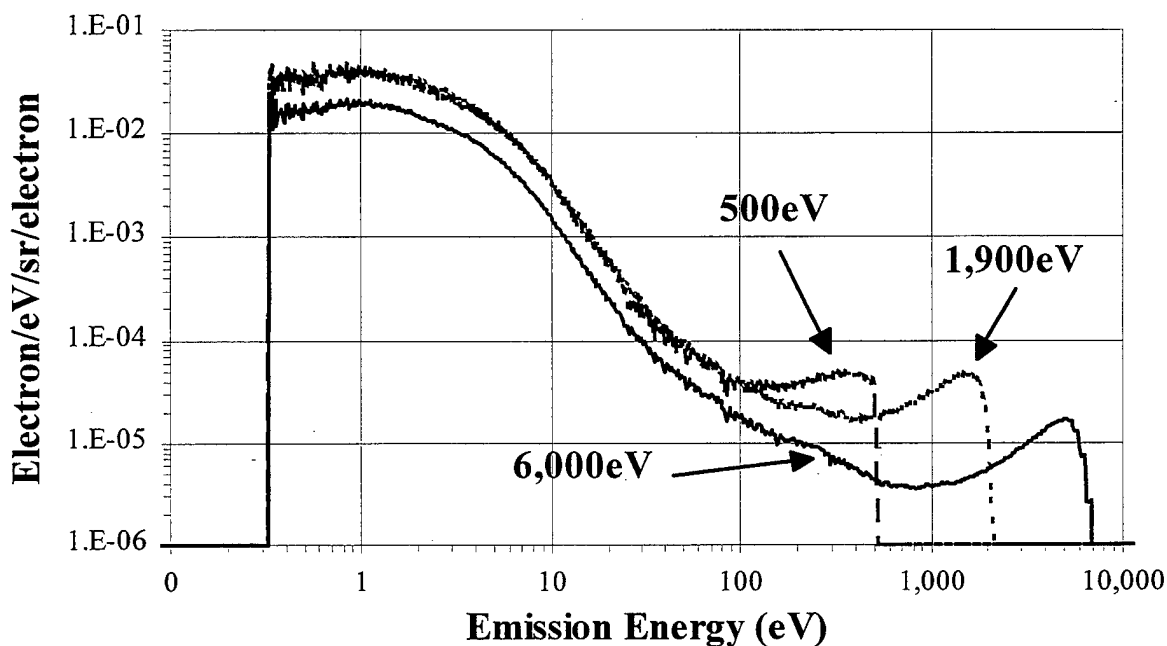
Figure 34: Emission spectrum at three incident engeries.

The values for the backscatter emission coefficient (η) were obtained by integrating over energy from 50 eV to incident beam energy and over the forward hemisphere (Equation 0.3).

$$\eta(E_p,\theta_p,T) \quad = \quad \int d\sigma/dEd\Omega \qquad E_s > 50 \text{ eV}, \theta_s \text{ and } \phi_s.$$

Table 5 is a listing of the values for δ and η from the data in Figure 34. A comparison with literature values is not possible as comparable measurements do not exist. The equivalent

values predicted by the Katz code (Equations 1.1 and 1.2) are in parentheses while those using

the Sternglass expression (Equation 1.3) are in brackets.

The assumptions made in the calculation of δ and η above are considered to be valid on a

gross scale. At higher incident energies, the shape of the emission spectrum ($d^2\sigma/dEd\Omega$) as a

Table 5:   Secondary (δ), backscatter (η) and total (σ) electron yield coefficients
                  for aluminum at 500, 1900 and 6000 eV.

Incident Energy	δ	+	η	=	σ
500 eV	1.25 (1.23) [1.28]		0.15 (0.17)		1.40 (1.40)
1900 eV	0.79 (0.87) [0.42]		0.27 (0.33)		1.06 (1.13)
6000 eV	0.38 (0.74) [0.28]		0.28 (0.33)		0.66 (1.07)

function of emission angle (θ_s and ϕ_s) for a fixed incident angle (θ_p) shows structure associated

with spectral reflection of the incident beam[†] (i.e., the elastic line is not isotopically scattered).

The assumed yield dependence on the $\cos(\theta_p)$ involves the assumption that the yield is

linearly dependent on the stopping power (minimal staggering) and the probability of an electron

being emitted is independent of the emission energy. Both of these are considered valid only in a

limited energy range (for incident electron energies above the peak in the secondary electron

yield curve, i.e., $E_p > E_{max}$ where for aluminum, $E_{max} = 1200$ eV) (Ref. 14).

---

†   The principal reasons for the present measurement sequence was to establish a data base
on which to examine the region (in energy and angle) of applicability of the various models (the
approximations and assumptions) currently used in this field.

<u>Low Energy Region:</u>

Figure 35 is the low energy region of the emission spectrum for copper, i.e., the

secondary electron emission spectrum $d^2\sigma(E_p=1900eV,\theta_p=45°,T=Cu,E_s,\theta_s=45°,\phi_s=0°)/dEd\Omega$.

Copper Spectrum: low energy region
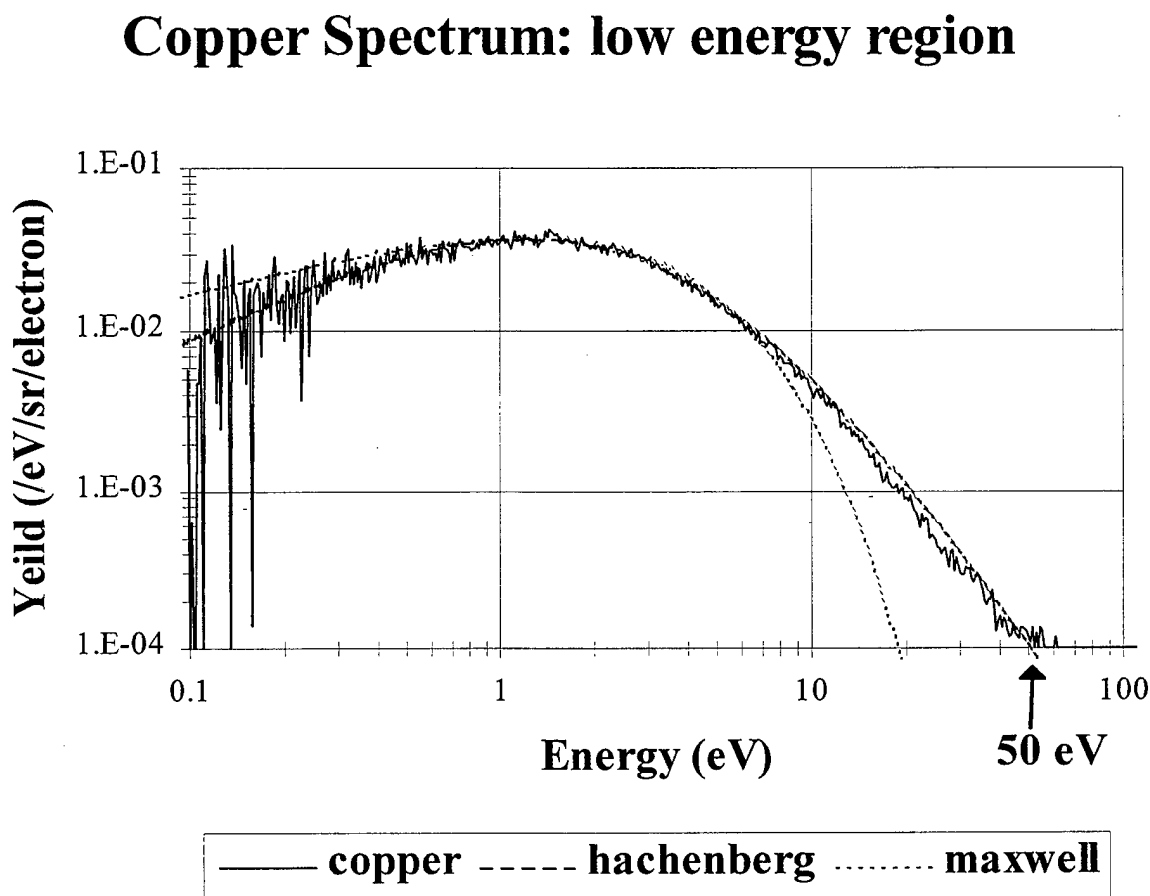
Figure 35: Low energy region emission spectrum for copper.

The distribution peaks at E_{peak} = 1.25 eV and has a FWHM of 3.8 eV. The values for the

secondary emission coefficient (δ) obtained from integration of the data (from 0 to 50 eV) is

1.29. The value for the backscatter coefficient (η) obtained from integration of the data (from 50

to 1900 eV) is 0.42. The measured total electron emission coefficient (σ) is 1.71[†]. The value for

σ', obtained from requiring the trap current and the target current to agree, was 1.685. The

agreement is 'nice' but considering the assumptions involved should be considered fortuitous[‡].

The corresponding values for δ, η and σ calculated from the Katz expression (Equations 1.1 and

1.2) are 1.37, 0.33 and 1.70. Again, subject to the assumptions involved, the agreement is 'good.'

This data is summarized in Table 6.

Table 6   Secondary (δ), backscatter (η) and total (σ) electron yield coefficients
for copper at 1900 eV.

δ	+	η	=	σ
1.29 (1.37) [1.23]		0.42 (0.33)		1.71 (1.70)

The shape of the low energy region ($E_s < 20$ eV) can be modeled in terms of a Maxwellian

distribution, with an amplitude related to the total emission and an effective temperature (E_0)

[†]   Again subject to the assumption of isotropic emission in the forward hemisphere (2π sr)
at all emission energies and a $1/\cos(\theta_p)$ dependence on incident angle.

[‡]   These two numbers are not independent. The value for σ' was derived from the
requirement that the target and trap currents agree at mode change over (between mode III and
mode IV). The total charge delivered to the target was then calculated from the integral of the
target current normalized to the trap current. The 'nice' agreement above between the value for σ
from integrating the spectrum and the value for σ' by forcing the mode change currents is not
always present. In some measurements, the difference between the two values for σ can be as
large as 30%, a number much too large to be attributed to the assumptions listed previously.
This difference needs to be fully understood in any future measurement.

related to the width and position of the secondary electron peak:

$$dY/dE = A * E^n * \exp(-E/E_0).$$ (7.2)

The peak of the emission distribution is located at an emission energy given by

$$E_{peak} = n * E_0.$$ (7.3)

where n is the Maxwellian exponent.

This is a valid representation for the energy dependence for electron emission distribution from a heated metal ($n=\frac{1}{2}$, $E_0 = kT_0$, for the tungsten filament in the electron gun, $T_0 = 1000$ K or $E_0 = 0.08$ eV). As seen in Figure 35, this functional form (with $n=\frac{1}{2}$ and $E_0=2.5$ eV) does not agree with the shape of the distribution of secondary electrons (it over predicts a low energies and under predicts at high energies).

Another model of the low energy emission distribution uses an expression developed by Hachenberg (Ref. 15):

$$dY/dE = A * E / (E + \phi)^4$$ (7.4)

where the model equates the value of ϕ with the material work function. This model distribution peaks at

$$E_{peak} = \phi / 3.$$ (7.5)

Using this functional form, the fit is better, with a value for ϕ of 3.75 eV. The work function of copper reported in the literature is $\phi_{Cu} = 4.0$ eV. It is clear that the noise in the measurement data below 0.2 eV will limit the accuracy of the secondary emission coefficient (δ).

The values for δ obtained from integration of the data and model fits in Figure 35 as a function of low energy cutoff are given in Table 7. In all cases, the Maxwellian fit underestimates (~10%) while the Hachenberg model overestimates (~3%) the measured secondary emission coefficient.

Table 7   Values for δ as a function of the low energy cutoff

Integration range	Maxwellian	Hachenberg	Measurement
0.0 - 50.0	1.17	1.33	1.29
0.2 - 50.0	1.16	1.32	1.28
0.3 - 50.0	1.14	1.31	1.27
0.4 - 50.0	1.12	1.29	1.26

The error in secondary emission coefficient (δ) associated with only integrating above 0.2 eV is seen to be less than 0.01 using either model for the above data. The fraction error (0.8% low) associated with this process should remain approximately the same for other targets, angles and incident energies.

High Energy Region:

Figure 36 is the high energy region of the secondary electron emission spectrum for aluminum. The energy of the incident electron beam was 500 eV. The spectrum shown is from the "short" time channel (the channel with the better time resolution). The energy resolution of the emitted electrons is dominated in this energy region by the width of the incident electron packet at the target (0.6 ns) and is 1.9%, i.e., ± 4.8 eV at 500 eV. The large structure seen at 470 eV is real (due to a single energy loss scattering process). But any structure with an energy

extent smaller than the available energy resolution (here ~5 eV) should, without further

investigation, be considered as due to counting noise[†]. The energy resolution at 400, 450 and

500 eV are shown below the spectra.

The search for structure is a highly subjective process. It helps to know where to look --

Aluminum Spectrum: high energy region
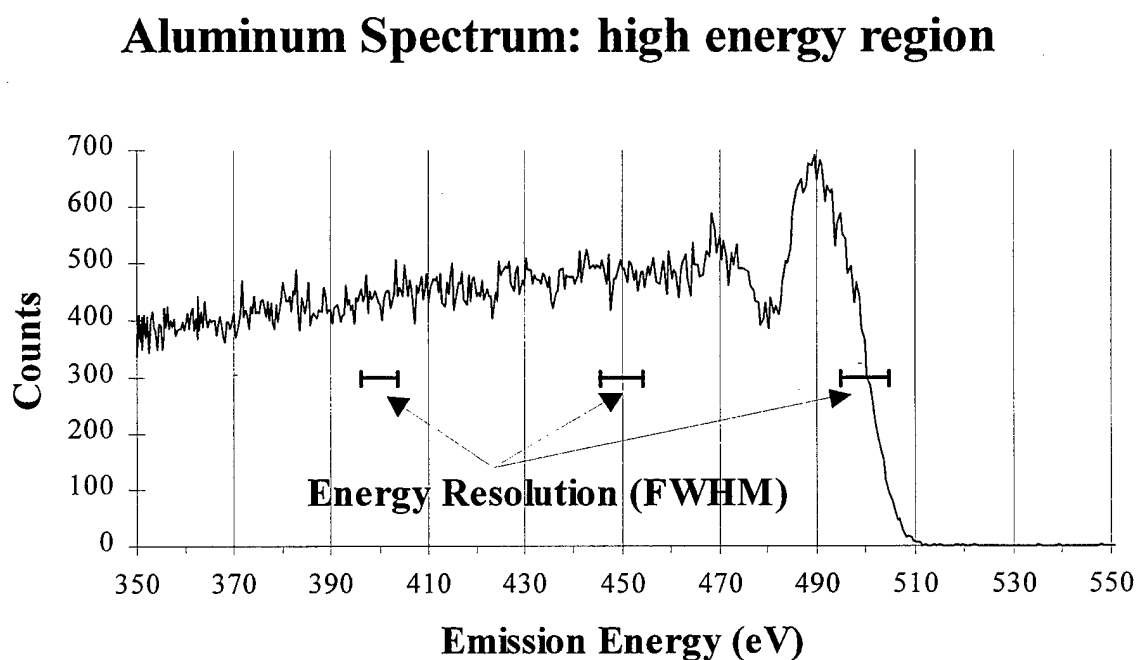
Figure 36: Typical emission spectrum for aluminum at high time resolution.

the foreknowledge will also result in "finding" a signal in noise based on a 'fortuitous

happenstance of chance'. Any structure must obviously be reproducible (more than a single

[†]   The experimental apparatus can be easily configured to examine structure (with regard to
energy and angle dependence). If an emission spectra (e.g., from a gas target) exhibited structure
of interest, the measurement parameters could be 'fined tuned' to enhance (i.e., improve the
energy resolution and signal to noise ratio) the signal over the region of interest.

observation), identifiable (vary in a predictable manner) and with a S/N ratio better than 1:1. A search to identify the source of structure in the emission spectrum is described in the following section.

Structure:

Figure 37 is the secondary electron emission spectrum for carbon (graphite) due to 1900 eV incident electrons. The secondary (δ) and backscatter (η) yield coefficients obtained by

Carbon Emission Spectrum
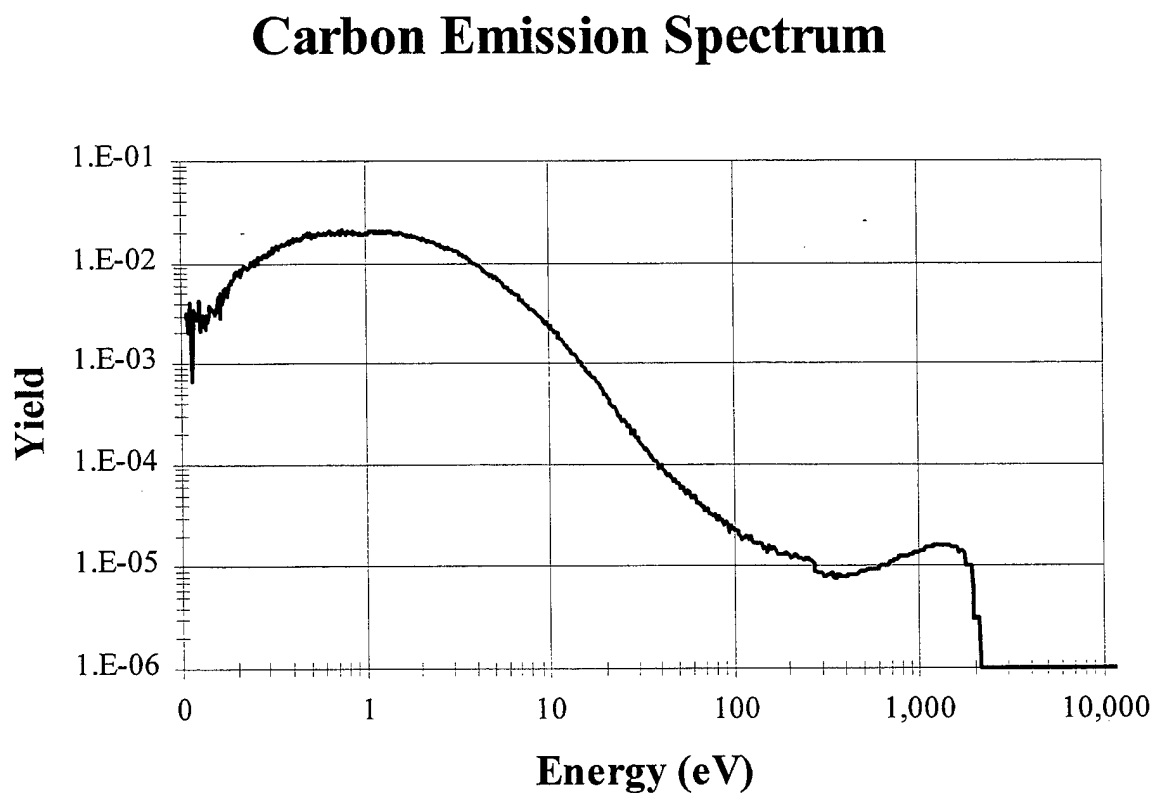
Figure 37: Electron emission spectrum for carbon at 1900 eV incident energy.

integrating the carbon spectrum over emission energy and angle are presented in Table 8. Again

a comparison with literature values is not possible as comparable measurements do not exist.

The structure near 270 eV in Figure 37 is examined in this section (the yield changes by 20% within an 8 eV energy range). When plotted against time of flight, this structure appears at a flight time of 98.3 ns. The appearance of this structure was unexpected. Initially it was thought to be an artifact of the measurement. Various possible sources of such a structure are examined below.

Table 8   Secondary (δ), backscatter (η) and total (σ) electron yield coefficients for carbon at 1900 eV.

δ	+	η	=	σ
0.67 (0.83) [0.44]		0.16 (0.21)		0.837 (1.04)

A)   If the X_0 and Y_0 offset bias on the deflection plates of the electron gun were improperly adjusted, it is be possible for the trailing edge of the sweep pulse (which moved the incident DC electron beam across the skimmer aperture and thereby generated the incident electron packet) to produce a second electron packet, delayed by the width of the sweep pulse, which would generate a second emission spectra (X-ray flash, elastic line, ...) displaced in time by the width of the sweep pulse. The width of the sweep pulse was ~100 ns. Any structure due to such a double pulsing would occur at 100 ns displaced from the elastic line, not 100 ns from 'zero time' (which is 63 ns from the primary beam elastic line at this incident energy). This possibility was eliminated by examining the effect of the width of the sweep pulse on the structure, with no

affect.

B)   A second possible source could be secondary electrons generated within the electron gun by the pulsed primary electron beam hitting an aperture or other electron gun optical lens element. The final energy of these secondary electrons will be given by the voltage of the 'hit' aperture relative to chamber potential. For these secondary electrons to exit the electron gun, they would need to be accelerated and passed (focused) by the following electron optics. They would constitute a (pulsed) electron beam of lower energy incident on the target. The co-traveling electron packet would generate its own secondary electron spectrum when it hits the target. In the above, the structure seen was thought to be the elastic line of this co-traveling electron beam. The requirement that the following electron optics must pass this lower energy electron packet is difficult to accept, but it can happen for a particular set of focus voltages. This possibility was eliminated by examining the dependence of the structure on electron gun lens focusing voltages. The structure did not move in time with variation of the electron gun lens voltage. The generation of these cotraveling electrons was discussed in Section 2.

C)   The structure could be a scattered incident electron that has experienced a specific energy loss at the target, in this case: $E_{loss} = E_{in} - 270$ eV $= 1630$ eV). This possibility was eliminated by examining the dependence of the structure on incidence electron beam energy. The structure did not move in time (i.e., emission energy) with variation of beam energy.

D)   The structure could be due to electrons emitted by the target at a specific energy (e.g., an

127

Auger process). Carbon has Auger emission lines from 260 to 270 eV. If this line is due to the carbon Auger emission, it may be possible to observe Auger lines from contaminates, i.e., at 380 eV for nitrogen (adsorbed air) and 500 eV for oxygen (adsorbed air and water vapor) in the same spectrum. Only the 270 eV line is seen in the carbon spectra. Aluminum has Auger emission at 70 eV and 1400 eV; spectra for aluminum were examined, but no comparable structure at these two emission energies was seen.

In an attempt to determine the source of this structure, a bias voltage was placed on the

Carbon Emission Spectrum
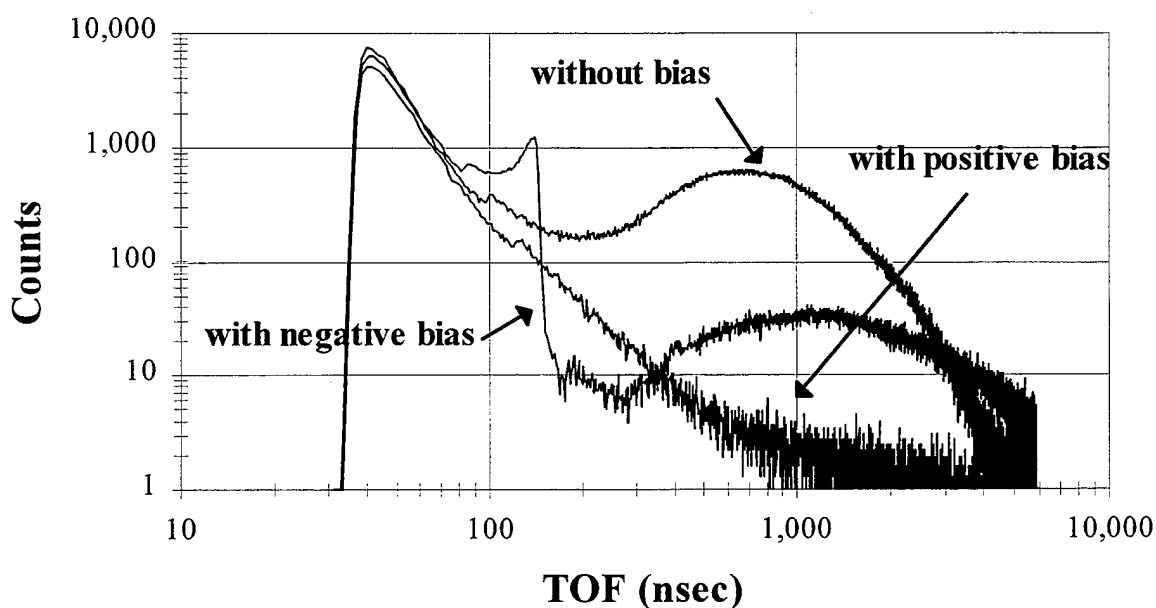
Figure 38: Carbon emission spectra with 0, -100 and +100 V applied to the target plotted as a function of arrival time.

target to 'tag' the emitted electrons. Figure 38 is an overlay of the measured emission spectra plotted against flight time. The spectra differ only in bias voltage applied to the target during the measurement. Figure 39 is the same spectra on an expanded time scale about 100 ns. The structure near 100 ns (without bias) moves to a shorter/longer flight time (85/120 ns) when a bias of -100/+100 V is applied to the target. The general movement of the structure is consistent with emission at a fixed energy from the target (i.e., Auger process).

The addition of the bias on the target changes the measured spectra in two ways: a) the incident electron energy 'at the target' is changed to $1900 + V_{bias}$, and b) the emitted electron energy 'at the detector' is changed to $E_s - V_{bias}$. In this type of measurement, the energy of the emitted electron is determined from the measured flight time. As the bias voltage is only ~5% of the incident electron voltage, the bias on the target does not appreciably change the time required for the incident electron to arrive at the target (confirmed from the almost non-movement in the X-ray flash in the three measurements). But the bias on the target does change the time required for an emitted electron to reach the detector since the emitted electron will gain or lose energy all along the flight path.

In modeling this process, the assumption is made that the region in which the acceleration/deceleration field due to the target bias is small and localized near the target, i.e., the electron will travel at its final velocity ($\propto \sqrt{(E_s - V_{bias})}$) over the majority of the flight path to the detector. Using nominal values for this partition (20%/80%), the calculated flight time of an electron with emission energy of 270 eV will arrive at the detector at the time shown in Figure

129

39. The calculated shift of the structure in time agrees with the measured value on a gross scale,
i.e., a positive (negative) bias will lengthen (shorten) the TOF of the emitted electron. In fact, the
calculated TOF for the positive bias (using the above 20%/80% partition) agrees with the
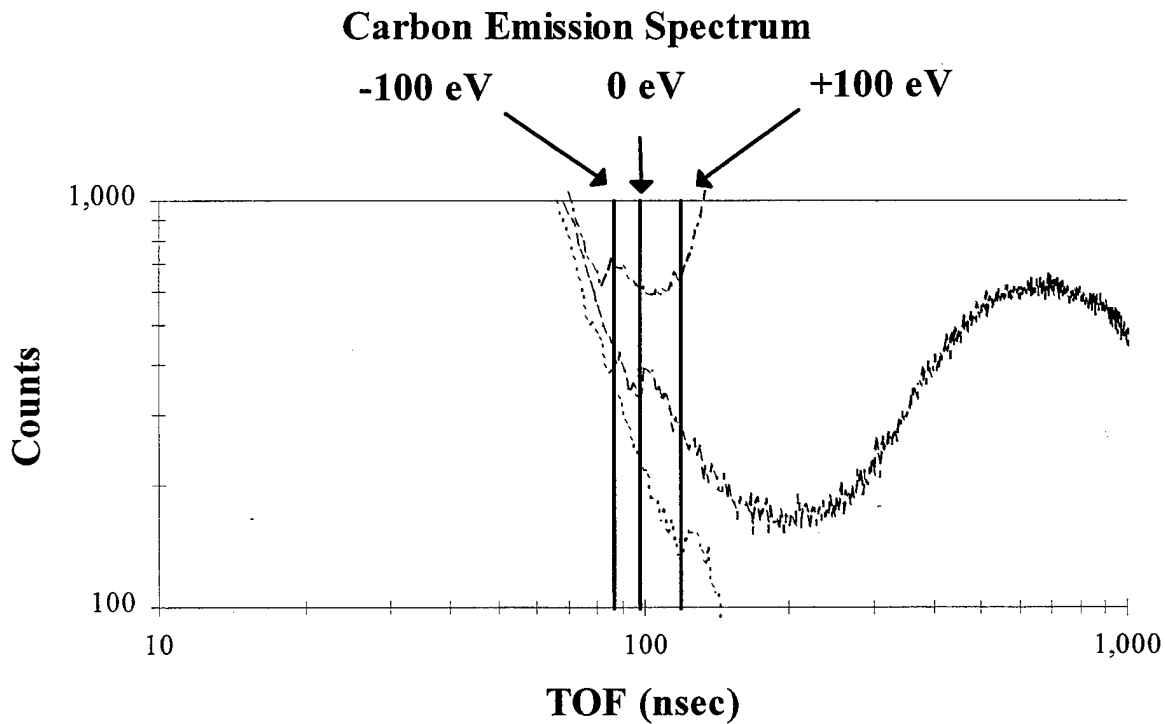
Figure 39: Spectrum for Figure 38, plotted on an expanded time scale about 100ns flight time.

measurement, but the calculated TOF for the negative bias is high by 5.3 ns. This difference can

be reduced to 2.5 ns by assuming a partition of 0%/100% (i.e., the unrealistic assumption that the

emitted electron is acceleration/deceleration instantaneously to its final value), but then the

previous agreement for the positive bias is removed (the measurement and calculation now differ

by 5.2 ns).

The conclusions of the structure search are: the structure is real, it is related to emission from the carbon target and does move approximately in a predictable manner, but the emission process is unknown. It would be nice to identify the structure as due to Auger emission, but no Auger emission structure was observed for aluminum (which has Auger emission near 70 and 1400 eV). The lack of measurable Auger emission for aluminum could be related to the magnitude for the Auger cross section.

The next section discusses conclusions reached during this research.

Section 8: Conclusion

The purpose of this research effort was to generate a data base of secondary and backscatter electron yield measurement for materials currently used in space. Only a limited number of target materials have been examined to date, but this data is sufficient to indicate that the machine is working properly and generating numbers that are comparable with the limited data presently available. The data generated is a high quality measurement of the emission energy distribution for the targets examined. The apparatus is complete. In its present form, it will generate spectral data on conducting targets over a range of incident energies from 100 eV to 20 keV[†] over incident and emission angles from normal to ~± 80°.

Only one target material has been examined in detain, aluminum, but no extensive data on emission yield as a function of incident (θ_p) and emission (θ_s, ϕ_s) angles has been taken. The only observation that can be made (based on the three targets examined: Cu, C and Al) is that the present data (reflected in the integral value for δ) equals or is below the values calculated using the Katz expression (Equation 1.1) and equals or is above the values calculated using the Sternglass expression (Equation 1.3). Only for aluminum, at 500 eV, do all three agree. The same trend is followed for the values for η. It would be inappropriate, because of the limited amount of data taken to date, to apply the above observation to other target materials.

[†]   Near the 20 keV level, the machine has an enhanced tendency to 'arc and spark'.

Because of the very low electron fluence (< 10 pA) used during a typical emission spectrum measurement, this machine is ideal for measurements with insulating targets. There is almost no data available on the emission spectrum from insulators. The data available is usually on the integrated yield σ and the cross-over or floating potentials (the two energies at which σ become equal to unity). To make such measurements, the target holder needs to be modified such that larger potentials can be applied to the target for systematic tests. No data has been taken on semiconducting or insulating targets to date.

Before any additional measurements are made, a number of questions need to be addressed. None reflect a limitation in the operation of the machine, but are concerned more with the interpretation of the data generated:

1.   Would it be possible to use a small potential (~± 1 V) applied to the target to move the low energy emission away from the 'late high energy' electron cutoff and thereby improve the integrated value obtained for δ?

2.   The sometimes different values for σ; one from the integral of the emission spectrum, the second from the target/trap measurements, needs to be fully understood. The obvious explanation, that the assumption of non-isotropic emission is not correct, is very intriguing.

3.   Related to number 1 above, can the contact potential between the target material and the chamber be ignored as was done for the data presented here?

4.   The structure seen in the carbon data (at 270 eV emission energy) needs to be fully understood. It appears to be from Auger electron emission, but the variation with target potential is not as predictable as it should be (i.e., the addition of a negative bias to the target fails to agree in detail with the calculated shift, while the positive bias agreed). Similar Auger emission from other targets has not been seen.

5.   The calibration of the electron detector system (SEM/MCP pair) needs to be extended in incident energy and published.

6.   Related to number 5 above, a check of the spatial extent of the electron 'beam' used in the calibration of the electron detector system needs to be made.

7.   The target mount needs to be modified to improve the incident and emission angle interdependence (i.e., reduce $d\phi/d\Omega$ and $d\theta/d\Phi$ to values near 1).

8.   Energy loss spectra (at high emission energies) for selected targets need to be made to resolve the structure present here.

The machine has the capability of generating high quality secondary and backscattered electron emission spectra for conducting target materials. The machine has yet to be used in a systematic examination of the materials currently used in space.

Electron optic transport software:

This program is based on a paper by Kisker (Ref. 16), who used a theory developed by Bertram (Ref. 17). Under the Gaussian approximation, only the potential on the axis of the lens system is needed to establish the potential distribution of an electron lens system. The present program develops the potential distribution between two tube elements of a single lens system in terms of the potential distribution on the axis of the tube lens, the boundary condition at the wall of the tube elements and in the gap between the ends of the tube elements. Assuming paraxial electron rays, the electron trajectories through the electron lens system can be obtained by integrating the electron path along a suitable grid (i.e., this program is a PIC code).

Data analysis software:

The spectrum and scaler data streams are processed separately, but are connected through the time flag associated with each data event (i.e., the data was taken in 'event mode'). The raw data files (listl.*, lists.* and scaler.*) collected with the CAMAC system were converted from binary to ASCII using the program 'convert.' This program reads the 'list?.*' files and generates two output files: 'lsl' and 'lss' which contain the spectrum information ('lsl' for the long time axis, 'lss' for the short time axis) as a stream of data (the time flag has been removed from this stream - if the data need be cut at selected times (e.g., to make an offset spectrum measurement (Mode IVd, on|with) in the middle of a direct spectrum measurement (Mode IV, on|with)), 'convert' can be configured to do so - but this requires some "tinkering"). The program 'convert' will also read

the 'scaler.*' files and generate a single 'sch' file which contained the scaler information in event mode with time steps of 10 s (the time flag has been retained for this stream). The spectrum data is further processed by the program sequence: 'stepls', 'step1', 'step2', and 'step3'. The scaler data is processed by the program sequence: 'stepsch' and 'step0'. Both of these paths are considered in detail below.

List-sequencer Path:

The program 'stepls' or 'step2ls' generates the files that hold the spectrum information, '$.l' and '$.s'. The program 'step1' places these files on a time axis using the location of the X-ray flash channel. The program 'step2' converts the TOF spectrum to an energy spectrum and normalizes the data based on total charge delivered to the target and corrects for detector efficiency and dead time. The program 'step3' corrects for the offset spectrum and integrates the absolute yield spectrum over energy and angle.

Processing of the raw list-sequencer data files:

1)   run 'convert -l -n 2 -o ls list01.*' to generate the 'ls' file

or

1a)   run 'convert -l -n 1 -o lsl listl.*' to generate the 'lsl' file

1b)   run 'convert -l -n 1 -o lss lists.*' to generate the 'lss' file

2)   run 'name' to generate the file 'filename' which contains the name ($) and the file '$.c' which contains the name and the detector size and location (aperture & setback)

3)   run 'stepls' which reads the 'ls' and '$.c' files and generates the 'short' ($.s), 'long' ($.l) and

'cal' ($.c) files

or

3a)   run 'step2ls' which reads the 'lsl', 'lss' and '$.c' files and generates the 'short' ($.s), 'long'

($.l) and 'cal' ($.c) files

4)   run 'step1' which reads 'filename' to get '$', 'axisname' to get '#', '#.x' (time axis

information file), '$.c' (the data run information) and the '$.[l,s]' (the binned data) files.

This program will generate the rebinned data on a time scale and the data corrected for

background. The files 'timel', 'times', & 'ntimes' (renormalized by time channel widths)

are generated. The time zero channel is located in one of three ways:

a)   the location and time width of the gamma peak

b)   uses the edge of the elastic line (either at the 1/3 or ½ point)

c)   uses any other structure in the spectrum

5)   run 'step2' which reads 'timel' and 'times' to generate a normalized yield vs energy file

('energyl' and 'energys') ['energylwo' and 'energyswo' are the same spectra uncorrected for

the detector efficiency]. The dead time correction is obtained by normalizing the total

charge on target by the dead time ratio.

6)   run 'step3' which reads 'energyl' to correct for the offset spectrum and generate the

integral secondary and backscatter electron yield.

Scaler Path:

The program 'stepsch' generates the various scaler files that hold the scaler information in

event mode. Some of these files are further processed using the program 'step0' which calculated

137

the "beam trap current," the "target current" and the dead time correction for the two time axis channels (long and short).

Processing the raw scaler data files

1) run 'convert -sh -n m -o sch scaler.*' to generate the 'sch' file

2) run 'stepsc' which reads the 'sch' and '$.c' files and generates the time history of the counts in each dump for the m scaler channels ('$.[0-9,a,b]') and the count rate for the m scaler channels (i.e., normalized by the 1 MHZ clock frequency in channel 0) in the '$.1[1-9,a,b]' files.

3) run step0 which reads the '$.13' (:=target), '$.14' (:=trap), '$.0' (:=clock) '$.15' (:=short TAC clock) & '$.16' (:=long TAC clock) these files are processed to generate the dead time correction for the short and long TACs and the total charge on the target during the experiment (delta for the target is determined from the fit of the target current and the trap current

Absolute Time Axis Calibration:

The long and short time axis were calibrated with the same electronics used for the spectrum measurements, the only difference was that the start and stop input now came from a calibrated pulse generator. The programs used to process this data were similar to that for the spectrum data except the program also fit the sequence of calibration peaks and generated a value for the mean and standard deviation of the time per channel for each time axis.

138

Generation of the slope for the 'long' and 'short' time axis

1)   run 'convert -l -n 2 -o ls list01.*' to generate the 'ls' file

or

1a)   run 'convert -l -n 1 -o lsl listl.*' to generate the 'lsl' file

1b)   run 'convert -l -n 1 -o lss lists.*' to generate the 'lss' file

2)   run 'axis' to generate the file 'axisname' which contains the name (#) and '#.x' file which

        contains the name and period information

3)   run 'axisls' which reads the 'axisname', 'ls' and '#.x' files

or

3a)   run 'axis2ls' which reads the 'axisname', 'lsl', 'lss' and '#.x' files and generates the 'long'

        (#.l), 'short' (#.s), 'cal' (#.x) and data output (timeaxis.out) files

4)   run 'timeaxis' which reads '#.[s,l,x]' and calculates the axis slope (in nsec/channel). This

        additional information is then stored in the '#.x' file

APPENDIX B

Examination of Poisson Statistics:

A crude estimate of the expected signal count rate can be determined from the electron

Table B-1   Typical Experimental Parameters

Incident DC beam current:	20 nA
X-ray flash FWHM:	1 ns
Sweep pulse rate:	100 kHz
Detector solid angle:	3×10^{-4} sr
Detector efficiency:	80%
Total secondary yield σ:	2 electron/electron
(aluminum target and incident electron energy of 2 keV)	

gun and detector properties, and from the target/detector geometry. The nominal values used in

this calculation are given in Table B-1. By assuming the total yield ($\sigma = \delta$[true secondary] +

η[backscattered]) is isotropic into the forward hemisphere (2π sr), then

~ 125 incident beam electrons arrive at the target (per packet),

~ 1.2×10^{-2} secondary electrons arrive at the detector per sweep pulse,

which generates

~1000 cps as the total detector output count rate.

The above numbers are important because the probability (p) of an event occurring (secondary

Table B-2	Probability of Missed Events		
n*p:	0.01 (1 kcps)	0.05 (5 kcps)	0.1 (10 kcps)
P(0):	0.99005	0.95123	0.90484
P(1):	0.00990	0.04756	0.09048
P($\geq$2):	0.00005	0.00121	0.00458
P($\geq$2)/P(1):	0.5%	2.5%	5.1%

electron being detected) is small (8×10^{-5} detected electrons per incident electron), while the

number (n) of samples (incident electrons) is large (125 electrons per sweep pulse). Under these

conditions, Poisson statistics apply. The product, n*p, is the mean number of detected events per

sample (sweep pulse). Which, for the above, has a nominal value of 0.01. The probability of

detecting zero, one or 'two-or-more' events (electrons) per sample (sweep pulse) is given in Table

B-2. Given that the first electron is detected, there is a 0.5(2.5,5.1) % chance of missing a second

electron when the mean detector count rate is 1(5,10) kcps.

References

1. Dekker, A.J., "Secondary Electron Emission," Solid State Physics, Vol. 6, p 251, 1960.

    Hachenberg, O. and Brauer, W., Advances in Electronics and Electron Physics, Vol. 16, p 145, 1962.

    Gibbons, D. J., "Secondary Electron Emission," Handbook of Vacuum Physics, Vol. 2, p. 299, Pergamon, 1966.

    Willis, R. F. and Skinner, D. K., "Secondary Electron Emission Yield Behavior of Polymers," Vol. 13, p 685, 1973.

    Whipple, E. C., "Potentials of surfaces in Space," Reports on Progress in Physics, Vol. 44, No. 11, p 1197, Nov 1981.

2. Suszcynsky, D. M. and Borovsky, J. E., "Modified Sternglass theory for the emission of secondary electron by fast-electron impact," Physical Review A, Vol. 45, No. 9, p 6424, May 1992.

3. Garrett, H. B., "The Charging of Spacecraft Surfaces," Chapter 7 of the Handbook of Geophysics and the Space Environment, A. S. Jursa Editor, Air Force Geophysics Laboratory, 1985

4. Radar Hit Confirmation Concept, Volume I, Contract No. F29601-88-C-0068, General Atomics, June 5, 1992.

5. Katz, I., Parks, D. E., Mandell, M. J., Harvey, J. M., Brownell Jr., D. H., Wang, S. S., and Rotenberg, M., A Three Dimensional Dynamic Study of Electrostatic Charging in Materials, NASA CR-135256, SSS-R-77-3367

6. Sternglass, E. J., "Backscattering of Kilovolt Electrons from Solids," Vol. 95, No. 2, p 345, July 1954.

7. Prokopenko, S. M. L. and Laframboise, J. G., "High-Voltage Differential Charging of Geostationary Spacecraft," Journal of Geophysical Research, Vol 85, No. A8, p 4125, Aug 1980.

8. Mullen, E. G., Gussenhoven, M. S., Hardy,D. A., Aggson, T. A., Ledley, B. G., and Whipple, E., "SCATHA Survey of High-Level Spacecraft Charging in Sunlight,"

Journal of Geophysical Research, Vol. 91, No. A2, p1474, Feb 1986.

9. Gussenhoven, M. S., Hardy, D. A., Rich, F., Burke, W. J., and Yeh, H. C., "High-Level Spacecraft Charging in the Low-Altitude Polar Auroral Environment," Vol. 90, No. A11, p 11009, Nov 1985.

10. Handbook of Chemistry and Physics, The Chemical Rubber Co. 1969

11. Yaer Ji and Wu, Ting, "Study of Poisoning of an Oxide Cathode" J. Vac. Sci. Technol. A, 6(3), p. 1073-1074, May/Jun 1988.

12. Simon, R.E. and Williams, B.F., "Secondary-Electron Emission," IEEE Trans. Nucl. Sci., Vol. NS-15, p 167, 1968.

13. Goruganthu, R.R. and Wilson, W.G., "Relative electron detection efficiency of microchannel plates from 0-3 keV," Rev. Sci Instrum., Vol. 55, No. 12, p 2030, Dec 1984.

14. Shimizu, R. and Ze-Jun, D., "Monte Carlo modeling of electron-solid interactions," Report on Progress in Physics, p 487, 1992.

    Chung, M.S. and Everhart, T.E., "Simple calculation of energy distributions for low-energy secondary electrons emitted from metals under electron bombardment," Journal of Applied Physics, Vol. 45, No. 2, p 707, Feb 1974.

    Koshikawa, T. and Shimizu, R., "A Monte Carlo calculation of low-energy secondary electron emission form metals," Journal of Physics. D: Applied Physics, Vol. 7, p 1303, 1974.

    Henke, B. L., Smith, J.A. and Attwood, D.T., "0.1-10-keV x-ray-induced electron emissions form solids-Models and secondary electron measurements," Journal of Applied Physics, Vol. 48, No. 5, p 1852, May 1977.

    Everhart, T. E., "Simple Theory Concerning the Reflection of Electrons from Solids," Journal of Applied Physics, Vol. 31, No. 8, p 1483, Aug 1960.

15. Hachenberg, O. and Brauer, W., "Secondary Electron Emission form Solids," Advances in Electronics and Electron Physics, Vol.16, p 145, 1962.

16. Fink, J. and Kisker, E., "A method for rapid calculations of electron trajectories in multi-element electrostatic cylinder lenses", Rev. Sci. Instrum., Vol. 57, No. 7, p 918, Jul. 1980.

17.   Bertram, S. "Calculation of Axially Symmetric Fields," <u>Journal of Applied Physics</u>, Vol. 13, p 496, Aug 1942.

DISTRIBUTION LIST

AUL/LSE
Bldg. 1405 - 600 Chennault Circle
Maxwell AFB, AL 36112-6424   1 cy

DTIC/OCP
8725 John J. Kingman Rd, Suite 0944
Ft Belvoir, VA 22060-6218   2 cys

AFSAA/SAI
1580 Air Force Pentagon
Washington, DC 20330-1580   1 cy

AFRL/PSTL
Kirtland AFB, NM 87117-5776   2 cys

AFRL/PSTP
Kirtland AFB, NM 87117-5776   1 cy

LtCol Geoff McHarg
AFA Physics Dept
HQ-USAFA/DFP
2354 Fairchild Dr. Suite 2A6
USAF Academy, CO 80840-6254   1 cy

Dr Steve McCready
UNM Physics and Astronomy Dept
800 Yale
Albuquerque, NM 87131   1 cy

Dr C. Lon Enloe
James Madison University
College of Integrated Science and Technology
Harrisonburg, VA 22807   1 cy

AFRL/VS/Dr Fender
Kirtland AFB, NM 87117-5776   1 cy

Dr J. R. Dennison
Utah State University
Department of Physics
SER Bldg. 222D
4415 University Blvd
Logan, UT 84322-4415   1 cy

Official Record Copy
AFRL/VSSE/Dr Warren Wilson
Kirtland AFB, NM 87117-5776   8 cys